ULTRA-LOW FREQUENCY WAVES, MAGNETIC PULSATIONS, AND THE IONOSPHERIC ALFVÉN RESONATOR

A DISSERTATION
SUBMITTED TO THE FACULTY OF THE GRADUATE SCHOOL
OF THE UNIVERSITY OF MINNESOTA
BY

JESSE RICHARD WOODROFFE

IN PARTIAL FULFILLMENT OF THE REQUIREMENTS
FOR THE DEGREE OF
DOCTOR OF PHILOSOPHY

ADVISOR ROBERT LYSAK

DECEMBER 2010

Acknowledgments

I would like to thank my advisor Robert Lysak for giving me the opportunity to discover my interests and pursue my own research. The insight I've found in his work has been key in helping me to develop insights of my own. I am also grateful to my colleagues Scott Thaller, Lei Dai, and Lenny Wilson for many interesting conversations.

Much thanks is owed to my parents, Phil and Patty Woodroffe, who always encouraged me to follow my passions and never discouraged me from trusting myself. Without their loving and tireless support, I may have never found my way into college, much less out of graduate school.

Finally, I am grateful to the teachers who have guided me along the path of learning, however winding it may have been. At Moose Lake High School, Dave Waechter and Tom Deering introduced me to mathematics and the study of the natural world; at Augsburg College, Ken Erickson and Mark Engebretson introduced me to space physics and research; and at the University of Minnesota, Tom Jones, Cindy Cattell, and John Wygant gave me the tools and understanding needed to tackle tough questions and find answers. That I have come this far is thanks to the effort of others to help me along the way. I will be forever thankful.

This material is based upon work supported by the National Science Foundation under Grant No. 0602464

Dedication

To Laura, whose love and patience have made this work possible.

Abstract

Magnetic pulsations are the signatures of ionospheric currents which are driven by magnetospheric ultra low frequency (ULF) waves. The characteristics of ULF waves with frequencies near 1 Hz is strongly dependent on the structure of the plasmas in the ionosphere and near-Earth magnetosphere, particularly those of a region known as the Ionospheric Alfvn resonator (IAR).

The IAR is an inhomogeneous plasma region bounded below by a conducting ionosphere and above by a sharp increase in the Alfvén speed. The Alfvén speed reaches a minimum near the ionosphere, but the location of the minimum is not strictly coincident with the ionospheric boundary, being located at the F_2 density peak some 100's of kilometers above. The particular structure of the IAR allows for the existence of two particular ULF eigenmodes, cavity and waveguide modes. The cavity eigenmode is a localized shear oscillation of a particular magnetic field line, while the waveguide mode is a transversely propagating compressional oscillation near the Alfvén speed minimum. Each IAR eigenmode is characterized by a particular spectrum of resonant frequencies. The cavity and waveguide modes are coupled by the action of ionospheric Hall currents, which also produce detectable signatures below the ionosphere.

Using realistic models of the IAR Alfvén speed and geomagnetic field, we have studied the properties of IAR and its effects on ULF waves both inside and outside the IAR. Our results indicate that models which do not account for the separation of the Alfvén speed minimum from the ionosphere may incorrectly predict the resonance structure of the IAR. In addition to this eigenmode analysis, we present results from a three-dimensional finite difference time domain (FDTD) model. This model is unique in its ability to self-consistently calculate electromagnetic fields both above and below the

ionosphere, thus providing an accurate representation of electrodynamic processes at the ionospheric boundary and in the IAR. Results from this simulation demonstrate that the structure of the ionospheric boundary is itself an important factor in determining the properties and lifetime of IAR cavity modes and their ionosphere-mediated coupling the the waveguide mode.

Contents

List of Tables

List of Figures

Chapter 1

Introduction

1.1 The Earth's Plasma Environment

1.1.1 The Solar Wind

The surface temperature of the sun (i.e. the photosphere) drops as low as 4200 K, but its corona - the outer layer of the solar atmosphere - is nearly 10^6 K at its base[74]. The asymptotic temperature of the interstellar medium is significantly lower than this, and the associated thermal pressure is much lower than that at the coronal base. It was shown by Parker[65] that this requires the existence of a supersonic outflow of solar plasma, the solar wind.

The solar wind typically flows radially outward from the sun with a speed between 300 and 800 km/s. Embedded in the flow of the solar wind are solar magnetic field lines (the IMF), which are carried outward due to the effect of magnetic flux freezing[65]. Because one end of these field lines are anchored to the sun, the solar rotation causes

the field lines to be drawn out in a spiral-like geometry. At 1 AU (i.e. at the Earth), the solar wind magnetic field makes an angle of approximately 45° with respect to the Earth-Sun line (the x_{GSE} direction). The solar wind density decreases with distance but 5 particles per cm^3 is typical at 1 AU.

There are distinct periodicities in the solar wind related to the 11-year solar cycle as well as the presence of solar features known as coronal holes and the $\approx$ 25 day solar rotation period.[1] Moreover, impulsive ejections of solar plasmas called coronal mass ejections (CMEs) are known to carry out plasmas with extremely high densities 40 cm^{-3} or greater) and/or speeds (in excess of 2000 km/s). This variability in the properties of the solar wind is of fundamental importance in space physics, because it is the primary source of energy for driving non-equilibrium processes in the magnetosphere. In particular, CMEs are known to be responsible for strong magnetic storms and variation of the IMF north/south[2] component is strongly linked to the triggering of magnetic substorms[56],[80].

1.1.2 The Magnetosphere

The region of space within which the geomagnetic field is confined by the outflowing solar wind is known as the magnetosphere. The magnetosphere is separated from the solar wind from a relatively thin current layer known as the magnetopause. The shape and position of the magnetopause is controlled by the balance of the geomagnetic field and solar wind dynamic pressure. Consequently, the magnetosphere is asymmetric along the Earth/Sun line, being compressed on the day side and stretched into an extended tail-like configuration on the night side[86].

[1] This is an average value. Being a fluid body, the sun experiences differential rotation with the equator rotating more rapidly than the poles. See the article by Brandenburg[13] for more details.

[2] With respect to solar ecliptic plane.

Distortion of the geomagnetic field requires the presence of a current sheet. On the day side this is the Chapman-Ferraro current, which runs east/west along the magnetopause, and on the night side this is the cross-tail current. These current systems connect to magnetic field lines which trace down to high geomagnetic latitudes. The exact footprints of these current systems varies depending on the level of geomagnetic activity[3], but on average these currents map to 75° magnetic latitude.[4] At the base of these field lines - and, indeed, all geomagnetic field lines - is a region or relatively cold ($T \sim 1$ eV) and dense plasma known as the Ionosphere.

The ionosphere arises from the ionization (by solar UV, charged particle precipitation, and cosmic rays) of the Earth's neutral atmosphere, the density of which increases rapidly near to the Earth's surface according to a balance of (primarily) thermal and gravitational effects. The ionosphere occupies the range of altitudes $60 \lesssim z \lesssim 2000$ km, with significant vertical structure. The ionosphere is conventionally divided into layers based on this vertical structure. The D layer occupies the range $60 \lesssim z \lesssim 80$ km, the E layer occupies $80 \lesssim z \lesssim 150$ km, the F_1 layer occupies $150 \lesssim z \lesssim 200$ km, the F_2 layer occupies the region $200 \lesssim z \lesssim 400$ km, and the topside layer occupies the space $400 \lesssim z \lesssim 2000$ km. The mass density of the ionosphere maximizes in the F_2 layer, typically near $z = 300$ km. The ionosphere becomes increasingly rarefied above the F_2 peak, asymptotically joining into the magnetospheric plasmas. At high latitudes ($67° \lesssim \lambda \lesssim 77°$), the ionospheric plasmas merge into the auroral zone plasma, while at lower latitudes ($\lambda \lesssim 67°$) the ionospheric plasmas merge into a region known as the plasmasphere.

[3]This, in turn, is closely related to the level of solar wind activity.

[4]Magnetic mapping relies upon the idea of magnetic field lines, or similarly, magnetic flux tubes. Both of these concepts will be discussed in detail in the next chapter. It is a matter of some debate whether or not it makes sense to think of field lines as moving, lending a certain amount of controversy to popular explanations of some magnetospheric processes.

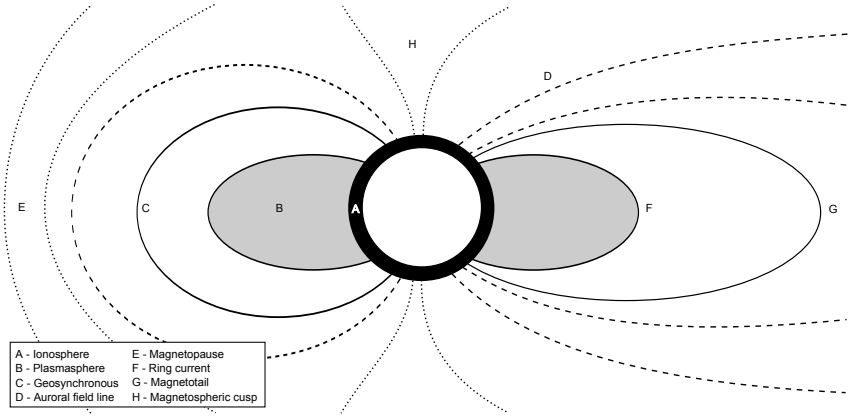

Figure 1.1: A Cartoon Diagram of Earth's Magnetosphere (not to scale)

The Auroral Zone

On the night side, auroral field lines are conjugate to the magnetotail.[5] Since the properties of tail plasmas differ greatly from those in the ionosphere, the profile of plasmas along auroral field lines must vary significantly between the equator and the ionosphere.

The Plasmasphere

The plasmasphere is a toroidal region of cold ($T < 10$ eV) plasma which surrounds the Earth out to a distance of 4-5 Earth radii.[6], populated with low-energy ionospheric plasma which have diffused outward along magnetic field lines.[7] During quiet periods of geomagnetic activity, the density distribution of plasma along magnetic field lines approaches a diffusive equilibrium, although it is subject to erosion from convective

[5]That is, the same field lines pass through both regions.

[6]Earth's radius $\equiv R_E = 6371$ km, by convention.

[7]The majority of the magnetosphere's plasma mass is provided by particles with $T < 100$ eV, the so-called core plasmas[25].

instabilities[25].

The outer boundary of the plasmasphere is called the plasmapause. At least two interpretations of the plasmapause exist. The first, which is more commonly encountered, suggests that the plasmapause is the line at which the convection electric field (due to the inductive effect of the entrained solar wind magnetic field) balances the co-rotation electric field (due to the rotational motion of dipole field lines). Lemaire[40] provides an alternative explanation in terms of a balance between gravity and the centrifugal force arising from co-rotation of the plasma. In either case, the plasmasphere is marked by a steep decline in plasma density over a few thousand kilometers at the equator (and less at higher latitudes). During periods of enhanced activity, the plasmapause is typically pushed inwards; conversely, during periods of prolonged quiet, the plasmapause will expand outwards.

Radiation Belts

In stark contrast to the cold plasmaspheric plasmas, the highly energetic radiation belts constitute a minority population with typical energies $T \gtrsim 200$ keV[86]. Under quiet circumstances, the radiation belts are a remarkably stable population, owing to the strong conservation of certain adiabatic invariants.[8]

Enhancements of the radiation belts are typically associated with compressions of the magnetospheric cavity. These compressions are in turn associated with the previously mentioned magnetic storm phenomena.

[8]The colloquial notion of the adiabatic invariant as a quantity conserved under slow variations in some parameter and the precise mathematical definition (see e.g. Arnold[9]) are not incompatible, but some care needs to be taken in proper definition of the invariant as well as the notion of change. For example, no matter how slowly a particle traverses a region of vanishing magnetic field, the most strongly conserved adiabatic invariant is violated.

1.2 Magnetic Storms

Long before the satellite age, observers had noted a relationship between apparent solar activity and geomagnetic processes. In 1859, Stewart[88] observed a series of brilliant auroral displays in conjunction with variations in the terrestrial magnetic field. Furthermore, Stewart noted that

> [A]t the time of their occurrence a large spot might have been seen on the disc of our luminary, a celestial phenomenon which we have grounds for supposing to be intimately connected with auroral exhibitions and magnetic storms.[88]

As a matter of historical interest, it is possible that Stewart was unfamiliar with Maxwell's theory of electricity[53], which had only been published a few months earlier, in March of 1861. Stewart provided no direct mechanism for the production of geomagnetic disturbances by the sun ("our luminary"), but rather suggested that disturbances were due to solar currents which induced two complementary current systems, a slowly varying one in the Earth's crust and a more rapidly varying one flowing "along the upper strata of the atmosphere"[88].

Later, in his evaluation of an 1862 geomagnetic disturbance, Stewart[89] expanded upon his hypothesis of multiple current systems, using data from deflection magnetograms and telluric current measurements. Although both signals agreed with his theory, Stewart concluded that

> [I]t is lost labour to attempt a quantitative comparison when our observation of the magnetic disturbances and their corresponding earth-currents is

confined to one locality.[89]

Our modern understanding of geomagnetic storms is based upon the resolution of Stewart's troubles - simultaneous multipoint observations at well-instrumented ground observatories, along with in situ observations of associated processes in space. We now know that, in addition to atmospheric and terrestrial currents there are currents in space which can significantly affect observations at the Earth's surface[37].

The Ring Current

We commonly quantify the degree of geomagnetic disturbance by a magnetic storm using the Disturbance Storm-Time (DST) index. The DST index is a weighted average of North-South (N-S) magnetic deflections from a specific set of ground magnetometers. The measured N-S deflection is due to the influence of the ring current, a population of moderately energetic (10-200 keV) trapped ions[37] that drift azimuthally westward.[9]

The composition of the ring current has been observed to depend on the intensity of the magnetic storm, with weaker storms having populations dominated by H^+ of solar wind origin and stronger storms having mainly O^+ of ionospheric origin[14]. Because ionospheric plasmas are cold and gravitationally bound, there must be some mechanism by which the O^+ are removed from low altitudes and accelerated to keV energies. Possible explanations are ponderomotive forcing by large amplitude ultra-low frequency waves[34] and perpendicular heating through wave-particle resonance (cyclotron or lower hybrid, for instance[14]).

The ring current decays by a combination of charge exchange processes and wave-particle

[9]The current resulting from this ion motion induces a N-S magnetic field variation at the Earth's surface which is then used to calculate the DST.

scattering. Electromagnetic ion cyclotron (EMIC) waves cause particle losses by pitch-angle scattering, where the particle's parallel velocity is increased and its perpendicular velocity is decreased while conserving total energy. The net result is a reduction in the angle between the particle's velocity and the magnetic field.[10] Numerical simulations suggest that scattering by EMIC waves may be responsible for a significant fraction ($\sim 10\%$) of ring current losses.

1.3 Substorms

Substorms are arguably the most imprtant dynamical process for regulating the distribution of magnetic and plasma energy in the magnetosphere. The term substorm was introduced by S.-I. Akasofu[2] to describe a particular sequence of auroral phenomena . However, the particular sequence of physical processes to which Akasofu referred had been observed as early as 1902 by Kristian Birkeland, who called referred to it as a polar elementary magnetic storm[87]. In either case, the label refers to a specific series of physical processes which occur during a period of dynamic solar wind - magnetosphere coupling which results in the storage of large amounts of energy in the magnetotail and the subsequent explosive release of that energy. McPherron [55] provided a concise definition of a substorm:

> A magnetospheric substorm is a transient process initiated on the night side of the earth in which a significant amount of energy derived from the solar wind - magnetosphere interaction is deposited in the auroral ionosphere and magnetosphere.

[10] En masse, the result is known as pitch-angle diffusion.

To this day there remain many unanswered questions regarding the physical processes leading to substorm initiation, the sequence of events during a substorm, and the physical mechanisms which produce may of the well known features of a substorm. As it is not the purpose of this work to discuss the particulars of substorm physics, we will avoid topics where we believe any significant amount of controversy is currently thought to exist, opting instead to focus on a well-established phenomenological description of the substorm.

1.3.1 Observational Characteristics

It was long ago noted that substorms appear to proceed through three distinct phases, termed growth, expansion, and recovery.[11]

Growth Phase

The growth phase of a substorm is well correlated with the northward component of the IMF turning southward (i.e. becoming negative.) As previously discussed, this configuration is optimal for day side reconnection. It is believed that enhancement of the day side reconnection rate leads to the erosion of the day side magnetic field and the deposition of magnetic energy in the night side geomagnetic tail. This is consistent with observations of the Earth's auroral oval, which is seen to expand equatorward in the night side, consistent with an increase in the magnetic field strength in the tail. At the same time, spacecraft at geosynchronous orbit observe a decrease in the north/south component and an increase of the sunward/earthward components of the geomagnetic

[11] Substorms, as originally conceived of by Akosofu[2] had only two phases, expansion and recovery. The third phase, growth, was argued for by McPherron[54] based primarily on spacecraft observations. The three-phase model was eventually adopted by the larger community and remains in use today.

field, consistent with the stretching of the night side magnetic field into a more tail-like configuration. This period lasts for about one hour before the beginning of the Expansion phase.

Expansion Phase and Recovery

The onset of a substorm is typically associated with the beginning of the expansion phase. The most equatorward auroral arc experiences a rapid brightening, and this arc then expands poleward and westward. Satellites in the near-Earth magnetotail observe regions of strong localized turbulence, consistent with the development of plasma instabilities in this region. The end of the expansion phase is typically heradled by the dipolarization of the geomagnetic field near geosynchronous orbit, the return of a stretched magnetic field configuration towards a more quiescent dipole configuration. The duration of the expansion phase is approximately one hour, though it may be much shorter or longer (10 minutes - 2 hours) depending on the efficacy of the solar wind-magnetosphere coupling.

The recovery phase of the substorm is characterized by a return of the magnetosphere to its pre-substorm state.

1.3.2 Substorm-Related Magnetic Pulsations

Other reasons aside, magnetic substorms are notable because they are almost exclusively associated with an entire class of magnetic pulsation, the impulsive (Pi) bands.[12] The Pi2 magnetic pulsation has long been recognized as being associated with the onset

[12]The primary exception to this is the Pi1c magnetic pulsation, which occurs on the day side as a consequence of auroral precipitation.

of a substorm[64], and more recently the Pi1b magnetic pulsation has been cited as a high time resolution indicator of substorm onset (see e.g. [58], [59], [79], and references therein). Despite this close temporal association, it is believed that Pi1b and Pi2 are manifestations of different processes associated with the dynamics of substorm onset.[72]

1.4 The Structure of this Thesis

This work is concerned primarily with upper band ULF waves. These waves are typically localized and propagating (unlike lower and middle bands, which are usually resonant standing waves), and they are most often observed in the mid-latitude and auroral ionospheres (nominally $45^\circ \leq \lambda \leq 77^\circ$). In order to understand how the wave fields couple and evolve, we must introduce a basic understanding of linear wave theory for magnetospheric plasmas [Chapter 2], recognize the physical processes giving rise to the waves and their terrestrial manifestations [Chapter 3], and have an understanding of the electrodynamical properties of the ionospheric Alfvén resonator [Chapter 4]. Having established an understanding of the theoretical concepts, we will develop a numerical model with which we can simulate the propagation and development of ULF waves in the mid-latitude magnetosphere [Chapter 5]. We will then use our numerical model to study the development of spatial and temporal structure in the Alfvén resonator [Chapter 6]. Finally, we will summarize the results presented in this thesis and suggest future directions of research [Chapter 7].

Chapter 2

Theoretical Background

2.1 Introduction

Waves with frequencies between 1 and 10^4 mHz are frequently observed at ground-based observatories and in space. This range of frequencies extends from the lowest cavity frequency of the Earth's magnetosphere to (roughly) the Schumann spectrum of the Earth-Ionosphere cavity. Samson[81] divides this interval into three logarithmic decades which we refer to as the lower ($1 \leq f \leq 10$ mHz), middle ($10 \leq f \leq 10^2$ mHz), and upper ($10^2 \leq f \leq 10^4$ mHz) bands. We refer to those signals which are observed on the ground as geomagnetic pulsations, while those in space are referred to as ultra-low frequency (ULF) waves. It is almost always the case that a geomagnetic pulsation can be interpreted as the terrestrial manifestation of a magnetospheric ULF wave, but ULF waves do not always result in the production of a geomagnetic pulsation.

2.2 Terminology

The most elementary concept with which we are concerned is a wave, but one must be mindful not to mistake this elementary concept for simple. What is a wave? It is more than some construct which obeys a wave equation. In the context of this work, "wave" refers to small amplitude perturbation of a magnetized plasma. The cause and properties of this perturbation may be arbitrarily described within the limits of hydromagnetic theory. These perturbations may be propagating, as is the case for impulses, or they may be stationary, as is the case for normal modes. They may vary harmonically with time, as is the case for oscillations, or they may exhibit arbitrary variation as is the case for bursts. It is typically the case that normal modes are oscillatory, and bursts are impulsive, although we will also discuss the interesting case of the impulsive PiC oscillation. It should be noted that oscillatory does not mean sinusoidal, rather that the waveform is characterized by a succession of positive peaks followed by negative troughs; the spacing of the peaks and troughs is, again, arbitrary.

2.3 Fundamental Equations of a Cold Plasma

The Earth's magnetosphere is populated to a great extent by so-called "core plasmas" having thermal energy (W_T) less than 50 eV[25]. Even in a relatively dense plasma ($n = 1000$ cm^{-3}), the thermal energy density of the core ions is only a few percent of the energy density of the magnetic field,

$$\beta = \frac{nW_T}{B^2/2\mu_0} \ll 1 \tag{2.1}$$

Thus the core magnetospheric plasma is said to be "low-β", and this indicates that temperature-driven effects can, to a reasonable level of approximation, be ignored[94].

In the low-β regime, the relevant equations for a magnetized plasma are Newton's law (with s denoting a particle species),

$$m_s \frac{\partial \mathbf{v}_s}{\partial t} = q_s(\mathbf{E} + \mathbf{v}_s \times \mathbf{B}) - \nu_s \mathbf{v}_s \tag{2.2}$$

Faraday's law,

$$\frac{\partial \mathbf{B}}{\partial t} = -\nabla \times \mathbf{E} \tag{2.3}$$

Ampere's law,

$$\frac{1}{c^2}\frac{\partial \mathbf{E}}{\partial t} = \nabla \times \mathbf{B} - \mu_0 \mathbf{J} \tag{2.4}$$

And the definition of current density,

$$\mathbf{J} = \sum_s q_s n_s \mathbf{v}_s \tag{2.5}$$

These equations self-consistently describe perturbations of any magnitude and are fully general (within the limits of the low-β approximation). However, we are interested in studying the effects of small perturbations on an equilibrium system, so we are able to further simplify (2.2)-(2.5) by use the method of linearization.

Linearization

In equilibrium, a cold, stationary plasma can be characterized by its particle densities $n_{s,0}$, drift speeds $\mathbf{v}_{s,0}$, and electromagnetic fields $\mathbf{E}_0$ and $\mathbf{B}_0$.

$$\mathbf{E} \to \mathbf{E}_0 + \mathbf{E}_1 \quad \mathbf{v} \to \mathbf{v}_{s,0} + \mathbf{v}_{s,1} \quad \mathbf{B} \to \mathbf{B}_0 + \mathbf{B}_1 \quad n \to n_{s,0} + n_{s,1} \tag{2.6}$$

We will consider explicitly the case of static equilibrium, where $\mathbf{v}_{s,0} = 0$ and $\mathbf{E}_0 = 0$. In this situation, equations (2.2)-(2.5) can be written as

$$m_s \frac{\partial \mathbf{v}_{s,1}}{\partial t} = q_s(\mathbf{E}_1 + \mathbf{v}_{s,1} \times \mathbf{B}_0) - \nu_s \mathbf{v}_{s,1} \tag{2.7}$$

$$\frac{\partial \mathbf{B}_1}{\partial t} = -\nabla \times \mathbf{E}_1 \tag{2.8}$$

$$\frac{1}{c^2}\frac{\partial \mathbf{E}_1}{\partial t} = \nabla \times \mathbf{B}_1 - \mu_0 \mathbf{J}_1 \tag{2.9}$$

$$\mathbf{J}_1 = \sum_s q_s n_{s,0} \mathbf{v}_{s,1} \tag{2.10}$$

Note also that in equilibrium, the absence of an electric field implies that the charge density of the plasma vanishes. This provides us with the quasi-neutrality condition,

$$\sum_s q_s n_{s,0} = 0 \tag{2.11}$$

2.4 Waves in a Cold Magnetized Plasma

The linear dielectric tensor for a cold plasma with a background magnetic field $\mathbf{B}_0$ can be derived from equations (2.7)-(2.10) by Fourier-transforming the equations in time and relating all the quantities to the electric field. The resultant expression is referred to as the wave equation for a cold plasma[1]. However, in order to obtain a form that is suitable for both theoretical analysis and computation, we will begin by introducing the auxiliary field variables $\mathbf{D}$ and $\mathbf{H}$. In terms of these fields, the linearized Maxwell equations (2.9) is

$$\frac{\partial \mathbf{D}}{\partial t} = \nabla \times \mathbf{H} \tag{2.12}$$

Fourier transforming this equation in time allows us to consider the fields of a single plane wave [2],

$$-i\omega\tilde{\mathbf{D}} = \nabla \times \tilde{\mathbf{H}} \tag{2.13}$$

The auxiliary fields $\tilde{\mathbf{H}}$ and $\tilde{\mathbf{D}}$ are related to the electromagnetic fields by $\tilde{\mathbf{B}} = \tilde{\mathbf{H}}/\mu_0$ and $\tilde{\mathbf{D}} = \epsilon_0 \epsilon \cdot \tilde{\mathbf{E}}$. The dielectric tensor ϵ can be derived from (2.7)-(2.10) using Fourier

[1] From hereon we will suppress the subscript $_1$ for perturbation quantities, letting it be understood that any quantity not explicitly labeled otherwise is a wavelike perturbation on the equilibrium. We will however retain the subscript $_0$ for identifying equilibrium quantities.

[2] See Appendix 1 for more details.

transforms. The explicit form of the dielectric tensor ϵ is given by Samson[81] as

$$\epsilon = \begin{pmatrix} \epsilon_\perp & -i\epsilon_H & 0 \\ i\epsilon_H & \epsilon_\perp & 0 \\ 0 & 0 & \epsilon_\parallel \end{pmatrix} \tag{2.14}$$

With the components being

$$\epsilon_\perp = 1 - \sum_s \frac{\omega_s^2}{\omega^2 - \Omega_s^2} \quad \epsilon_H = -\sum_s \frac{\Omega_s}{\omega} \frac{\omega_s^2}{\omega^2 - \Omega_s^2} \quad \epsilon_\parallel = 1 - \sum_s \frac{\omega_s^2}{\omega^2} \tag{2.15}$$

Where $\omega_s^2 = \omega_{p,s}^2/(1 + i\nu_s/\omega)$ and $\Omega_s = \Omega_{g,s}/(1 + i\nu_s/\omega)$ and $\omega_{p,s}^2 = n_s q_s^2/\epsilon_0 m_s$ and $\Omega_s = q_s B_0/m_s$ are the plasma- and gyro- frequencies for species s.

Note that these expressions (2.14) are accurate for any orthogonal coordinate system[3] as long as $\mathbf{B}_0$ is parallel to the x^3 axis.

Ultra-low frequency waves typically satisfy the inequality $\omega \ll \omega_s$, Ω_s (an important exception is the excitation of sub-gyrofrequency electromagnetic ion cyclotron waves, which we will discuss later). It is possible for the collision frequency to be either lesser or greater than the gyrofrequency. Although it is the case that $\omega > \nu$ (as it is the for most of the magnetosphere), in this case both ω, $\nu_s \ll \Omega_s, \omega_s$ and so both are equally negligible. Acknowledging this, we can write (2.15) as

$$\epsilon_\perp = \epsilon_A + \frac{i\sigma_P}{\epsilon_0 \omega} \quad \epsilon_H = -\frac{i\sigma_H}{\epsilon_0 \omega} \quad \epsilon_\parallel = \epsilon_P + \frac{i\sigma_0}{\epsilon_0 \omega} \tag{2.16}$$

[3]For example, Cartesian ($x^1 = x, x^2 = y, x^3 = z$), Cylinder ($x^1 = s, x^2 = \phi, x^3 = z$), or Dipole ($x^1 = \nu, x^2 = \phi, x^3 = \mu$) coordinates. See Appendix A for more details.

Here we've introduced the collisional dielectric functions and plasma conductivities,

$$\epsilon_A = 1 + \sum_s \frac{\omega_s^2}{\nu_s^2 + \Omega_s^2} \qquad \epsilon_P = 1 - \sum_s \frac{\omega_s^2}{\nu_s^2 + \omega^2} \tag{2.17}$$

$$\sigma_P = \epsilon_0 \sum_s \frac{\omega_s^2 \nu_s}{\nu_s^2 + \Omega_s^2} \quad \sigma_H = \epsilon_0 \sum_s \frac{\omega_s^2 \Omega_s}{\nu_s^2 + \Omega_s^2} \quad \sigma_0 = \epsilon_0 \sum_s \frac{\omega_s^2}{\nu_s} \tag{2.18}$$

These conductivities are useful because they relate the current density in the plasma to the electric field applied to that plasma according to the linear Ohm's Law,

$$\mathbf{J} = \sigma \cdot \mathbf{E} \tag{2.19}$$

(Note that we have ignored ω in relation to ν in the parallel conductivity. This is because the conductivity vanishes when collisions vanish, so the finite-frequency correction is never important in the ULF limit. This is not the case for the parallel dielectric component, however, so we have retained the finite frequency term there.)

2.4.1 Dispersion Relation

If we assume a homogeneous and uniform plasma, we are able to take the Fourier transform of our equations in space, allowing us to replace ∇ by $i\mathbf{k}$ in our expressions. Combining (2.13), (2.19) the above mentioned constitutive relation $\mathbf{D} = \epsilon \cdot \mathbf{E}$, and the Fourier transform of Faraday's Law,

$$\omega \tilde{\mathbf{B}} = \mathbf{k} \times \tilde{\mathbf{E}} \tag{2.20}$$

We can obtain the dispersion relationship for a cold plasma,

$$(\epsilon - n^2\mathbb{I} + \mathbf{nn}) \cdot \tilde{\mathbf{E}} = 0 \tag{2.21}$$

Here $\mathbf{n}$ is the index of refraction vector, defined as $\mathbf{n} = c\mathbf{k}/\omega$. The explicit form of this relationship is

$$\begin{pmatrix} \epsilon_\perp - n^2\cos^2\theta & i\epsilon_H & n^2\sin\theta\cos\theta \\ i\epsilon_H & \epsilon_\perp - n^2 & 0 \\ n^2\sin\theta\cos\theta & 0 & \epsilon_\parallel - n^2\sin^2\theta \end{pmatrix} \cdot \tilde{\mathbf{E}} = 0 \tag{2.22}$$

Where $\theta = \arctan(k_\perp/k_\parallel)$ is the propagation angle.

For non-zero $\mathbf{E}$, the dispersion relationship requires that the determinant of its tensor coefficient vanish[8]. In general, this requires the solution of a third order equation in ω^2. However, significant simplification occurs if we ignore the effects of collisions. It can be seen or easily shown that as $\nu_s \to 0$, $\sigma_s, \epsilon_H \to 0$[4] In this case, the dispersion relationship can be written as

$$(n^2 - \epsilon_\perp)\left(n^2 - \frac{\epsilon_\perp\epsilon_\parallel}{\epsilon_\perp\sin^2\theta + \epsilon_\parallel\cos^2\theta}\right) = 0 \tag{2.23}$$

The parenthetical terms of (2.23) correspond to the magnetosonic and Alfvén waves, respectively. More explicitly, the magnetosonic dispersion relation is

[4]Albeit for somewhat different reasons.

$$\omega^2 = \frac{c^2 k^2}{\epsilon_\perp} \tag{2.24}$$

And the Alfvén wave dispersion relation is

$$\omega^2 = \frac{1}{1 + k_\perp^2 \delta_e^2} \frac{c^2 k_\parallel^2}{\epsilon_\perp} \tag{2.25}$$

Where $\delta_e = c/\omega_p$ is the plasma inertial length.

2.4.2 Parallel Electric Fields

In the framework of space plasma physics, the formation of parallel electric fields is an important dynamical process. However, these electric fields are primarily a small-scale phenomenon and are largely ignorable on the scale sizes of interest for our studies.

The Importance of Parallel Electric Fields

Although the majority of the magnetospheric plasmas are cold, precipitating auroral particles may have keV energies. Although it is possible for particles to be energized by adiabatic processes, the most effective method for providing energy for cold particles is by means of parallel electric fields ($E_\parallel$). There are two primary processes by which an $E_\parallel$ can be established - electrostatic charge separation or wave dynamics. Appreciable charge separation as a linear process is unlikely in most plasmas, owing to quasi-neutrality and the high mobility of electrons along the field line.[5] In this case,

[5] An important exception to this is for strongly rarefied plasmas where ω_p is in the ULF frequency range. In this case, waves with $\omega \sim \omega_P$ can produce charge separation.

wave dynamics are much more likely to contribute to the acceleration of particles. The degree to which the wave energizes the particles is dependent both on the characteristics of the wave and the distribution of particles. However, for the plasmas of interest in this study, we will argue that the interaction of particles and waves via $E_\parallel$ is negligible.

Can $E_\parallel$ Be Ignored?

Dynamically, $E_\parallel$ affects the parallel velocity of particles. The cold plasma assumption excludes the possibility of extreme energization by $E_\parallel$. If we set the upper bound of energies for a cold plasma at 100 eV (corresponding to the upper range of the so-called core plasmas [25]), then we can infer limits on the spatial scale of parallel electric fields. It can be seen from the dispersion relation that $E_\parallel$ depends primarily on $k_\perp$ and the product $k_\perp \delta_e$. Because of the interaction of the wave electric field with the plasma, $E_\parallel$ of the inertial Alfvén wave has the effect of slowing the wave down, thus reducing the frequency for a given wave vector. One straightforward way of quantifying the effect of $E_\parallel$ is therefore its deviation from the non-inertial ($\delta_e = 0$) limit.

Since the wavelength of ULF waves is $\sim V_A/\omega$, where $f < 1$ Hz, $V_A > 500$ km/s,[6], and $\delta_e = 5.31/\sqrt{n}$ km, (typically $n \gg 1$ cm^{-3}) a wave must be propagating almost perpendicular to the background field in order to have appreciable inertial effects. For instance, the frequency of an inertial Alfvén wave differs from $k_\parallel c/\sqrt{\epsilon_\perp}$ by only 1% for $k_x \delta_e = 0.142$. Assuming the wavelength of the wave is approximately $\lambda = c/\sqrt{\epsilon_\perp}\omega$, then the angle at which inertial effects are "important" is $\tan\theta \approx 0.001$ or so. Thus, so long as an Alfvén wave has an angle of propagation of at least 1°[7], it is safe to ignore

[6]The quantity V_A is called the Alfvén speed, defined as $V_A = B_0/\sqrt{\mu_0 \rho_0}$. This is the characteristic speed of hydromagnetic wave propagation, and it will be frequently encountered over the remainder of this work.

[7]Or the plasma is not especially rarefied, as may occur along auroral field lines around 2 R_E.

the inertial effect when considering linear ULF wave properties. For the length scales of interest in this study, we are largely justified in setting $E_{\parallel} = 0$.[8]

2.4.3 Perpendicular Electric Fields

We can inverse Fourier transform the perpendicular components of (2.12), substituting in the electric field and using the dielectric components from (2.16) to obtain

$$\frac{\epsilon_{\perp}}{c^2}\frac{\partial \mathbf{E}_{\perp}}{\partial t} = (\nabla \times \mathbf{B})_{\perp} - \mu_0 \sigma_{\perp} \cdot \mathbf{E}_{\perp} \tag{2.26}$$

Where the perpendicular conductivity tensor $\sigma_{\perp}$ is given by

$$\sigma_{\perp} = \begin{pmatrix} \sigma_P & -\sigma_H \\ \sigma_H & \sigma_P \end{pmatrix} \tag{2.27}$$

2.5 Cold Plasma Hydromagnetics

Large-scale linear perturbations of magnetospheric low-β plasmas are governed by the cold plasma hydromagnetic equations, Faraday's Law and the collisionless Ampere's Law

$$\frac{\partial \mathbf{B}}{\partial t} = -(\nabla \times \mathbf{E}_{\perp}) \tag{2.28}$$

[8] As said S. L. Mandelstahm, "Any approximation eventually revenges itself."[31]

$$\frac{\epsilon_A}{c^2}\frac{\partial \mathbf{E}_\perp}{\partial t} = (\nabla \times \mathbf{B})_\perp \tag{2.29}$$

Where $c_A^2 = c^2/\epsilon_A$ and $\epsilon_A = 1 + c^2/V_A^2$ is the collisionless limit of $\epsilon_\perp$.

Since the electric field parallel to the background magnetic field vanishes in this limit, the current density along the background magnetic field is directly related to the curl of the magnetic field by Ampere's law,

$$J_\parallel = \frac{(\nabla \times \mathbf{B})_\parallel}{\mu_0} \tag{2.30}$$

Let us suppose that the background magnetic field is oriented uniformly in the $\hat{e}_z$ direction, and further suppose that the plasma is uniform in both perpendicular directions. Without a loss of generality, we can consider a wave propagating only in the $x-z$ plane (since we could just rotate our axes to make this true). We refer to this as the slab model of the magnetosphere, a schematic of which is shown in Figure 2.1.

Since the plasma is uniform and the wave propagates only in the $\hat{e}_x$ and $\hat{e}_z$ directions, we can ignore derivatives with respect to the transverse coordinate, y. Thus we find that the components of (2.28)-(2.29) decouple into two sets - E_x, B_y and E_y, B_x, B_z. These two sets of fields correspond to the two fundamental modes in a cold plasma, the Alfvén and magnetosonic waves, respectively.

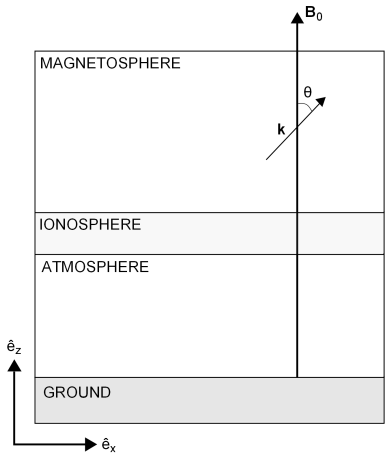

Figure 2.1: Slab Magnetosphere Model for ULF Waves

2.5.1 Alfvén Waves

The Alfvén wave carries electromagnetic energy parallel to the background magnetic field and causes perturbations perpendicular to the the background magnetic field.[9] The Maxwell equations for the Alfvén wave are

$$\frac{1}{c_A^2}\frac{\partial E_x}{\partial t} = -\frac{\partial B_y}{\partial z} \qquad \frac{\partial B_y}{\partial t} = -\frac{\partial E_x}{\partial z} \tag{2.31}$$

If we take the Fourier transform of (2.31), it is a straightforward matter to obtain the Alfvén wave dispersion relation,

$$\omega^2 = c_A^2 k_z^2 \tag{2.32}$$

[9]In the inertial limit, as previously discussed, the Alfvén wave is associated with electric fields parallel to the background magnetic field. This is an important mechanism for providing particle acceleration in the auroral region, but it is outside the scope of this work. See e.g. Thompson[92] for a discussion.

The ratio of the electric and magnetic field can be found from either of the Fourier transformed equations along with the dispersion relation (2.32)

$$\frac{B_y}{E_x} = \frac{1}{c_A} \tag{2.33}$$

This relationship between the transverse electric and magnetic field components is regarded as a characteristic signature of the Alfvén wave. Notice that the wave propagates along the background field (in the $\hat{e}_z$ direction), but it only causes disturbances perpendicular to the background field. It is for this reason that this wave is often referred to as the shear Alfvén wave.

2.5.2 Magnetosonic Waves

The magnetosonic wave, unlike the Alfvén wave, is capable of producing an disturbance parallel to the magnetic field. The Maxwell equations for the magnetosonic wave are

$$\frac{1}{c_A^2}\frac{\partial E_y}{\partial t} = \frac{\partial B_x}{\partial z} - \frac{\partial B_z}{\partial x} \qquad \frac{\partial B_x}{\partial t} = \frac{\partial E_y}{\partial z} \qquad \frac{\partial B_z}{\partial t} = -\frac{\partial E_y}{\partial x} \tag{2.34}$$

As before with the Alfvén wave, if we Fourier transform the Maxwell equations (2.34), we can obtain a dispersion relation for the magnetosonic wave,

$$\frac{\omega}{k} = c_A \tag{2.35}$$

Since the magnetosonic wave has two magnetic field components, there are two electric-magnetic field ratios,

$$\frac{B_x}{E_y} = -\frac{k_z}{k}\frac{1}{c_A} \qquad \frac{B_z}{E_y} = \frac{k_x}{k}\frac{1}{c_A} \tag{2.36}$$

From these polarization relations, it can be seen that the parallel and perpendicular magnetic perturbations are 180° out of phase.[10] As a result, the magnetic field disturbance has a "bottle" geometry.

2.6 Wave Equations in a Dipole Magnetic Field

Close to the Earth, the magnetic field is dominated by the dipole moment of the geomagnetic field. During periods of low geomagnetic activity, the field can be dipolar out to beyond geostationary orbit (r = 6.6 R_E). Because of its applicability to the real space environment, we choose to use this as our plasma model. Fortunately, it is not a particularly difficult system to work with.

2.6.1 The Geomagnetic Dipole Field

The Earth has a uniform dipole moment **M** that we will take to be directed southward along the $\hat{e}_z$ axis. In terms of the spherical (r, θ, φ) coordinates, the magnetic field due to the geomagnetic dipole is

$$\mathbf{B}_D = -\frac{M}{r^3}(2\cos\theta\hat{e}_r + \sin\theta\hat{e}_\theta) \tag{2.37}$$

The magnitude of the dipole field is

[10] This can also be seen from the divergence condition $\nabla \cdot \mathbf{B} = 0 \rightarrow \mathbf{k} \cdot \mathbf{B} = 0$.

$$B_D = M\frac{\sqrt{1+3\cos^2\theta}}{r^3} \tag{2.38}$$

Where $M = R_I^3 B_0$, where R_I is the radius of the Earth's ionosphere and B_0 is equatorial magnetic field at the Earth's ionosphere. Representative values for B_0 and R_I are 30 μT and $R_E = 6461$ km, respectively.

2.6.2 Dipole Coordinates

A particularly good set of dipole field-aligned coordinates is the (ν, ϕ, μ) system of Radoski[78].[11] The dipole coordinates are related to the spherical coordinates by

$$\nu = -\frac{R_I \sin^2\theta}{r} \qquad \phi = \phi \qquad \mu = \frac{R_I^2 \cos\theta}{r^2} \tag{2.39}$$

Note that these coordinates define a right-handed orthogonal system as discussed in the appendix.

Differential Geometry of Dipole Coordinates

For any coordinate system (x^1, x^2, x^3), there exists a set of basis vectors $\varepsilon^i = \nabla x^i$. The contravariant scale factors of the dipole coordinates are defined as the magnitude of the basis vector, $h^i = \sqrt{g^{ii}}$. The contravariant basis vectors for the dipole coordinates (2.39) are

[11] However, we choose to normalize the coordinates to the ionospheric radius rather than the Earth's radius, in anticipation of Chapter 4.

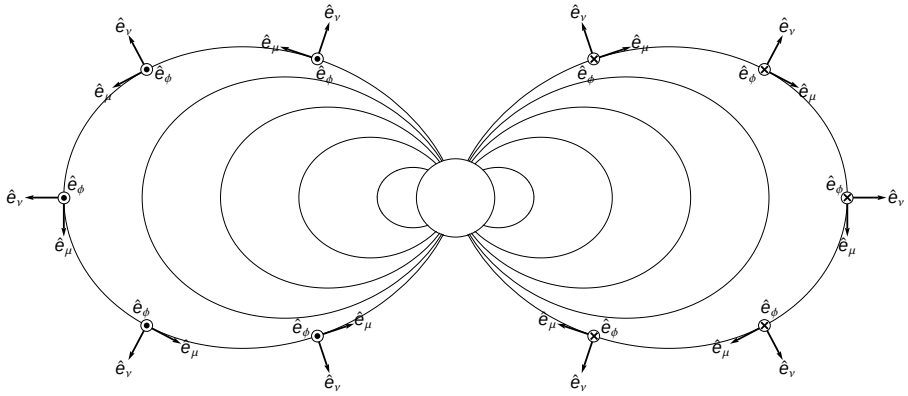

Figure 2.2: Orthogonal Dipole Basis Vectors

$$\varepsilon^{\nu} = h^{\nu}\hat{e}_{\nu} \qquad \varepsilon^{\phi} = h^{\phi}\hat{e}_{\phi} \qquad \varepsilon^{\mu} = h^{\mu}\hat{e}_{\mu} \tag{2.40}$$

Where the $\hat{e}_i$ are the unit vectors for the coordinate x^i, defined in terms of the spherical unit vectors as

$$\hat{e}_{\nu} = \frac{\sin\theta\hat{e}_r - 2\cos\theta\hat{e}_{\theta}}{\sqrt{1+3\cos^2\theta}} \qquad \hat{e}_{\mu} = \frac{2\cos\theta\hat{e}_r + \sin\theta\hat{e}_{\theta}}{\sqrt{1+3\cos^2\theta}} \tag{2.41}$$

And the h^i are the contravariant scale factors,

$$h^{\nu} = \frac{R_I\sin\theta\sqrt{1+3\cos^2\theta}}{r^2} \qquad h^{\phi} = \frac{1}{r\sin\theta} \qquad h^{\mu} = \frac{R_I^2\sqrt{1+3\cos^2\theta}}{r^3} \tag{2.42}$$

Notice that $h^{\mu} = R_I^2 B_D/M$, and that $R_I h^{\nu} h^{\phi} = h^{\mu}$.

The covariant basis vectors are related to the contravariant basis vectors by the contravariant metric tensor,

$$\varepsilon^i = g^{ij}\varepsilon_j \tag{2.43}$$

Where $g^{ij} = \varepsilon^i \cdot \varepsilon^j$. The covariant scale factors are given by $h^i = \sqrt{g^{ii}}$, and it follows from the orthogonality of the dipole coordinates that the covariant and contravariant basis vectors are orthonormal, giving us $h_i = 1/h^i$.

Magnetic Field Lines

The differential length vector is given by $d\ell = \varepsilon_i dx^i$, and so a dipole magnetic field line is defined by

$$d\ell \times \mathbf{B}_D = 0 \tag{2.44}$$

Using the definition of the dipole field (2.37) and assuming ϕ =constant, (2.44) results in a single differential equation for the magnetic field line

$$\frac{dr}{d\theta} = 2r\frac{\cos\theta}{\sin\theta} \tag{2.45}$$

The solution to this equation is

$$\frac{r}{\sin^2\theta} = LR_E \tag{2.46}$$

Here LR_E is the constant of integration, defined such that L is equal to the distance at which the field line crosses the equatorial plane, measured in R_E. This quantity is usually referred to as the L-shell of the magnetic field line, because it actually defines a family of magnetic field lines, requiring the specification of an azimuthal angle to define a particular field line.

It is particularly revealing to note that the dipole coordinate $\nu = -1/LR_E$, as can be seen by comparing (2.39) and (2.46).

Using the definition of the differential length vector, a differential unit of length parallel to the dipole field is given by

$$ds = h_\mu d\mu \tag{2.47}$$

From the definitions of our scale factors and the differential relation for a dipole field line (2.45), it can be shown that

$$\frac{ds}{d\theta} = LR_E \sin\theta \sqrt{1 + 3\cos^2\theta} \tag{2.48}$$

Upon integration, this yields an expression for the total length of a magnetic field line[12]

$$s = \frac{LR_E}{\sqrt{3}} \left(\log\left(\chi + \sqrt{1+\chi^2}\right) + \chi\sqrt{1+\chi^2} \right) \tag{2.49}$$

[12]For $2 \leq L \leq 30$, the length of a field line is given to within 1% by the simple formula $s = 1.15L - 0.63$. The asymptotic form factor for a dipole field line is $\pi_D = 2 + \log(2+\sqrt{3})/\sqrt{3} \approx 2.717$ (defined such that $s = \pi_D L$) The relative oblateness of a dipole field line is represented by the ratio π_D/π, which is always less than 1.

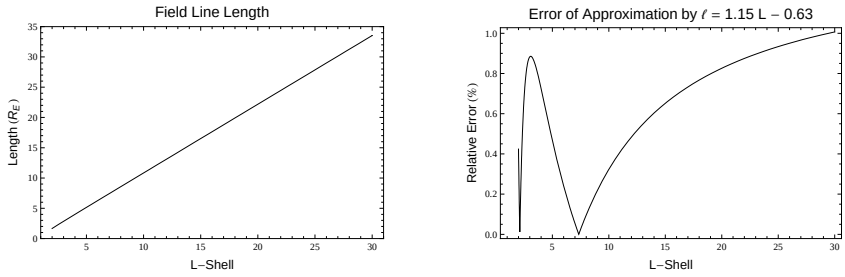

Figure 2.3: Length of a Magnetic Field Line as a Function of L-Shell

Where $\chi = \sqrt{3 - 3/L}$.

Magnetic Flux Conservation

The differential unit of area perpendicular[13] to the dipole magnetic field is

$$d\mathbf{a} = \varepsilon_\nu \times \varepsilon_\phi \, d\nu d\phi \tag{2.50}$$

Since the basis vectors are orthogonal, the scalar differential area is

$$da = h_\nu h_\phi d\nu d\phi \tag{2.51}$$

A dipole magnetic "flux tube" is a volume bounded by surfaces of constant ν and ϕ, so the magnetic flux through any surface perpendicular to the magnetic field line is independent of position along the field line

[13]This is a bit of a misnomer - it's actually parallel to the dipole magnetic field. The direction of the area is determined by its normal vector. Thus, although the area of the plane is along a constant value of the field-aligned coordinate, the area is itself parallel to the field. This is why it makes sense to write the differential magnetic flux as $\mathbf{B}_D \cdot d\mathbf{a}$

$$\Phi_B = \iint B_D da = M\Delta\nu\Delta\phi \tag{2.52}$$

The differential unit of volume is given by

$$dV = Jd\nu d\phi d\mu \tag{2.53}$$

Where $J = h_\nu h_\phi h_\mu$ is the determinant of the Jacobian matrix.

2.6.3 Maxwell's Equations in Dipole Coordinates

In an arbitrary orthogonal[14] coordinate system, Maxwell's equations can be written as

$$\frac{\partial \mathcal{B}^i}{\partial t} = -\frac{\delta^{ijk}}{J}\frac{\partial \mathcal{E}_k}{\partial x^j} \tag{2.54}$$

And

$$\frac{1}{c_A^2}\frac{\partial \mathcal{E}^i}{\partial t} = \frac{\delta^{ijk}}{J}\frac{\partial \mathcal{B}_k}{\partial x^j} \tag{2.55}$$

Where δ^{ijk} is the permutation symbol[15], $\mathcal{E}^i = \varepsilon^i \cdot \mathbf{E}$ and $\mathcal{B}^i = \varepsilon^i \cdot \mathbf{B}$ are the contravariant electric and magnetic fields, and $\mathcal{E}_i = \varepsilon_i \cdot \mathbf{E}$ and $\mathcal{B}_i = \varepsilon_i \cdot \mathbf{B}$ are the covariant electric and magnetic fields.

[14] These are valid for non-orthogonal systems too, so long as the basis vectors are not coplanar. We will exploit this fact when developing a numerical method in Chapter 4.

[15] Since this is an orthogonal coordinate system, $\delta^{ijk} = (\hat{e}_i \times \hat{e}_j \cdot \hat{e}_k$, were $\hat{e}_i$ is a unit vector along the i^{th} coordinate axis. In the more general case, $\delta^{ijk} = J(\varepsilon^i \times \varepsilon^j \cdot \varepsilon^k)$

Note that in these coordinates, B_μ is the compressional magnetic field component associated solely with the magnetosonic wave. The Alfvén wave is characterized by non-zero field-aligned current,

$$J_\mu = \frac{h_\mu}{\mu_0}\left(\frac{\partial \mathcal{B}_\phi}{\partial \nu} - \frac{\partial \mathcal{B}_\nu}{\partial \phi}\right) \tag{2.56}$$

Because they are exclusively associated with a single wave mode, in later chapters we will refer to J_μ and B_μ as the characteristic variables of the ULF wave modes.

Chapter 3

Magnetic Pulsations

3.1 Historical Background

Observations of long period ULF geomagnetic oscillations were made as early as 1741 by Anders Celsius[38] who measured the deflection of compass needles during auroras. Measurements of pulsations during magnetic storms were made by Balfour Stewart[88] in 1859 using the Kew Observatory magnetogram.[1] Sucksdorff and Harang made the first observations of pulsations with few second periods[38], discovering a "string of pearls" pulsation that was later classified as Pc1. A plethora of observations made in subsequent years led a profusion of different pulsation types. A standard nomenclature for pulsations was introduced by a committee of the International Association of Geomagnetism and Aeronomy (IAGA) in 1964[81], and to a large extent this scheme remains in use today.

[1] The sample frequency of both Celcius' and Stewart's observations were $\gtrsim$ 1 minute.

	Pc1	Pc2	Pc3	Pc4	Pc5	Pi1	Pi2
f[mHz]	200-1000	100-200	22-100	7-22	1-7	25-1000	1-25
T[s]	0.2-5	5-10	10-45	45-150	150-1000	1-20	20-1000

Table 3.1: IAGA magnetic pulsation frequency bands

3.2 IAGA Classification

The traditional classification scheme for magnetic pulsations is given in Table 3.1. Although this taxonomy has been updated over time, its use remains widespread due in large part to its ubiquity in the literature. The IAGA scheme is based entirely upon morphological characteristics of the wave forms and spectra, and makes no reference to underlying physical processes. This reflects the fact that very little was really known about the generative mechanisms of these signals even as recently as 1964.[81]

3.2.1 Continuous Pulsations

Pc1-2

Frequently observed at midlatitudes through the Auroral region, Pc1-2 pulsations are related to electromagnetic waves generated in the equatorial region and typically propagate along magnetic field lines to the ionosphere. According to Villante [95], peak Pc1-2 activity occurs near L = 7, with a secondary maximum occurs near the L-shell corresponding to the plasmapause. Observations from the Polar spacecraft have identified Pc1 in the outer dayside magnetosphere at latitudes as high as to L = 20.[18]

The majority of power in the Pc1-2 frequency range is provided by the electromagnetic ion cyclotron (EMIC) instability. The EMIC instability is driven by anisotropies in the

thermal distribution of particles[2] Waves are generated as a consequence of this instability at a frequency near to one of the gyro-resonant frequencies (Ω_s) or an intermediate bi-ion frequency.[3]

Engebretson[18], in agreement with Anderson[5] noted that "that the outer dayside magnetosphere is often near marginal stability for [EMIC] wave generation." As a consequence, even minor compressions of the magnetosphere - resulting, for example, from enhancements of the solar wind dynamic pressure - can produce conditions favorable for the generation of EMIC waves at sub-auroral latitudes. Statistical studies have found that EMIC occur nearly five times more often during magnetic storms than geomagnetically quiet periods. A superposed epoch analysis by Fraser et al.[21] found that 78% of magnetic storm onsets were accompanied by EMIC activity, but these waves only accounted for 29% of the overall EMIC wave activity during the storm, indicating that the changes in geomagnetic conditions associated with magnetic storms (e.g. compression, enhancement of the ring current) are indeed effective at stimulating and maintaining conditions favorable for EMIC wave generation.

A particularly interesting subtype of the Pc1 pulsation is the pearl pulsation. First identified by Sucksdorff and Harang in 1936[38], the pearl is characterized by a distinctive low frequency ($\leq$ 10 mHz) amplitude modulation.[4] It was originally thought that this modulation arose from the bouncing of a wave packet between conjugate ionospheres[63] with the amplitude increasing as the wave passed through the EMIC-unstable equatorial region. However, conjugate ground-space observations along with improved models of

[2]If we define the anisotropy to be $A = (T_\parallel - T_\perp)/(T_\parallel + T_\perp)$, then the EMIC instability can grow only if $A < 0$.

[3]For example, if the plasma is composed of two species, Hydrogen and Oxygen, then there is a Hydrogen-Oxygen bi-ion resonance whose frequency satisfies $\Omega_O < \omega_{O,H} < \Omega_H$.

[4]Because of the amplitude modulation and the rapid oscillation of the modulated signal, the waveform of a pearl pulsation bears a resemblance to beads on a string, or more grandly, a pearl necklace. Hence the name.

magnetospheric wave propagation indicate that the time scales of the bounce mechanism do not agree with the observed modulation periods[60]. Instead, it has been suggested that longer period Pc5 ULF oscillations cause periodic destabilization of the equatorial plasma. Observations[60],[61] appear to support this hypothesis, but the particular mechanism of pearl generation is still a matter of debate.

In addition to equatorial EMIC signals, there are transverse oscillating shear modes (cavity modes) and a transverse-propagating compressional modes (waveguide modes) whose frequency spectra overlap the Pc 1-2 range. We study the spectrum of these modes in Chapter 4. However, it should be noted that in the absence of magnetospheric convection or some other suitable driver energy source (e.g. energetic particle precipitation), the ionosphere is not a generator of pulsations. Instead, the Alfvén resonator filters pre-existing signals[15],[76] and may even structure incident waves. As a consequence, it makes sense to think of a non-driven IAR as modifying externally imposed signals, and we will study this in detail in Chapter 6.

Pc3-5 (Hydromagnetic Resonances)

The Earth's dipole magnetic field lines are a bounded plasma system, and as such support a spectrum of oscillations. The frequency of oscillation is dependent primarily upon the length of the field line and the Alfvén speed distribution along the field line, although there is an additional dependence on the conditions at each end of the field line, and the wavelength is naturally determined by the length of a given field line. We will discuss the effects of finite ionospheric conductance later in this chapter, but if the ionosphere is taken to be infinitely conducting, then it is possible to solve the coupled Maxwell equations to determine the eigenfrequency, or equivalently the eigenperiod, of an Alfvén wave on a given magnetic field line. As can be seen in Figure 3.1, for

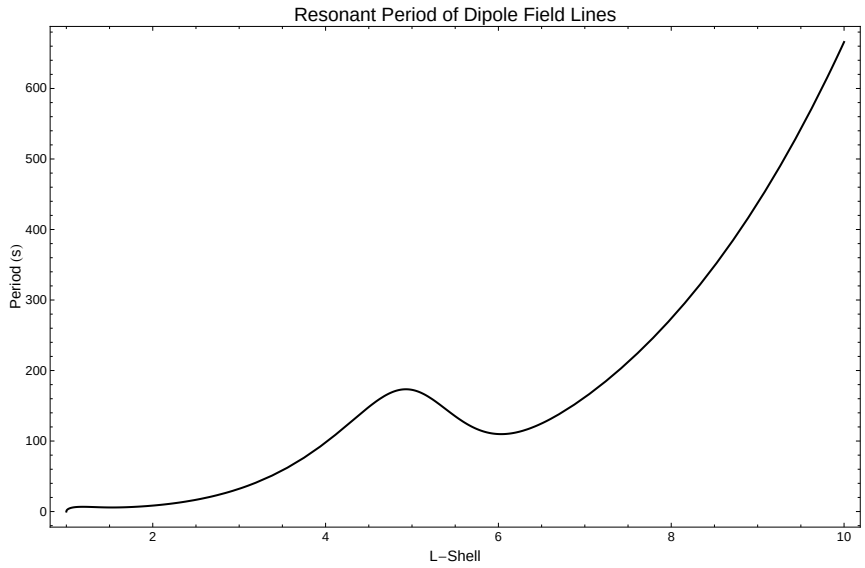

Figure 3.1: Magnetic Field Line Eigenperiod as a Function of L-Shell. Values were obtained by solving the $m = 0$ toroidal wave equation with Dirichlet boundary conditions. Assumes a two-species density model (see Appendix D) with plasmapause at L=4.4.

$L \gtrsim 4$ the field line eigenperiod is squarely within the Pc3-5 range given in Table 3.1. This relationship between pulsations and field line resonances (FLRs) has been long recognized. A good review on the subject is given by Cummings[96], who additionally provides a theoretical analysis of these waves' properties for a variety of plasma density profiles.

The FLR oscillation frequency is closely related to the Alfvénic travel time between hemispheres, defined as $\tau = \oint d\ell/V_A$ [85], and some authors have even taken the two quantities to identical. However close the travel time may be to approximating the actual FLR frequency, it is inaccurate at low latitudes when a significant fraction of the field line is embedded in the strongly inhomogeneous ionospheric plasma.[5]

[5]The same effects are operating at high altitudes, but the proportion of the field line affected is much smaller.

Notice that the resonant frequency of an $L = 6$ magnetic field line as given in Figure 3.1 is approximately 100 seconds, which agrees with the observed modulation frequency of Pc1 pearls noted in our discussion above. There are two characteristic polarizations of FLR, the toroidal and poloidal modes. The toroidal mode is characterized by velocity perturbations in the azimuthal direction, while the poloidal has a radial velocity perturbation.[6] These wave modes are typically limited to a narrow region of space around the resonant L-shell (where the wave period equals the FLR period), but theory and modeling indicate that the toroidal mode is longer-lived[51] and likely more important for EMIC excitation, although both modes have been observed in conjunction with Pc1[60].

3.2.2 Irregular Pulsations

Although the original IAGA system included only a Pi1 classification, it has since become standard to differentiate between two different sorts of Pi1 pulsation based upon the width of the associated frequency spectrum. Signals with power across a broad range of frequencies are typically referred to as Pi1b[7], while irregular pulsations with a narrow range of frequencies are usually referred to as Pi1c.[8]

Pi1b (Bursty)

Often referred to as noise bursts, the broadband character of the Pi1b pulsation likely arises from some manner of current driven turbulence, although the present state of observations is not such that any particular mechanism is indicated. Pi1b pulsations

[6] Actually, this is true only at the equator. In general, the velocity perturbation is directed towards the field line's center of curvature.

[7] Here b nominally stands for bursty, but we tend to favor broad-band, since this is the defining characteristic of the pulsation.

[8] Somewhat paradoxically, c stands for continuous.

are typically observed in conjunction with large-amplitude field-aligned currents and electron precipitation. As previously mentioned, these "noise bursts" are characterized by a broadband frequency spectrum. However, many authors have noted the presence of an embedded spectrum of harmonics with enhanced power[43],[44]. In addition, Posch[72] has shown that Pi1b are frequently observed within two minute of substorm onset (as determined by optical emissions), indicating that they may be useful as a marker of substorm onset.

Given their association with the onset of magnetospheric substorms and their broadband nature, it is reasonable to assume that Pi1b are generated by current-driven turbulence in the upper ionosphere[68] or in the near-Earth magnetotail. There are very few in situ observations of Pi1b in the tail, but Lessard[41] has found evidence of Pi1b signatures in data from the geosynchronous GOES satellites. Interestingly, although the waves were observed to be magnetosonic at GOES, conjugate observations by the FAST satellite indicated that the waves were primarily Alfénic. It has been hypothesized that this indicates some sort of magnetosonic-Alfvén wave coupling process, such as a resonant conversion by finite-frequency effects[67]. An alternative mechanism for the generation of Pi1b in the near-Earth ionosphere has been suggested by Lysak[44], who notes that the characteristics of waves generated by the Ionospheric Feedback Instability are consistent with observations of Pi1b.

Pi1c (Continuous)

Unlike the Pi1b pulsations, Pi1c are fairly well understood. There are two distinct maxima in the occurence of Pi1c - near midnight and in the morning, near 7 MLT. Morningside Pi1c are related to temporal modulations of the auroral zone conductances, and consequently they are often referred to as precipitation pulsations. Nightside Pi1c

are somehow related to the occurence of Pi1b - it is not uncommon to observe Pi1c along side Pi1b, but nightside Pi1c are never observed independent of Pi1b.

Pi2

As mentioned in Chapter 1 Pulsations of the Pi2 type are associated with the onset of magnetic substorms. These pulsations are typically generated by one of two mechanisms. The first of these has been termed the Transient Response mechanism[11] while the second is similar to the Impulse Excitation mechanism for Pc3 pulsations.

The disruption of cross-tail currents that accompanies the onset of a magnetic substorm results in the launching of large amplitude field aligned currents (FACs). These FACs are carried by Alfvén waves which serve to communicate the magnetic stresses in the tail along magnetic field lines to the Earth's ionosphere. At the ionosphere, these waves are partially reflected, resulting in the launching of a second Alfvén wave tailward. The wave will then travel along the magnetic field line to the conjugate hemisphere, where it is again partially reflected.

At lower latitudes, it has been theorized that Pi2 may be caused by oscillations of the plasmaspheric cavity. Much as an inwardly propagating compressional impulse can excite an oscillation of a magnetic shell (field line resonance), the plasmapause represents a somewhat effective barrier to the propagation of ULF waves with certain frequency and scale length characteristics. Energy from these waves goes into setting up a global oscillation of the inner magnetosphere, resulting in the generation of a monochromatic signal across a broad range of L-shells.(See e.g. [91])

3.3 ULF Waves and the Ionosphere

The subject of this chapter, magnetic pulsations, are the terrestrial manifestation of ULF wave-driven ionospheric currents. In order to properly understand and model processes in the IAR which may affect pulsation characteristics, we much first describe the electrodynamics of the ionospheric interaction.

3.3.1 The Ionosphere

Collisional Conductivity

We introduced the conductivity tensor in Chapter 2, noting that in the presence of collisions, the imaginary part of the dielectric tensor becomes comparable to - if not larger than - the real part (it is zero in the absence of collisions, in fluid theory). We can demonstrate this by examining, for example, the perpendicular dielectric component $\epsilon_\perp$ defined in equation (2.15),

$$\epsilon_\perp = 1 - \sum_s \frac{\omega_s^2}{(\omega + i\nu_s)^2 - \Omega_s^2}\left(1 + i\frac{\nu_s}{\omega}\right) \tag{3.1}$$

If the collision frequency for every particle is much greater than the wave frequency, then we find

$$\epsilon_\perp = 1 + i\frac{\sigma_P}{\epsilon_0\omega} \tag{3.2}$$

Where σ_P is the Pedersen conductivity[9] defined in equation (2.18). In the opposite limit, we have

$$\epsilon_\perp = 1 + c^2/V_A^2 \tag{3.3}$$

(Provided that $\omega \ll \Omega_s$, which is generally the case for the waves in which we are interested.)

Based on the ratio of (3.2) to (3.3) we expect the effects of conductivity to be important when $k^2\delta_P^2 \lesssim 1$, where the $\delta_P = \sqrt{2/\mu_0\omega\sigma_P}$ is the Pedersen skin depth. For a 200 mHz Alfvén wave with wavelength 1 R_E, this implies that conductivity is important for values on the order of 10^{-6} Mho/m or greater, values which are characteristic of the ionosphere below 200 km. Consequently, the region in which conductivity effects are important is smaller than the wavelength of most hydromagnetic wave of interest for this study, although they may be important for waves having frequencies near 1 Hz[46],[47].

If we regard the conducting ionosphere as a thin layer of anisotropic conductor, then we may represent its effects using the electrodynamic jump conditions[48].

$$\hat{e}_n \times \Delta\mathbf{B}_\perp = \mu_0\Sigma_\perp \cdot \mathbf{E} \qquad \hat{e}_n \cdot \Delta\mathbf{B} = 0 \tag{3.4}$$

Here Δ indicates the difference of the fields above and below the ionosphere, and $\Sigma_\perp$ is the perpendicular conductance tensor,

[9]Named for the pioneering Danish electrical engineer Peder Oluf Pedersen.

$$\Sigma_\perp = \begin{pmatrix} \Sigma_P & -\Sigma_H \\ \Sigma_H & \Sigma_P \end{pmatrix} \tag{3.5}$$

Where the conductances are defined as the integration over the conducting layer of the corresponding conductivities,

$$\Sigma_P = \int_{h_0}^{h_1} \sigma_P \, dh \qquad \Sigma_H = \int_{h_0}^{h_1} \sigma_H \, dh \tag{3.6}$$

Ionospheric Currents

There are two primary types of electric-field driven perpendicular currents in the ionosphere, the Pedersen and Hall currents. Instead of the vector-matrix equation $\mathbf{J} = \sigma \cdot \mathbf{E}$, the currents and electric fields may be related by the pure vector equation

$$\mathbf{J} = \sigma_P \mathbf{E} + \sigma_H \hat{e}_B \times \mathbf{E} \tag{3.7}$$

Where $\hat{e}_B = \mathbf{B}_0 / B_0$ is a unit vector in the direction of the background magnetic field. From this expression, we see that the Pedersen currents are directly driven by the electric fields in the direction of the electric field, while the Hall currents are driven in a direction that is perpendicular to both the background magnetic field and the applied electric field. In static and quasi-static situations, only Pedersen currents are able to close field aligned currents flowing into the ionosphere. When inductive effects are accounted for, this is not necessarily the case.[99]

3.3.2 Slab Model of the Ionosphere

The expressions introduced in the previous section are nominally valid for any conductor geometry, but they're most useful when the conductor is a uniform surface with uniform thickness. The two most commonly encountered of such geometries are the slab and spherical geometries, both of which can be applied to the Earth's ionosphere in certain situations. However, since the physics is the same and the mathematics is more straightforward, we will consider the slab geometry first.

Let us consider a system where the magnetic field is directed uniformly in the $\hat{e}_z$ direction. We let the ionosphere be situated at $z = 0$, and we take the surface the earth to be at $z = -H$. For all $z > 0$, we take the plasma to be described by a uniform dielectric constant $\epsilon_\perp$.

Fields Below the Ionosphere

From a plasma point of view, the region of space below the Earth's ionosphere is essentially a vacuum - the concentration of charged particles is very small, making it difficult to support currents of any sort. Moreover, since the ionospheric Alfvén speed is much smaller than the speed of light ($V_A/c \sim 0.01$), signals propagate from the ionosphere to the ground in times much shorter than a wave period. This allows us to disregard the time dependence of the fields in the atmosphere, allowing us to use a magnetostatic description, since $\nabla \times \mathbf{B} = 0$ and $\nabla \cdot \mathbf{B} = 0$. It follows from these expressions that the atmospheric magnetic field can be derived from a scalar potential, $\mathbf{B} = \nabla\Psi$ and that scalar potential satisfies Laplace's equation $\nabla^2\Psi = 0$.

If the wave fields above the ionosphere are assumed to vary as $e^{ik_\perp x}$, then it is reasonable

to assume that the scalar potential in the atmosphere has the same dependence[10]. Consequently, we can write the Laplace equation for the scalar potential as

$$\frac{\partial^2 \Psi}{\partial z^2} - k^2 \Psi = 0 \tag{3.8}$$

The solution to this equation is $\Psi = e^{ik_\perp x}(c_1 \sinh(k_\perp z) + c_2 \cosh(k_\perp z))$, where c_1 and c_2 are chosen to satisfy the boundary conditions at $z = -H$ (the ground) and $z = 0$ (the ionosphere). The Earth is a strong conductor, so we should have the normal component of the perturbation magnetic field vanish at the ground.[11] Letting ^{A} denote atmospheric fields and ^{M} magnetospheric fields, We therefore have two boundary conditions, $B_z^A(-H) = 0$ and $B_z^A(0) = B_z^M$ with which we can determine our potential.[12] The condition at $z = -H$ implies that $c_2 = c_1 \coth(k_\perp H)$, and the condition at $z = 0$ implies that $c_1 = B_z/k_\perp$. After a little algebra, the scalar potential can be written as[49]

$$\psi = \frac{B_z^M}{k} \frac{\cosh(k_\perp(z + H))}{\sinh(k_\perp H)} \tag{3.9}$$

The perpendicular fields below the ionosphere are given by

$$B_x^A = i \frac{B_z^M}{\tanh(k_\perp H)} \qquad B_y^A = 0 \tag{3.10}$$

[10]For a uniform plasma, this is a generally applicable assumption, because a suitable rotation can always align the coordinate axes along the wave vector. Moreover, we can always represent an arbitrary signal with complicated horizontal structure using a superposition of different k values.

[11]For finite ground conductivity, this is not the case.

[12]These are Neumann BCs, since $\partial\Psi/\partial z = B_z$.

Fukushima Shielding Effect

Consider a plane Alfvén wave incident on a uniform ionosphere. It was shown by Fukushima [24] that in the absence of Hall currents, such a wave will generate no magnetic signature below the ionosphere. This shielding arises from the exact cancellation of the wave-associated fields by the current-associated fields. We refer to this as the Fukushima Shielding Effect (FSE).

It can be seen that the FSE follows directly from (3.10) with a pure Alfvén wave, since $B_z = 0$ regardless of propagation direction. If Hall conductance is not ignored, then the Alfvén wave will drive Hall currents which in turn produce a ground-observable magnetosonic wave.[13]

Imperfect Fukushima Shield Effect from Field Tilt

As we will discuss in greater detail in subsequent chapters, the Earth's magnetic field is typically inclined with respect to the ionospheric boundary. In this situation, it is possible for the fields associated with the Alfvén wave to penetrate directly to the ground. Suppose that the background field is inclined at an angle α with respect to the vertical, $\mathbf{B}_0 = B_0(\sin\alpha, 0, \cos\alpha)$. The most general wave vector is $\mathbf{k} = (k_x, k_y, k_z)$, since we must allow for the wave to propagate out of the plane of the inclined field.[14] Let us introduce a field-aligned coordinate system, with $\hat{e}_\tau = \cos\alpha\hat{e}_x - \sin\alpha\hat{e}_z$ and $\hat{e}_B = \sin\alpha\hat{e}_x + \cos\alpha\hat{e}_z$. In the ideal MHD approximation, the Alfvén wave fields satisfy $\hat{e}_B \cdot \mathbf{E} = 0$ and $\hat{e}_B \cdot \mathbf{B} = 0$.

[13] A normally incident magnetosonic wave also generates no ground signature, since $B_z \propto k_\perp$. Consequently, a normally incident Alfvén wave would never produce a ground signature in this situation.

[14] Contrast this to the case of the vertical field, when it suffices to consider just one transverse direction.

The divergence-free condition on magnetic fields $\nabla \cdot \mathbf{B} = 0$ applied to the Alfvén wave magnetic field gives us

$$B_\tau = -\frac{k_y}{k_\tau} B_y \tag{3.11}$$

Where $k_\tau = \hat{e}_\tau \cdot \mathbf{k}$.

At the ionospheric boundary, the jump condition requires that $\hat{e}_z \cdot \Delta\mathbf{B} = 0$. This allows us to determine the magnetic potential below the atmosphere (noting $\hat{e}_z \cdot \hat{e}_\tau = -\sin\alpha$) as

$$\Psi = \sin\alpha \frac{k_y}{k_\tau} \frac{B_y}{k_\perp} \frac{\cosh(k_\perp z)}{\sinh(k_\perp h)} \tag{3.12}$$

Where $k_\perp = \sqrt{k_x^2 + k_y^2}$ is the wave vector perpendicular to the ionospheric normal. Notice that there is no ground signal if the wave is propagating only in the meridian of the magnetic field ($k_y = 0$) or if the field is vertical ($\sin\alpha = 0$). It is, however, still due only to the fields of an Alfvén wave, since we have strictly required $\mathbf{B}_0 \cdot \mathbf{B} = 0$ while allowing for an arbitrary wave vector.

The transverse magnetic fields at the ground are given by $\mathbf{B}_\perp^g = i\mathbf{k}_\perp \Psi(0)$, with $\mathbf{k}_\perp = (k_x, k_y, 0)$. If an Alfvén wave generates a ground signature, it will always result in a field in the direction transverse to the plane of the background field; the ratio of the magnetospheric field to this transverse ground field is

$$\frac{B_y^g}{B_y} = i \frac{\sin\alpha}{\sinh(k_\perp h)} \frac{k_y^2}{k_\perp k_\tau} \tag{3.13}$$

Having noted the existence of this penetration effect, we will limit our consideration to strictly vertical fields for the remainder of this chapter. A good discussion of the general case can be found in [83].

Hughes Rotation

The interpretation of ground signals is complicated by the details of the ionospheric interaction. Consider an incident Alfvén wave. A pure Alfvén wave generates no ground signature, as per Fukushima's theorem. However, the ionospheric Hall currents produce a secondary magnetosonic wave which does produce observable effects. Because this is a magnetosonic wave, the associated magnetic field is B_x, whereas the magnetospheric Alfvén wave was associated with B_y. In general, the Hall currents have the effect of producing a ground signature which is rotated 90^o with respect to the incident signal. We refer to this phenomenon as Hughes Rotation, after W. J. Hughes whose theoretical study[33] first elucidated the effect.

Note that Hughes Rotation is not a proper rotation in the classical mechanical sense[27], since the conductance matrix is neither unitary nor orthogonal. Moreover, although it is possible to express the conductance matrix as the composition of a scaling by $\sqrt{\Sigma_P^2 + \Sigma_H^2}$ and a rotation by $\beta = \tan^{-1}(\Sigma_H/\Sigma_P)$, the different polarization relationships for Alfvén and magnetosonic wave components prevent the relationship between the magnetospheric and atmospheric fields from being expressed as a (scaled) rotation. However, in the case of a pure wave mode, the net effect is a scaled rotation by 90^o.

Numerical simulations by Lysak[46] have demonstrated that Hughes rotation is robust even in the presence of a distributed and vertically inhomogeneous ionosphere.

Atmospheric Shielding Effect

Although the ionosphere is regarded as a good conductor, the integrated effect of Earth's surface is typically a much better one (practically perfect at ULF wave frequencies). The space between the ionosphere and the ground is, to a good approximation, non-ionized and an effective insulator. As a consequence, the speed of electromagnetic waves propagation below the ionosphere is the speed of light, which is much faster than the Alfvén speed above the ionosphere.[15]

Consider an Alfvén wave incident on the ionosphere. What we wish to know is the relationship of the ground magnetic field to the magnetospheric field. Consistent with the above arguments, we ignore the effects of E_y and the currents it drives, as well as the associated magnetic field B_x (they are non-zero, but significantly smaller than the other terms). The electrodynamic boundary conditions are (assuming plane-wave variation in $\hat{e}_x$-direction),

$$\tilde{\Sigma}_P E_x = -V_A B_y \tag{3.14}$$

$$\tilde{\Sigma}_H E_x = -B_x^{ATM} \tag{3.15}$$

Notice that the magnetic field of interest below the ionosphere is B_x, due to the Hughes rotation effect.[16] The atmospheric electric field is related to the ionospheric compressional magnetic field (created by Alfvén wave-driven Hall currents) by

[15] It is because of this that the magnetostatic assumption is permissible.

[16] Although formally non-zero, it can be shown that the B_y magnetic field is much smaller than B_x.

$$B_x^{ATM} = iB_z^I \coth(k_x h) \tag{3.16}$$

And the ground magnetic field is related to the same compressional magnetic field by

$$B_x^g = i\frac{B_z^I}{\sinh(k_x h)} \tag{3.17}$$

Combining equations (3.14)-(3.17), we obtain an expression relating the magnetospheric magnetic field to the ground magnetic field,

$$\frac{B_x^g}{B_y} = \frac{1}{\cosh(k_x h)}\frac{\Sigma_H}{\Sigma_P} \tag{3.18}$$

Our result differs somewhat from that of Hughes et al.[33], who considered a somewhat more complicated problem including a finite-width Hall region and the contribution from finite parallel electric fields. However, our result does agree with that of Nishida[17] in the limit $kh \gg 1$ (the conditions of Nishida's derivation), since $1/\cosh(kh) \approx 2e^{-kh}$ for large $k_x h$.[18]

Note that the ASE geometrical attention factor is different from that arising from the imperfect FSE, differing by a factor of $\tanh(k_\perp h)$. Since $-1 \leq \tanh(k_\perp h) \leq 1$, this implies that the atmospheric attenuation of the secondary signal is always greater than that of the primary one. This can be understood as being a difference in the type of source responsible for each signal. The imperfect FSE signal is due to a plane current

[17] As reported by Sciffer et al. [83]

[18] Since we do not need to consider the effects of either a distributed Hall layer or parallel electric fields in the frequency and wavelength regime in which we are concerned, we prefer (3.18) to the more general result of Hughes et al.

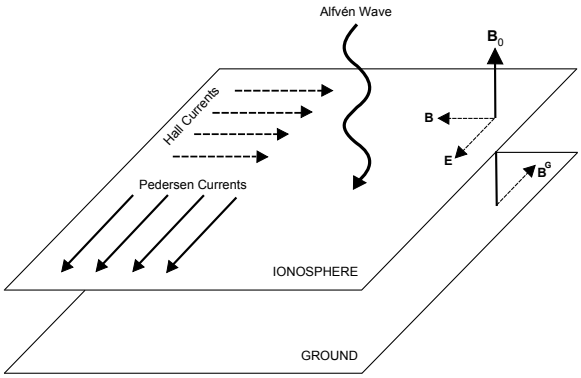

Figure 3.2: Ionospheric Currents and Associated Fields for an Incident Alfvén Wave

sheet, thus producing a signal which drops off roughly as r^{-1}. On the other hand, the ASE field arises from a Hall current loop, producing a dipolar field which drops off (again, roughly) as r^{-3}.

3.4 Wave Reflection and Transformation

Let us consider a hydromagnetic wave with arbitrary components incident on the ionosphere. We would like to determine how much of the wave is reflected, how much is transmitted, and how much is lost (via resistive heating of the ionosphere). As before, we assume that the wave has perpendicular dependence $e^{ik_\perp x}$, but we now suppose that it's parallel dependence is $e^{ik_\parallel z}$. A similar derivation can be found in both Yoshikawa[99] and Sciffer[82].

3.4.1 Derivation of the Reflection Matrix

The electromagnetic jump conditions (3.4) can be combined with the hydromagnetic equations for a cold plasma (2.28)-(2.29) and the atmospheric solution (3.10) to give us

$$\Sigma_\perp \cdot \begin{pmatrix} E_x \\ E_y \end{pmatrix} = -\Sigma_A \begin{pmatrix} k_\parallel V_A/\omega & 0 \\ 0 & k_\parallel V_A/\omega - \alpha \end{pmatrix} \begin{pmatrix} E_x \\ E_y \end{pmatrix} \tag{3.19}$$

Where $\Sigma_A = 1/\mu_0 V_A$ is the Alfvén conductance and $\alpha = ik_\perp V_A/\omega \tanh(k_\perp H)$. At this point, it is helpful also to introduce an atmospheric conductance, $\Sigma_{ATM} = \alpha\Sigma_A$, to represent effect of a finite-thickness atmosphere.

Note that the quantity $k_z V_A/\omega$ is in general different for Alfvén and magnetosonic waves. Using the dispersion relationship (2.24), we can show that $k_z = -i\sqrt{k_x^2 - \omega^2/V_A^2}$. We define the magnetosonic conductance to be

$$\Sigma_M = -i\Sigma_A \sqrt{k_x^2 V_A^2/\omega^2 - 1} \tag{3.20}$$

Waves incident on the ionosphere have $k_\parallel = -k_z$, while reflected waves have $k_\parallel = k_z$. We can decompose the wave fields as the sum of incident and reflected components, and then write (3.19) as

$$\begin{pmatrix} \Sigma_P - \Sigma_A & -\Sigma_H \\ \Sigma_H & \Sigma_P - \Sigma_M + \Sigma_{ATM} \end{pmatrix} \cdot \mathbf{E}^i = \\ - \begin{pmatrix} \Sigma_P + \Sigma_A & -\Sigma_H \\ \Sigma_H & \Sigma_P + \Sigma_M + \Sigma_{ATM} \end{pmatrix} \cdot \mathbf{E}^r \tag{3.21}$$

Where ^{i} denotes the incident wave fields and ^{r} denotes the reflected wave fields. We can solve this for the reflected waves, finding

$$\mathbf{E}^r = \begin{pmatrix} R_{xx} & T_{yx} \\ T_{xy} & R_{yy} \end{pmatrix} \cdot \mathbf{E}^i \tag{3.22}$$

The components of the reflection matrix can be written as

$$R_{xx} = \frac{\Sigma_A - \Sigma_P - \Sigma_{xy}}{\Sigma_A + \Sigma_P + \Sigma_{yx}} \tag{3.23}$$

$$R_{yy} = \frac{\Sigma_F - \Sigma_P - \Sigma_{yx}}{\Sigma_F + \Sigma_P + \Sigma_{xy}} \tag{3.24}$$

$$T_{yx} = (1 + R_{xx}) \frac{\Sigma_{yx}}{\Sigma_H} \tag{3.25}$$

$$T_{xy} = (1 + R_{yy}) \frac{\Sigma_{ATM} - \Sigma_{xy}}{\Sigma_H} \tag{3.26}$$

Where Σ_{yx} and Σ_{xy} are given by

$$\Sigma_{xy} = \Sigma_{ATM} + \frac{\Sigma_H^2}{\Sigma_A + \Sigma_P} \qquad \Sigma_{yx} = \frac{\Sigma_H^2}{\Sigma_P + \Sigma_M + \Sigma_{ATM}} \tag{3.27}$$

These expressions agree with those given by Lysak and Yoshikawa[50], apart from minor differences in notation.

The components of the reflection matrix are complicated functions of the atmospheric and wave parameters, but their basic properties are conceptually straightforward. The diagonal terms R_{xx} and R_{yy} represent the direct reflection of Alfvén and Magnetosonic waves while the off-diagonal terms T_{xy} and T_{yx} quantify the transformation of Alfvén waves to Magnetosonic waves and vice versa.

Wave reflection is normally associated with Pedersen conductance, although R_{xx} and R_{yy} depend just as strongly on the Hall conductance. Wave transformation is truly dependent on the Hall conductance, however - in the limit $\tilde{\Sigma}_H \to 0$, the coupling terms disappear.

In the absence of Hall effects (formally equivalent to a normally incident wave), the reflection matrix simplifies to a scalar relationship,

$$\mathbf{E}^r = \frac{\Sigma_A - \Sigma_P}{\Sigma_A + \Sigma_P}\mathbf{E}^i \tag{3.28}$$

Note that this expression is valid for any type of hydromagnetic wave, since $\Sigma_M = \Sigma_A$ when $k_x = 0$.

3.4.2 Fields Resulting from Wave Reflection

A wave incident on the ionosphere goes as $e^{-ik_z z}$ while an outgoing wave goes as $e^{ik_z z}$. If an Alfvén wave is incident on the ionosphere, then the total electric field is given by

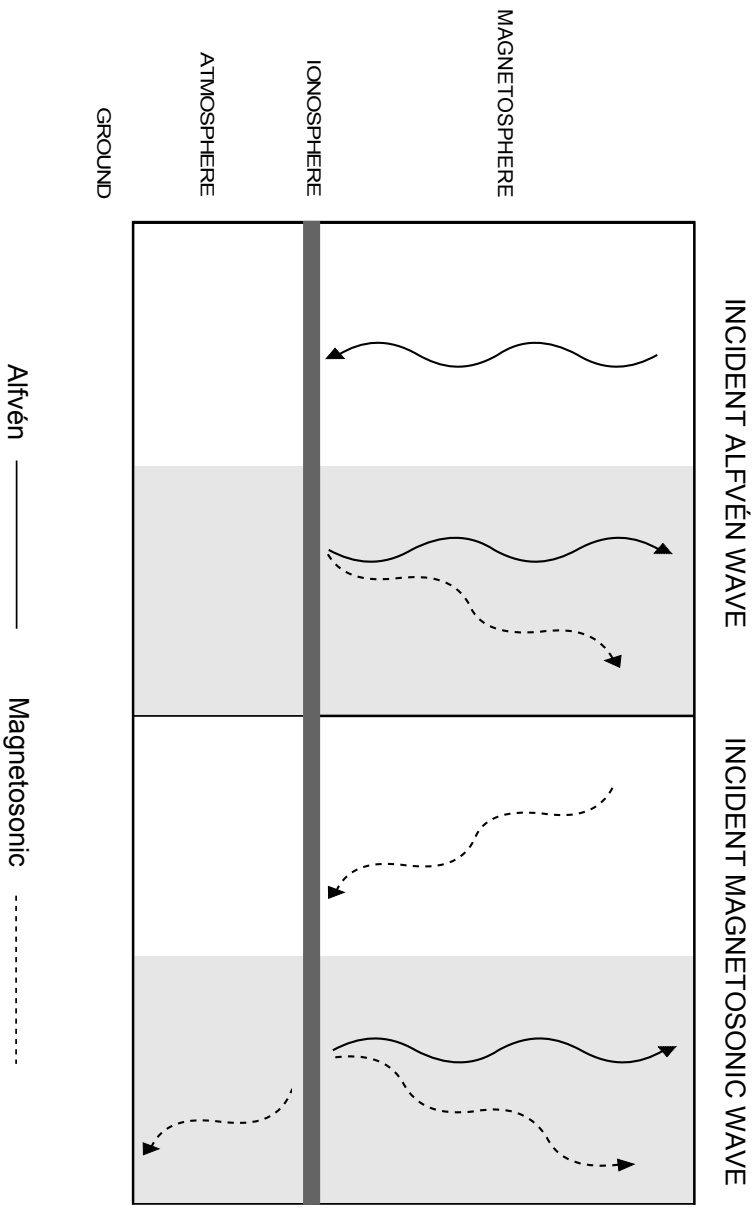

Figure 3.3: Schematic illustration of reflection and transmission of hydromagnetic waves at the ionosphere. The left two panels and right two panels show the effects of incident Alfvén and magnetosonic waves, respectively. Notice that only incident magnetosonic waves (right half) produce signatures below the ionosphere, as per Fukushima's theorem.

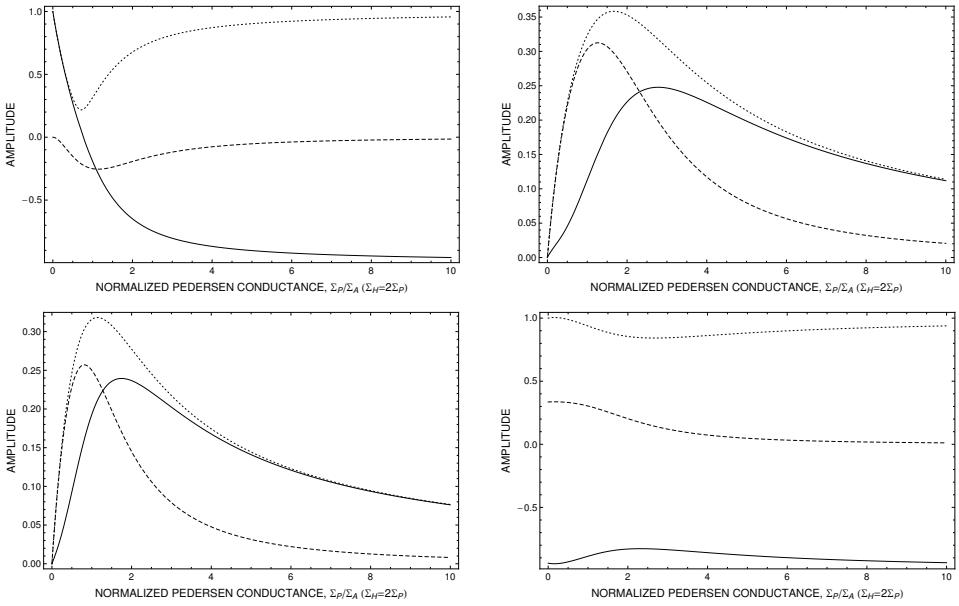

Figure 3.4: Dependence of Reflection Matrix Components on Pedersen Conductance. Clockwise from top left: R_{xx}, R_{yx}, R_{yy}, R_{xy}.

$$E_x = E_x^i \left(e^{-ik_z z} + Re^{ik_z z} \right) \tag{3.29}$$

The associated magnetic field from Faraday's Law (2.3) is

$$B_y = -\frac{E_x^i}{V_A} \left(e^{-ik_z z} - Re^{ik_z z} \right) \tag{3.30}$$

Note that we have used the Alfvén wave dispersion relation to replace k_z/ω by $1/V_A$.

It can be shown that the amplitude of the ratio B_y/E_x is given by

$$\frac{B_y}{E_x} = \frac{1}{V_A} \frac{1 + R^2 - 2R\cos(k_z z)}{1 + R^2 + 2R\cos(k_z z)} \tag{3.31}$$

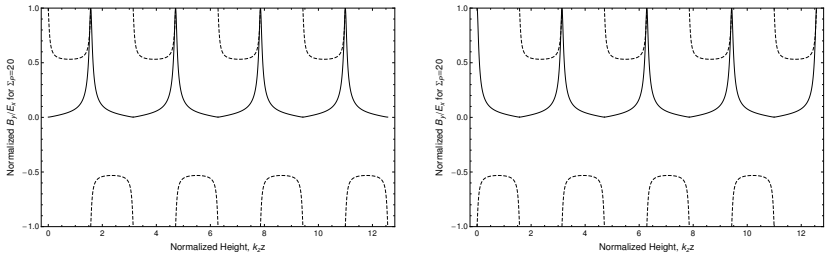

Figure 3.5: Normalized Ratio of Alfvén wave magnetic and electric fields. Solid line is amplitude, dotted line is phase. Left: $\Sigma_P/\Sigma_A = 20$. Right: $\Sigma_P/\Sigma_A = 1/20$. Horizontal axis is the vertical height normalized by the vertical wavenumber.

We can see from this expression that the field ratio has a nodal structure which depends on the sign of the reflection coefficient. In the large conductance limit ($\tilde{\Sigma}_P \ll 1$), maxima (which formally approach infinity) are found where $k_z z = n\pi$ and minima are found at $k_z z = \pi(n + 1/2)$. In the opposite limit, $\tilde{\Sigma}_P \gg 1$, the locations of maxima and minima are switched.

Just as the ionospheric currents create visible signatures on the ground, they also create additional signatures in the space above the ionosphere. For instance, a purely Alfvénic signal characterized by an electric field $\mathbf{E} = E_x \hat{e}_x$ will result in a compression wave with associated electric field $\mathbf{E}_c = R_{xy} E_x \hat{e}_y$. Using the values from Figure 3.4, we see that - depending on ionospheric conditions - an appreciable fraction of the incident wave energy may be converted to the compressional mode. Moreover, Figure 3.5 demonstrates that the observed vertical structure of a wave in the vicinity of the ionosphere depends strongly on the ionospheric conductance (or equivalently, reflection coefficient). For example, in situ observations near $z = 1/k_z$ would yield very different measurements depending on whether the boundary was a good conductor (large conductance limit) or a poor conductor (small conductance limit); intermediate values of conductance would naturally result in some manner of intermediate profile.

A very similar quantity to the field ratios shown in Figure 3.5 is the wave impedance, defined as the ratio of the transverse electric field to the complementary transverse magnetic field,

$$Z = \mu_0 \frac{E_{\perp,1}}{B_{\perp,2}} \tag{3.32}$$

For an Alfvén wave in a uniform (or slowly varying) plasma, the wave impedance of a propagating wave is the inverse of the Alfén conductance, while the impedance of a standing Alfvén wave is the inverse of the ionospheric conductance. Because of this, the wave impedance provides an obvious indicator of whether a wave is resonant (standing) or transient (propagating). Measurements of the wave impedance have been used to classify electromagnetic perturbations observed by the AUREOL-3 satellite[100], where the presence of structure in the profile of the wave impedance was used to infer the presence of propagating Alfvén waves.[19] It has suggested that wave impedance can be used to for diagnosing the ionospheric conductance[15]. We will return to this idea in Chapter 4.

[19]The waves observed in Zhao[100] were most likely in the inertial limit. Recall from Chapter 2 that such waves would have a $k_\perp$ dependence, $Z = \Sigma_A^{-1}(1 - k_\perp^2 \delta_e^2)/\sqrt{1 + k_\perp^2 \delta_e^2}$. For very small transverse scales, $k_\perp \delta_e^2 \gg 1$, it follows that $Z \propto k_\perp$.

Chapter 4

The Alfvén Resonator and Waveguide

As discussed in Chapter 1, the magnetospheric plasma density profile varies rapidly within 1 R_E of the Earth's surface. This region includes the ionosphere, and at high latitudes includes at least some of the auroral acceleration region. The rapid decrease in plasma density in the topside ionosphere leads to the formation of a resonant cavity for Alfvén waves, while the the strong minimum in Alfvén speed near the F_2 peak defines a waveguide for obliquely propagating magnetosonic waves. The fundamental frequencies of the IAR are on the order of 1 Hz, with the characteristic frequencies of cavity modes always being lower than the corresponding frequencies for waveguide modes.

The existence of the IAR was first postulated by Polyakov[71] , although earlier work by Greifinger[28] had already outlined the problem without much investigation. Theoretical and numerical work by Lysak[43],[44] and Pokhotelov[70], [69] has analyzed the properties of the Alfvén resonator using a model similar to that of Greifinger[28], and

the associated IAR spectra have been thoroughly analyzed in context. However, to our knowledge, only Lysak[45] and Prikner[75],[76] have considered a realistic density profile, while only Lysak[45] has used a realistic magnetic field model. In this Chapter, we will introduce a model which builds on the generality of Lysak's method and extends their ability to precisely characterize eigenmodes of the Alfvén resonator.

Alfvén resonator waveguide modes have been studied using multipoint ground measurements by a number of authors, including Fraser[19], Duong and Fraser[16],[17], Altman and Fijalkow[4], Arnoldy et al.[10], and Posch et al.[72].

In situ observations of IAR cavity modes have been reported on by numerous authors including Grzesiak et al.[30] and Zhao et al.[100].

We will begin this chapter by examining the theoretical properties of Alfvén and magnetosonic waves in a simplified model of the IAR region. We will then introduce a numerical method for the solution of the coupled Maxwell equations which we will use to study the properties of magnetic pulsations in the IAR for a variety of different plasma conditions.

4.1 Theoretical Background

The plasma we consider in this chapter is characterized by a uniform magnetic field directed in the $\hat{e}_z$-direction, with an Alfvén speed[28] that exponentially increases from a low value in the ionosphere and asymptotes to a large value in the ionosphere,

$$V_A^2 = \frac{V_I^2}{\epsilon^2 + e^{-z/H}} \tag{4.1}$$

Here V_I is the ionospheric Alfvén speed, and $V_M = V_I/\epsilon$ is the asymptotic Alfvén speed in the magnetosphere. The depth of the ionospheric minimum is determined by ϵ, while the width of the the minimum is determined by the scale height H.

Having previously analyzed the characteristics of waves in a uniform plasma, we are in a good position to explore additional effects that arise from considering wave processes in a non-uniform plasma.

4.1.1 Aspects of Wave Behavior in an Inhomogeneous Plasma

Let us consider a plasma which is inhomogeneous in the $\hat{e}_z$ direction having density given by (4.1) and uniform in the transverse directions. By virtue of the uniformity of the plasma, the transverse wave vector is a constant. However, the parallel wave vector varies spatially dependent upon the local value of the Alfvén speed. One model of this variation is provided by the WKB assumption, which presumes that the dispersion relationship of the wave is satisfied locally. Using (2.32) and (2.35), we can show

$$k_z = \frac{\omega}{c_A} \qquad k_z = \sqrt{\frac{\omega^2}{c_A^2} - k_x^2} \tag{4.2}$$

If an Alfvén wave with frequency ω and wave vector $\mathbf{k} = (k_x, 0, k_z)$ couples to a magnetosonic wave, (4.2) shows that it is possible for the resultant wave to have a zero or even imaginary parallel wave vector.

The majority of ULF waves observed propagating into the near-Earth region are Alfvénic, because these waves propagate largely unaffected along the magnetic field according to (2.32). Magnetosonic waves, on the other hand, are subject to refraction, reflection,

and attenuation arising from the inhomogeneity of the magnetospheric plasma.[1] A good example of this was provided by Lessard et al. [41], who observed an earthward propagating magnetosonic wave at geosynchronous orbit and an Alfvén wave with similar characteristics in the auroral zone with FAST.

Because of the strongly inhomogeneous plasma density within 1 R_E of the Earth, strongly localized Alfvén and magnetosonic wave modes are essentially decoupled. The notable exception to this decoupling is the generation of magnetosonic waves by ionospheric currents (both Hughes Rotation and Imperfect ASE). Note, however, that the sorts of waves that are permissible in this region are limited by, in essence, the dispersion relationship (2.35). Specifically, we will show that if the perpendicular wave number exceeds the asymptotic parallel wave number, the magnetosonic wave is confined to a limited spatial region, which we term the magnetosonic waveguide.

As an illustration, consider an incident Alfvén wave with $\omega - k_{z,I}V_I = 0$ incident at an angle θ at the ionosphere. If ionospheric Hall currents produce a magnetosonic wave with the same values of ω, k_x, we expect the wave to have a turning point at a height $z_{\rm t}$ above the ionosphere given by

$$z_{\rm t} = \frac{H}{\tan^2\theta - \epsilon^2} \tag{4.3}$$

Thus, any wave with $\tan\theta > \epsilon$ has a turning point at finite distance; when $\theta \sim 45^o$, the turning point and the scale height are comparable. We will typically consider waves for which $\epsilon \ll \tan\theta < 45^o$, corresponding to waves with turning points in the IAR region.[2]

[1] The extended WKB theory for magnetosonic waves is not overly complicated but it is beyond the scope of this thesis. In a 3d-inhomogeneous plasma, the wave is constantly diverted in such a way so as to satisfy the principle of least action. If the wave is initially earthward directed, it will be diverted in a manner similar to that of a Coulomb collision.

[2] Properly speaking the WKB approximation used to obtain (4.3) breaks down in the region where

4.1.2 The Magnetospheric Solution

Derivation of the Wave Equations

Although the plasma under consideration varies in the $\hat{e}_z$-direction, it is uniform in the perpendicular direction. Consequently, we can Fourier-transform Ampere's law in the transverse directions and time, and obtaining

$$E_x = -i\frac{V_A^2}{\omega}\frac{\partial B_y}{\partial z} \tag{4.4}$$

$$E_y = \frac{V_A^2}{\omega}(k_x B_z + i\frac{\partial B_x}{\partial z}) \tag{4.5}$$

And likewise Faraday's law,

$$B_x = -\frac{i}{\omega}\frac{\partial E_y}{\partial z} \tag{4.6}$$

$$B_y = \frac{i}{\omega}\frac{\partial E_x}{\partial z} \tag{4.7}$$

$$B_z = \frac{k_x}{\omega}E_y \tag{4.8}$$

As in the uniform plasma case, these equations can be separated for Alfvén and magnetosonic waves. However, instead of obtaining dispersion relationships, we now find wave

$k_z \approx 0$, but a full-wave solution should yield a qualitatively similar result.

equations. Equations (4.4) - (4.8) may be combined in order to find two second-order equations for the Alfvénic and magnetosonic electric fields (E_x and E_y, respectively),

$$\frac{\partial^2 E_x}{\partial z^2} + \frac{\omega^2}{V_I^2}\left(\epsilon^2 + e^{-z/H}\right) E_x = 0 \tag{4.9}$$

$$\frac{\partial^2 E_y}{\partial z^2} + \left(\frac{\omega^2}{V_I^2}\left(\epsilon^2 + e^{-z/H}\right) - k_x^2\right) E_y = 0 \tag{4.10}$$

Where e have explicitly inserted the Alfvén speed profile given by (4.1) in place of V_A^2. If V_A were constant, then the solution would obviously be a plane wave. However, with a non-uniform density profile, this is not the case. The solution, which is somewhat more complicated, will be discussed below.

4.1.3 Analytical Solution of the IAR Equations

In this section, we will demonstrate the existence of eigenfunction solutions of (4.9) and (4.10) as well as derive "dispersion relations" from which the eigenvalues can be obtained. We will then obtain analytical expressions for certain limits using perturbation expansions of the dispersion relations. Solutions of this type were first obtained by Greifinger[28] and have been used by various authors (e.g. Lysak[43], Demekhov[15], Lysak and Yoshikawa[50]) since.

Let us introduce $\zeta = \zeta_0 e^{-z/2H}$, $\zeta_0 = \dfrac{2H\omega}{V_I}$, $\nu = i\epsilon\zeta_0$, and $\mu = \sigma\sqrt{(2k_xH)^2 - (\epsilon\zeta_0)^2}$ where $\sigma = \text{sign}(2k_xH - \epsilon\zeta_0)$. Equations (4.9) and (4.10) may be written as

$$\frac{\partial^2 E_x}{\partial \zeta^2} + \frac{1}{\zeta}\frac{\partial E_x}{\partial \zeta} + \left(1 - \frac{\nu^2}{\zeta^2}\right) E_x = 0 \tag{4.11}$$

$$\frac{\partial^2 E_y}{\partial \zeta^2} + \frac{1}{\zeta}\frac{\partial E_y}{\partial \zeta} + \left(1 - \frac{\mu^2}{\zeta^2}\right) E_y = 0 \tag{4.12}$$

Both (4.11) and (4.12) are forms of Bessel's differential equation, so we can write their solutions as

$$E_x = a_+ J_\nu(\zeta) + a_- J_{-\nu}(\zeta) \tag{4.13}$$

$$E_y = b_+ J_\mu(\zeta) + b_- J_{-\mu}(\zeta) \tag{4.14}$$

Note that we want to consider only waves for which energy is not being supplied from the outer magnetosphere. This requires that we have either a wave propagating in the $-\hat{e}_z$ direction or that the wave decay exponentially with increasing z. (The evanescent equivalent of an outgoing wave.)

Note that as $z \to \infty$, $\zeta \to 0$. The leading term in the Taylor series for $J_{\nu,\mu}(\zeta)$ is

$$J_{\nu,\mu} \approx \frac{1}{\Gamma(1+\nu,\mu)} \left(\frac{\zeta}{2}\right)^{\nu,\mu} \tag{4.15}$$

Or, inserting the explicit form of ζ, we have

$$J_{\nu,\mu} \approx \frac{1}{\Gamma(1+\nu,\mu)} \left(\frac{\zeta_0}{2}\right)^{\nu,\mu} e^{\frac{-z\nu,\mu}{H}} \tag{4.16}$$

Since we are considering a Southern-Hemisphere situation in which $\hat{e}_n = -\hat{e}_z$, we find that an outward propagating wave is given by $J_{-\nu}$ and an evanescent wave is given by J_μ, since σ accounts for the necessary change of sign across $2k_xH = \epsilon\zeta_0$. Thus, for a purely outgoing wave, we set $a_+ = b_{-\sigma} = 0$.

In order to determine the allowed frequencies and damping rates, we must specify ionospheric boundary conditions.

4.1.4 Ionospheric Boundary Conditions

The Ionosphere jump conditions were discussed in Chapter 3. These boundary conditions relate the change in the transverse magnetic fields across the ionospheric layer to the currents driven by the associated electric fields. The general form of the jump conditions are (from (3.4))

$$\mu_0 \Sigma \cdot \mathbf{E} = \hat{e}_n \times \Delta\mathbf{B} \tag{4.17}$$

Here, as before, Δ indicate the difference in a quantity above and below the ionosphere, which is assumed to have a thickness d such that $k_\perp d << 1$ and $\omega d << V_A$. Using the Maxwell equations (4.6) and (4.7), we can write (4.17) as

$$\mu_0 \begin{pmatrix} \Sigma_P & -\Sigma_H \\ \Sigma_H & \Sigma_P \end{pmatrix} \cdot \begin{pmatrix} E_x \\ E_y \end{pmatrix} = - \begin{pmatrix} \frac{i}{\omega}\frac{\partial E_x}{\partial z} + B_x^{ATM} \\ \\ \frac{i}{\omega}\frac{\partial E_y}{\partial z} + B_y^{ATM} \end{pmatrix} \tag{4.18}$$

The superscript ^{ATM} here indicates the value below the ionosphere (i.e. in the atmosphere). These fields are obtained using the magnetic potential method of Chapter 3.[3] As shown previously, the magnetic field in the atmosphere can be expressed in terms of a scalar potential, $\mathbf{B}^{ATM} = \nabla\Psi$, where the scalar potential is given by

$$\Psi = \frac{\sinh(k_x z)}{\omega \cosh(k_x h)} E_y \tag{4.19}$$

Since the potential has no dependence on y, $B_y^{ATM} = 0$. The $x-$component of the magnetic field is given by

$$B_x^{ATM} = \frac{ik_x}{\omega \tanh(k_x h)} E_y \tag{4.20}$$

4.1.5 Dispersion Relation

We can combine expressions (4.20) and (4.18) to obtain a relationship between the transverse electric fields and their derivatives,

$$\mu_0 \begin{pmatrix} \Sigma_P & -\Sigma_H \\ \Sigma_H & \dfrac{ik_x}{\mu_0 \omega \tanh k_x h} + \Sigma_P \end{pmatrix} \cdot \begin{pmatrix} E_x \\ E_y \end{pmatrix} = -\frac{i}{\omega}\frac{\partial}{\partial z} \begin{pmatrix} E_x \\ E_y \end{pmatrix} \tag{4.21}$$

Inserting the Bessel function solutions for E_x and E_y that we previously obtained and transforming from z to ζ, we find

[3] For a more realistic spherical ionosphere, the method of Appendix B would be used.

$$\begin{pmatrix} \dfrac{\Sigma_P}{\Sigma_A} & -\dfrac{\Sigma_H}{\Sigma_A} \\ \dfrac{\Sigma_H}{\Sigma_A} & \alpha + \dfrac{\Sigma_P}{\Sigma_A} \end{pmatrix} \cdot \left. \begin{pmatrix} J_{-\nu} \\ \rho J_{\sigma\mu} \end{pmatrix} \right|_{\zeta=\zeta_0} = -i \frac{\partial}{\partial \zeta} \left. \begin{pmatrix} J_{-\nu} \\ \rho J_{\sigma\mu} \end{pmatrix} \right|_{\zeta=\zeta_0} \tag{4.22}$$

Where $\alpha = 2ik_xH/\zeta_0 \tanh k_x h$ and $\rho = b/a$ is the ratio of the electric field amplitudes. Note that there are two unknown quantities in this equation, the frequency (contained in ζ_0, ν, μ) and the amplitude ratio. Because this two-equation system in linear in ρ, we can solve one of the equations for the amplitude ratio, finding

$$\rho = -\frac{\tilde{\Sigma}_H J_{-\nu}}{(\alpha + \tilde{\Sigma}_P) J_{\sigma\mu} + i J'_{\sigma\mu}} \tag{4.23}$$

(Where $\tilde{\Sigma}_{P,H} = \Sigma_{P,H}/\Sigma_A$ and a prime $'$ indicates differentiation, and all Bessel functions in have the argument ζ_0.)

The second equation of the linear system described above defines a coupled nonlinear dispersion relationship for hydromagnetic waves in the Alfvén resonator region,

$$\left(\tilde{\Sigma}_P J_{-\nu} + i J'_{-\nu}\right) \left((\alpha + \tilde{\Sigma}_P) J_{\sigma\mu} + i J'_{\sigma\mu}\right) = \tilde{\Sigma}_H^2 J_{-\nu} J_{\sigma\mu} \tag{4.24}$$

Notice that in the limit of $\tilde{\Sigma}_H \to 0$, (4.24) is satisfied by either of the parenthetical quantities vanishing. Recall from earlier that $J_{-\nu}$ relates to E_x perturbations, while $J_{\sigma\mu}$ corresponds to E_y perturbations; thus, in the absence of Hall conductance, the coupling between the waves disappears (as it should). Except in very special cases, it is unusual to find $\rho \sim 1$. Rather, numerical solutions of the fully coupled dispersion relation typically find either $\rho^2 \ll 1$ or $\rho^2 \gg 1$, corresponding to almost purely resonator-like

or waveguide-like modes.[4] Thus, while we acknowledge that normal modes of the IAR dispersion relation generally involves both cavity and waveguide components, we will limit our considerations in this chapter to the case of zero Hall conductance.

4.1.6 Cavity Modes of the Ionospheric Alfvén Resonator

The Alfvén resonator was predicted theoretically long before its existence was substantiated by observation. Initially discussed by Polyakav[71] and subsequently by many others such as Lysak[43],[44], the existence of a resonant cavity in the ionosphere provides a natural explanation for certain observed features of both Pc1 and Pi1 magnetic pulsations.

4.1.7 Analytic Solution for the Alfvén Resonator

The dispersion relationships governing the IAR cavity and waveguide modes, (4.24) are a complicated nonlinear function of the complex frequency, even in the absence of Hall effects. As a consequence, the existence of any solutions, much less an infinite number, is not immediately obvious.

The Deep Resonator Approximation

Cavity modes of the IAR are defined by the left parentheses of (4.24),

$$\tilde{\Sigma}_P J_{-\nu} + i J'_{-\nu} = 0 \tag{4.25}$$

[4]The particular coupled modes have been somewhat discussed by Pokhotelov[69], although the author's emphasis there is on the modification of the ionospheric feedback instability rather than the normal mode structure.

A well-defined Alfvén resonator requires $\epsilon \ll 1$ (i.e. the Alfvén speed minimum is a deep one). Assuming a well-defined resonator allows us to use ν (which is proportional to ϵ) as the small parameter in a perturbation expansion of the Bessel functions of (4.25). Using a rather convenient formula from Abramowicz and Stegun[1],

$$\left.\frac{\partial J_l}{\partial l}\right|_{l=0} = J_0 + \frac{l\pi}{2} Y_0 \tag{4.26}$$

We have

$$\tilde{\Sigma}_P \left(J_0 - \frac{\nu\pi}{2} Y_0 \right) - i \left(J_1 - \frac{\nu\pi}{2} Y_1 \right) = 0 \tag{4.27}$$

Note that we have used the well-known recurrence relations $J_0^{'} = -J_1$ and $Y_0^{'} = -Y_1$ in obtaining the above expression.

4.1.8 The Weak Damping Approximation

We expect the cavity modes to be damped (due to ionospheric dissipation and leakage), but observations indicate that this damping is not very strong. Therefore we suppose that the imaginary part of ζ_0 is much smaller than its real part, $\zeta_I \sim \epsilon$. Taylor expanding the Bessel functions of (4.27) around the real part of its argument ($\zeta_0 \approx \zeta_R$), we have to first order in ϵ

n	1	2	3	4	5
$\zeta_{R,n}$	3.83171	7.01559	10.17347	13.32369	16.47063

Table 4.1: Zeros of the J_1 Bessel Function

$$\begin{aligned}&\tilde{\Sigma}_P\left(J_0(\zeta_R) - i\zeta_I J_1(\zeta_R) - i\frac{\epsilon\zeta_R\pi}{2}Y_0(\zeta_R)\right)\\ =&i\left(J_1(\zeta_R) + i\zeta_I J_1'(\zeta_R) - i\frac{\epsilon\zeta_R\pi}{2}Y_1(\zeta_R)\right)\end{aligned} \tag{4.28}$$

Low Conductance Limit, $\tilde{\Sigma}_P \ll 1$

For small conductance, we assume $\tilde{\Sigma}_P \sim \epsilon$. Retaining terms of only $\mathcal{O}(\epsilon)$ or larger in (4.28), we find

$$iJ_1(\zeta_R) = \tilde{\Sigma}_P J_0(\zeta_R) + \zeta_I J_1'(\zeta_R) - \frac{\epsilon\zeta_R\pi}{2}Y_1(\zeta_R) \tag{4.29}$$

Note that the RHS of (4.29) involves only terms of $\mathcal{O}(\epsilon)$. The zeroth order solution is therefore given by $J_1(\zeta_R) = 0$, requiring ζ_R to be a zero of the J_1 Bessel function. The first five zeros of J_1 are given in Table 4.1.

With ζ_R being a zero of J_1 and noting that $J_1'(\zeta_R) = J_0(\zeta_R) - J_1(\zeta_R)/\zeta_R$, we can solve (4.29) for the imaginary component ζ_I

$$\zeta_I = -\left(\tilde{\Sigma}_P - \frac{\epsilon\zeta_R\pi}{2}\frac{Y_1(\zeta_R)}{J_0(\zeta_R)}\right) \tag{4.30}$$

The Wronskian relation for the Bessel J_0 and Y_0 functions is

n	1	2	3	4	5
γ_n/ω_n	-0.01870	-0.01725	-0.01675	-0.01649	-0.01634

Table 4.2: Relative Damping Increment γ/ω for $\tilde{\Sigma}_P = \epsilon$

$$J_0(\zeta)Y_1(\zeta) - J_1(\zeta)Y_0(\zeta) = -\frac{2}{\pi\zeta} \tag{4.31}$$

Since $\zeta_R > 0$ and $J_1(\zeta_R) = 0$, (4.31) tells us that J_0 and Y_1 have opposite signs and ζ_I is guaranteed to be negative.

Note that the ratio of ζ_I to ζ_R is the same as the ratio of γ to ω. For example, if we take $\tilde{\Sigma} = \epsilon$, then the ratio γ/ω calculated from (4.30) has the values given in 4.2.

In this case, the conductance contribution is about 15% of the total damping, so the majority of the loss is actually due to leakage into the magnetosphere.

High Conductance Limit, $\tilde{\Sigma}_P \ll 1$

For high conductance, we assume $1/\tilde{\Sigma}_P \sim \epsilon$. As before, we retain only terms of $\mathcal{O}(\epsilon)$ or larger in (4.28), finding

$$J_0(\zeta_R) = i\left(\frac{J_1(\zeta_R)}{\tilde{\Sigma}_P} + \zeta_I J_1(\zeta_R) + \frac{\epsilon\zeta_R\pi}{2}Y_0(\zeta_R)\right) \tag{4.32}$$

The zeroth order solution of (4.32) gives us $J_0(\zeta_R) = 0$, meaning that ζ_R is a zero of the J_0 Bessel function. The first five of these zeros are given in Table 4.3.

With $J_0(\zeta_R) = 0$, we can solve for the imaginary component ζ_I from (4.32)

n	1	2	3	4	5
$\zeta_{R,n}$	2.40483	5.52009	8.65373	11.79154	14.93092

Table 4.3: Zeros of the J_0 Bessel Function

n	1	2	3	4	5
γ_n/ω_n	-0.01959	-0.01746	-0.01684	-0.01654	-0.01637

Table 4.4: Relative Damping Increment γ/ω for $1/\tilde{\Sigma}_P = \epsilon$

$$\zeta_I = -\left(\frac{1}{\tilde{\Sigma}_P} + \frac{\epsilon\zeta_R\pi}{2}\frac{Y_0(\zeta_R)}{J_1(\zeta_R)}\right) \tag{4.33}$$

From (4.31), we can see that Y_0 and J_1 always have the same sign, guaranteeing that ζ_I is always negative.

For the case $1/\tilde{\Sigma}_P = \epsilon$, we can use (4.33) to determine the relative damping rate γ/ω for the high conductance case; the results are given in Table 4.4.

4.2 IAR Numerical Solution

When neither the large or small conductance approximations are appropriate, we must resort to solving (4.25) using numerical techniques. Specifically, we make use of the complex Newton's method[5] to find a value of ζ_0 such that (4.25) is satisfied to some pre-determined level of accuracy.[6] Although we don't have an expression for the exact solution, we do known that its real part will be somewhere between the roots of $J_0(\zeta_0)$ and $J_1(\zeta_0)$, which are known. Moreover, we expect that the complex part of the frequency will be negative, since there is no physical mechanism of instability (and our

[5]Cite Press/NR here.
[6]Seven decimal points, in practice

results at both limits were negative). Finally, we should expect damping to be at its greatest when the Alfvén conductance is in the neighborhood of the Pedersen conductance, since the homogeneous plasma reflection coefficient vanishes for $\Sigma_P = \Sigma_A$ (i.e. the wave is totally absorbed). This allows us to efficiently locate the roots of (4.25) and complete our picture of the cavity mode dispersion characteristics.

4.2.1 Numerical Dispersion Relationships

For a well-defined resonator and an ionosphere, the n^{th} harmonic of the IAR cavity mode has a normalized frequency bounded is effectively bounded by the roots of the n^{th} Bessel function and its derivative,

$$\text{RootOf}[J_n(\zeta)] \leq \zeta \leq \text{RootOf}[J_n'(\zeta)] \tag{4.34}$$

This is demonstrated in Figure 4.1. Notice that the transition between the limiting values occurs quite rapidly, near $\tilde{\Sigma}_P = 1$. For $\tilde{\Sigma}_P$ just a few times greater than 1, the frequency effectively obtains its limiting value. Thus, although we have previously considered $\tilde{\Sigma}_P \sim \epsilon^{-1}$ to be large, for the purposes of determining IAR cavity frequencies, $\tilde{\Sigma}_P = 5$ is effectively infinity.

Unlike the oscillation frequency, the damping rate of the IAR cavity mode is very sensitive to $\tilde{\Sigma}_P$. Comparing Figures 4.1 and 4.2, we see that the damping rate maximizes where the frequency is changing fastest, near $\tilde{\Sigma}_P = 1$. This is expected, since this value corresponds to a perfectly absorbed wave in the electrostatic limit (cf. Chapter 3).

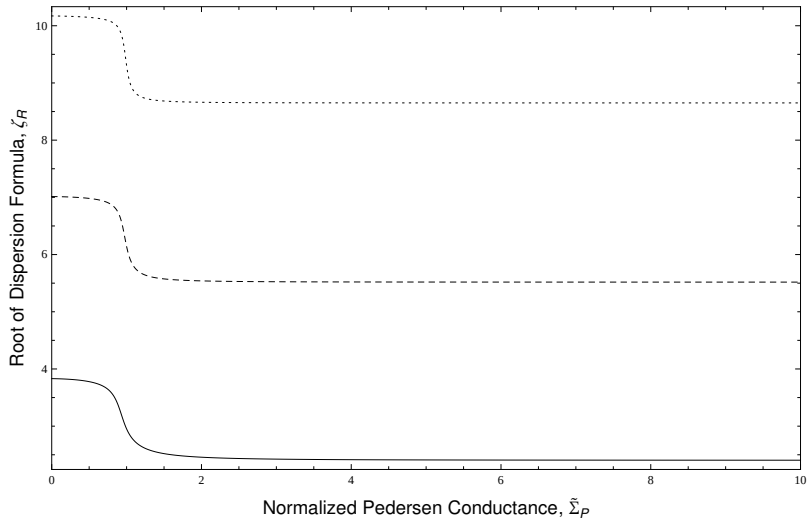

Figure 4.1: Dispersion Relation for Alfvén Resonator Modes n=0-2, $\epsilon = 0.01$

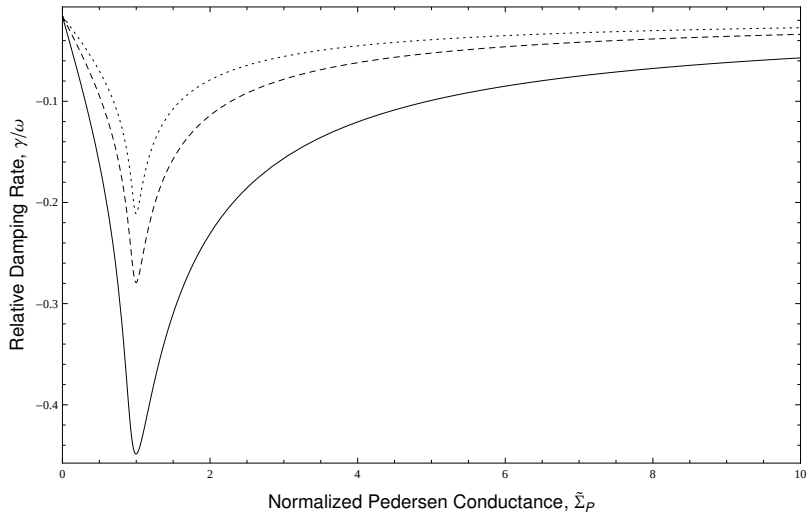

Figure 4.2: Damping Rate for Alfvén Resonator Modes n=0-2, $\epsilon = 0.01$

4.3 Waveguide Modes of the Ionospheric Alfvén Resonator

4.3.1 Observations

Greifinger[28] studied the problem of magnetosonic wave propagation in the ionosphere in order to explain the apparent worldwide propagation of signals generated by the Argus nuclear tests. These tests consisted of three nuclear warhead detonations between 200 and 600 km. Following the Argus 3 detonation at 539 km, a signal was observed on the ground propagating at 700 km/s away from the detonation epicenter. Given the proximity of the detonation to the ionospheric density peak and the correspondence between the propagation speed of the signal and the local Alfvén speed, it was hypothesized that the signal was a ducted magnetosonic wave.

Subsequent nuclear tests, including the 1962 Starfish Prime explosion provided additional evidence for the propagation of magnetosonic waves in the ionosphere around 400 km. The Starfish test was extensively instrumented [7] with both ground-based and airborne radar. Observations indicated that a dispersive wave with direction-dependent velocity propagated away from the epicenter. Although this was cited as being problematic in the analysis of Starfish data[42], it is consistent with the theory of off-meridian propagation as outlined by Greifinger[29].

Fraser[19] presented data from ground based magnetometers showing the westward propagation of a signal with velocities between 500 and 2500 km/s. Rather than being associated with a high-energy impulse as were the Argus events, Fraser's were caused by a naturally occurring plasma instability (the EMIC instability, discussed previously in Chapter 3).

[7] Argus was, by comparison, "poorly instrumented"[42]

Many authors have noted that the existence of a transverse duct in the IAR complicates the interpretation of ULF wave signals on the ground. If multiple observations are available, it is possible to use direction-of-arrival analysis[62],[20] to locate the actual injection center, i.e. the ground footprint of the magnetic field line along which the signal was initially incident.

4.3.2 Dispersion Relation

In the absence of coupling by Hall effects, waveguide modes are defined by the right parentheses of (4.24),

$$(\alpha + \tilde{\Sigma}_P)J_{\sigma\mu} + iJ'_{\sigma\mu} = 0 \tag{4.35}$$

Magnitude of the Atmospheric Correction

The characteristics of waveguide solutions depend not only the conductance, but also an atmospheric term, α of Equation (4.35). This atmospheric correction term depends on the parameters of both the Alfvén resonator and the atmosphere as well as the transverse structure of the wave itself.

$$\alpha = \frac{2iH}{h\zeta_0}\frac{k_x h}{\tanh(k_x h)} \tag{4.36}$$

We can expect that ζ_0 for the waveguide mode will have a magnitude comparable to that of the cavity mode. So, as an order of magnitude estimate, let us take $\zeta_0 \approx 3$ for $n = 0$. We expect the ionospheric scale height H to be at least a few times larger

than the atmospheric height, h, so we can reasonably expect $2H/h \geq \zeta_0$. Since we are primarily concerned with waves having larger transverse scales (non-inertial regime), it makes sense to suppose $k_x h \leq 1$, and so $1 \leq k_x h/\tanh(k_x h) \leq 1.3$. Thus, the atmospheric correction should always be greater than 1 for the fundamental mode, and quite possibly for a few of the higher harmonics as well, since the ratio H/h may be as large as 10. As noted by Lysak[50], the magnitude of the atmospheric term is negligible only in the infinite conductance limit, $\tilde{\Sigma}_P \to \infty$. For waveguide modes in the nightside IAR, the atmospheric effect is usually the dominant one.

Finally, note that the atmospheric correction is an imaginary one. As a consequence, the atmospheric term results in phase shift rather than attenuation - the effective conductivity of the Earth is taken to be infinite, and there is consequently no loss due to the wave in the atmosphere. The damping rate does depend on k_x, however, since the atmospheric correction does modify the phase of wave at the ionospheric boundary.[8]

4.4 Waveguide Normal Modes

For a given set of magnetosphere-ionosphere parameters, each value of k_x corresponds to a unique spectrum of allowable waveguide frequencies, or, equivalently, every given frequency corresponds to a unique spectrum of complex wavenumbers. This is perhaps the more preferred viewpoint for a waveguide mode, but owing to the close analogy between the waveguide and the IAR, we prefer to think of the frequency as a complex quantity.

[8]Specifically, for a given conductance, the absolute damping rate increases with k_x, while the relative damping rate decreases. Harmonics have higher absolute damping rates than the fundamental, but their relative damping rates are smaller.

4.4.1 Numerical Dispersion Relationships

The waveguide modes show less of dependence on the ionospheric conductance than the cavity modes and exhibit what is, essentially, the opposite behavior - an increase in frequency with increasing $\tilde{\Sigma}_P$. The frequency of the waveguide is basically a linear function of the perpendicular wavenumber, k_x. This isn't entirely surprising, since the WKB estimate gives us $\omega \approx k_x V_A \sqrt{1 + k_z^2/k_x^2}$. For $k_x \gtrsim k_z$, this implies an essentially linear relationship between the frequency and the perpendicular wavenumber. It can be seen in Figure 4.3(a) the only real breakdown of this linear relationship occurs for $k_x R_E \ll 1$, corresponding to asymptotically untrapped modes.[9].

Unlike the characteristic frequencies, the damping rates of the IAR waveguide mode are qualitatively similar to those of the cavity mode, although the steep maximum near $\tilde{\Sigma}_P = 1$ no longer exists. Instead, we find that the damping maximizes for some value $\tilde{\Sigma}_P > 1$ that is inversely related to $k_x H$. We can interpret this as resulting from the k_x-dependent atmospheric correction producing an effective increase in the ionospheric conductivity.

The transition between trapped and untrapped mode is rather obvious in the damping rate, as shown in Figure 4.3(b). Untrapped waveguide modes are very similar to cavity mode oscillations, as they are damped not only by ionospheric losses but also leakage to the magnetosphere.

[9] In the case of Figure 4.3, the transition between trapped and untrapped occurs at about $k = 0.15\ R_E^{-1}$

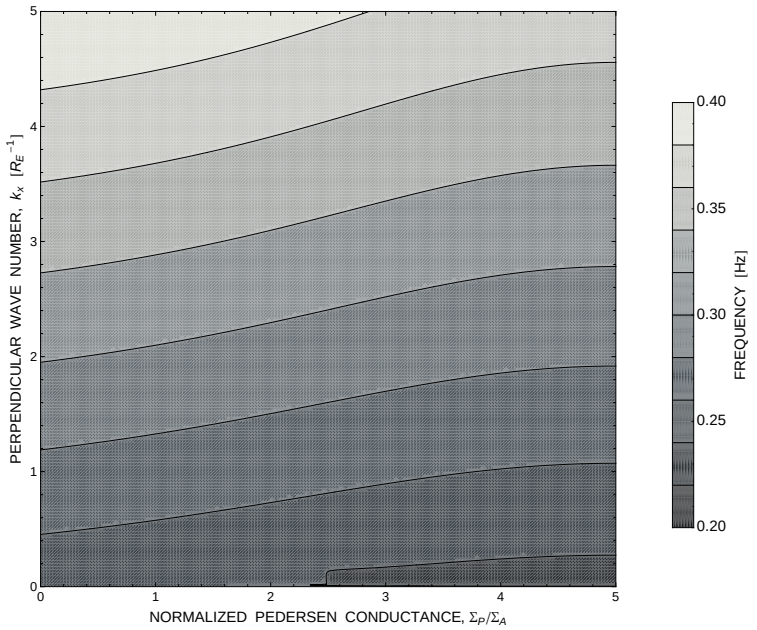

(a) Waveguide Mode Frequency

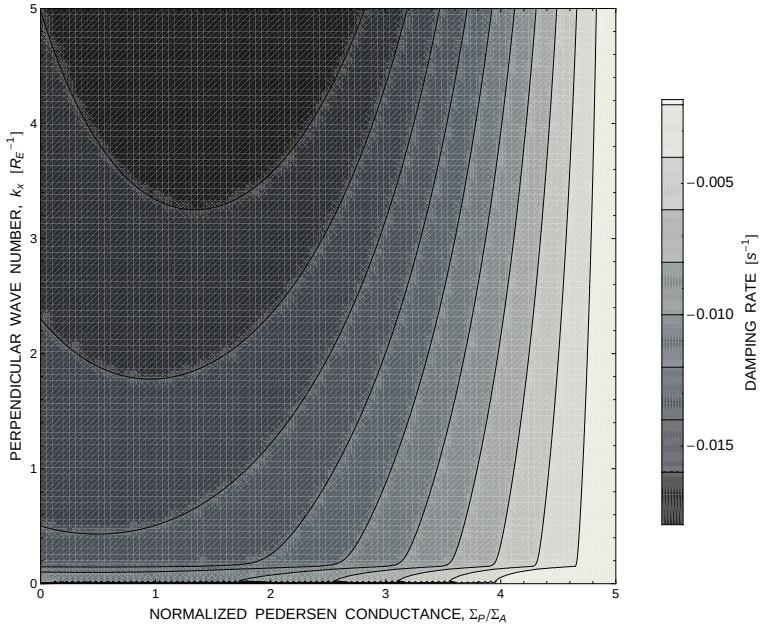

(b) Waveguide Mode Damping Rate

Figure 4.3: Characteristics of fundamental waveguide mode, $\epsilon = 1/100$, $H = 500$ km, $d = 100$ km, $V_I = 700$ km/s. (a) Frequency. (b) Damping rate.

4.4.2 Propagation Speed

The perpendicular propagation velocity of the eigenmode is related to the group velocity, which in terms of the eigenvalue ζ_0 is given by

$$V_g = \frac{V_I}{2H}\frac{\partial \zeta_0}{\partial k_\perp} \tag{4.37}$$

Since the frequency of a waveguide eigenmode is generally complex, the propagation wave is taken to be the real part of the group velocity, $V_\perp = \Re(V_g)$.

We see that the propagation speed is largest for small Pedersen conductances and large perpendicular wavelengths. This suggests that waves should propagate most quickly at lower latitudes on the night side. Even at higher conductances, the propagation speed is always above the minimum Alfvén speed, typically 1.4 - 1.5 times greater (although much larger for smaller $k_\perp$). The dependence of the wave speed on the perpendicular wavelength for small $k_\perp H$ and $\tilde{\Sigma}_P$ provides a reasonable explanation for the variation of signal propagation speeds observed by Fraser[19] and noted by Altman[4], amongst others.

The group velocity given by Equation (4.37) is not only possible definition for the propagation speed of a waveguide mode. Hayes[32] showed than the group velocity of a wave can be equivalently viewed as the speed of energy propagation. By considering the flux of wave energy in perpendicular direction to be due to the propagation of wave energy density at the perpendicular group velocity, it is possible to obtain an independent determination of the group velocity. In the Cartesian coordinates currently being considered, this method gives us

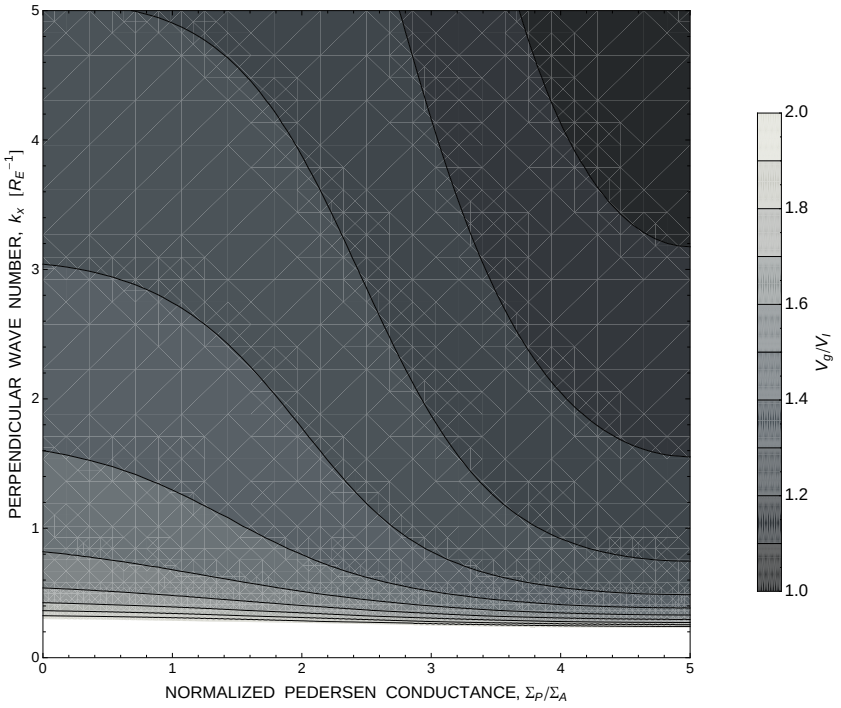

Figure 4.4: Perpendicular propagation speed of fundamental waveguide mode, $\epsilon = 0.01$, $H = 500$ km, $d = 100$ km, $V_I = 700$ km/s. Group speed increases rapidly near the trapped/untrapped limit of k_x, indicating that just barely trapped waves should propagate much more rapidly than strongly trapped waves. Only values corresponding to trapped modes are plotted.

$$v_g = 2\frac{E_y \tilde{B}_z}{E_y^2/V_A^2 + B_x^2 + B_z^2} \tag{4.38}$$

Unlike the derivative method, application of (4.38) does not produce a single value, but rather a vertical profile of group velocities. Given that they are both nominally accurate, it would be desirable to reconcile these two results, but their mutual relationship is not immediately obvious. Figure 4.4.2, shows an example of the group speeds determined from Equations (4.37) and (4.38). We see that the derivative method predicts higher propagation speed than direct energy considerations, if we assume that the energy is being propagated in regions where the Poynting flux is at a maximum.

One possible connection is the that the group velocity obtained from Equation (4.37) represents an average, in some sense, of the profile given by Equation (4.38). This would imply that the region of consideration extends to 3.4 scale heights (1700 km) for the fundamental mode (v_g = 887 km/s) and 4.75 scale heights (2375 km) for the first harmonic (v_g = 958 km/s). This height is not unreasonable, since more than 98% of the Poynting flux is located found below this height for both the fundamental and first harmonics.

In addition to the complications arising from multiple definitions of propagation speed, researchers have previously discussed the additional possibility of multiple ducts with different propagation speeds[42],[4]. It is conceivable that this is related not only to the structure of the ionosphere (i.e. a second duct), but also of the ducted wave. If this were the case, Figures 4.6 and 4.4.2 would imply that harmonics of long perpendicular wavelength would be able to propagate more rapidly than shorter wavelength fundamental modes, something not necessarily indicated by the derivative method, e.g. Figure 4.14. In this case, $k_\perp$ dependence of the waveguide frequency would allow for

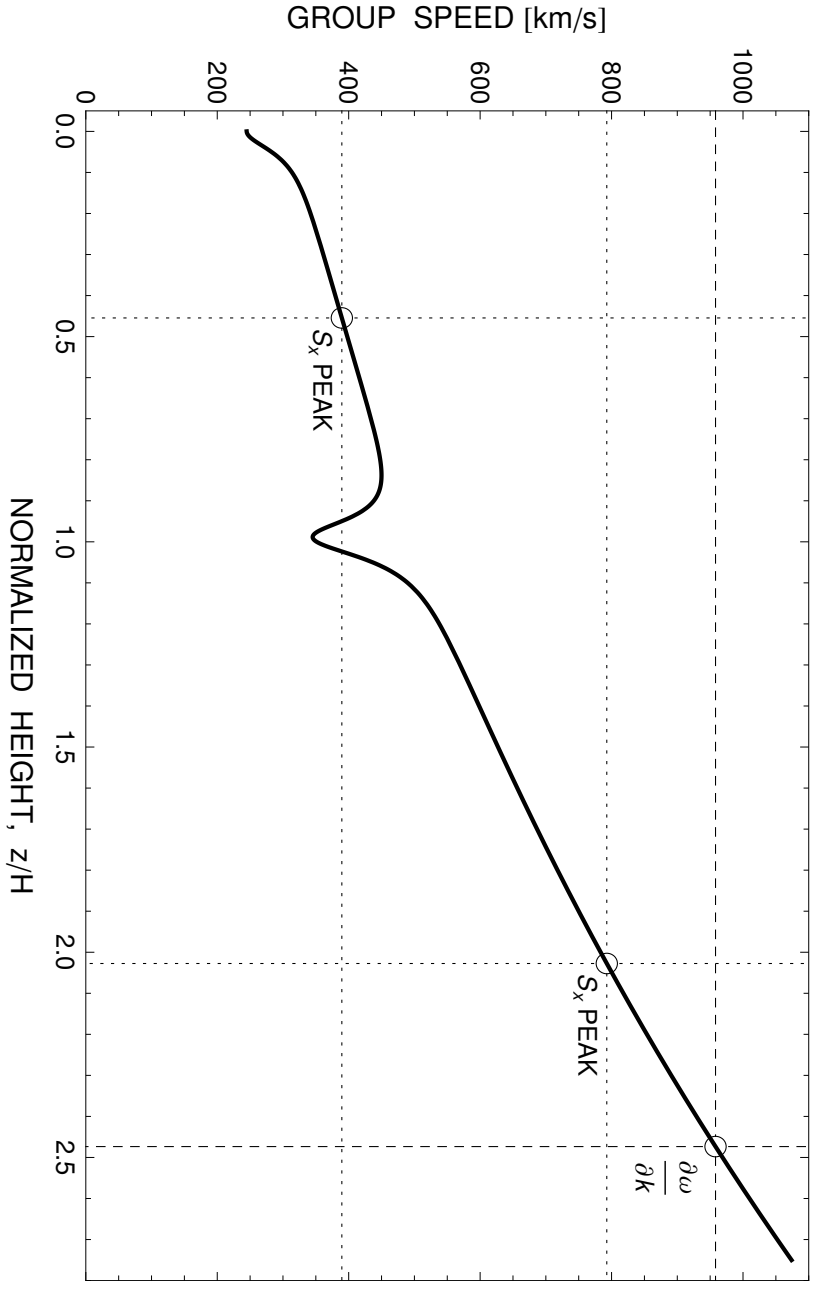

Figure 4.5: Profile of group velocity as determined from Equation 4.38 for a first harmonic IAR cavity mode in Greifinger's model. Here $V_I = 700$ km/s and $H = 500$ km. Dotted lines correspond to altitude of Poynting flux maxima and the dashed line corresponds to the group speed as determined from Equation 4.37.

two waves with similar frequencies but different perpendicular wavelengths to propagate at potentially very different speeds. This question cannot be answered by the present analysis, however, and we will return to it in Chapter 6.

4.4.3 Vertical Structure

As noted in the previous section, the propagation characteristics of the waveguide mode may exhibit vertical variation depending on the distribution of Poynting flux. Generally speaking, higher altitude corresponds to larger propagation speeds. By examining the vertical profile of waves as a function of model parameters, we find that the location of the waveguide peak depends primarily upon the perpendicular wave vector and the harmonic number. This is shown in Figure 4.6, where we see that the height of the mode peak is inversely related to the magnitude of the perpendicular wave vector and that higher harmonics have uppermost peaks at higher altitudes. Since we already know that (trapped) waves with smaller k_x travel faster, this would suggest that the waves also travel at higher altitudes. This is consistent with the previously mentioned idea that waves travel near the local Alfvén speed, since the Alfvén speed is an increasing function of altitude.

4.5 Generalization of the Model

The Alfvén speed profile given by (4.1) is useful in that it allows for the analytical solution of the waveguide equations, but it does not accurately represent the behavior of the Alfvén speed above its peak. Lysak[10] studied this problem by examining the structure of the reflection coefficient for Alfvén waves in an inhomogeneous plasma

[10]Cite Lysak, 1994

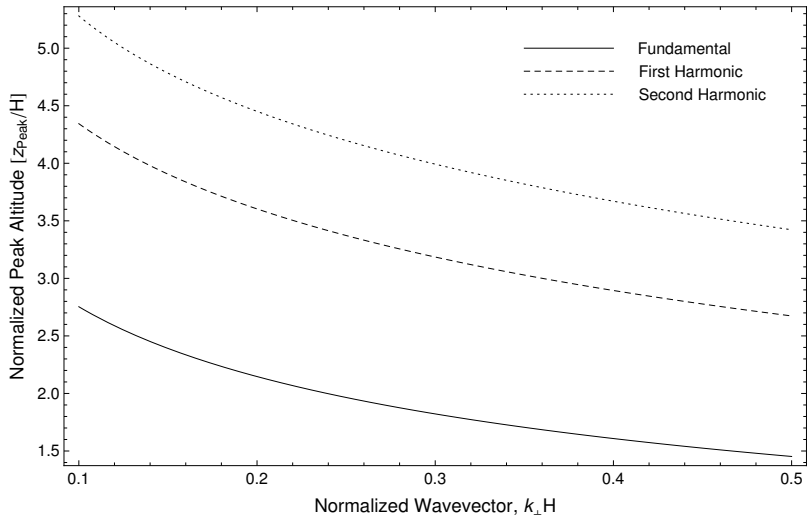

Figure 4.6: Height of upper waveguide mode peak, $\epsilon = 0.01$ and $\tilde{\Sigma}_P = 10$. If $h = 500$ km and $k = 2\ R_E^{-1}$, then the upper peaks occur at 1900 km, 2200 km, and 2400 km for the fundamental and first two harmonics, respectively.

using a method based on Elsässer variables. We will briefly discuss this method and relevant results, and then we will introduce an alternative method which addresses some apparent shortcomings of the reflection coefficient method.

Reflection Coefficient for the Greifinger Model

In Chapter 3 we discussed the reflection and transformation of plane waves for which sinusoidal variation could be assumed. This cannot be applied directly to Alfvén waves in the IAR. Instead, we must return to (4.18) and allow the wave to be a superposition of incoming and outgoing waves. Setting $\Sigma_H = \alpha = 0$ and letting $\mathbf{E} = (e^i J_\nu(\zeta) + e^r J_{-\nu}(\zeta))\hat{e}_x$, we find that the reflection coefficient $R_A = e^r/e^i$ is

$$R_A = -\frac{\tilde{\Sigma}_P J_\nu(\zeta_0) + i J'_\nu(\zeta_0)}{\tilde{\Sigma}_P J_{-\nu}(\zeta_0) + i J'_{-\nu}(\zeta_0)} \tag{4.39}$$

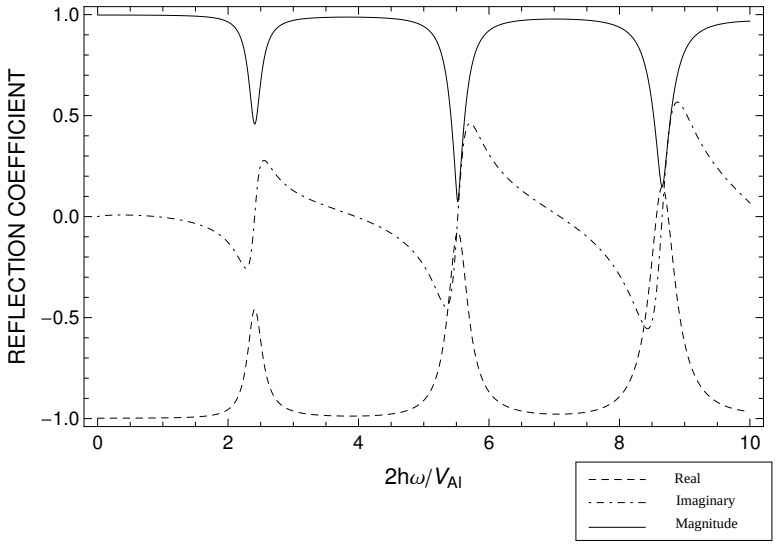

Figure 4.7: Reflection Coefficient for Alfvén Resonator, $\Sigma_P = 10$, $\epsilon = 0.01$

Unlike the uniform Alfvén speed case discussed in Chapter 3, there is a apparent resonance structure for waves in the IAR. As can be seen in Figure 4.7, the minima of the reflection coefficient closely agree with the Bessel function zeros from Table 4.3 (the appropriate limit for comparison).

Grzesiak[30] analyzed data from the Freja satellite and used a cross-phase wavelet method[11] to show that the observed signatures were consistent with an earlier theoretical model of Lysak[43],[44]. Specifically, Grzesiak showed that the relative phase between the electric and magnetic field at Freja could were consistent with the Bessel function representation of E_x and B_y and the superposition of fields obtained using the reflection coefficient of Equation (4.39). As an aside, we should note that the spectral power of Grzesiak's Freja observations showed only weak harmonic structure, and the phase relationship was cited as the best evidence of IAR excitation.

[11] We will use a similar technique in Chapter 6.

4.5.1 Reflection Coefficient Method for IAR Cavity Modes

One possible issue with interpretation of actual observations using the Bessel function representation of the IAR fields is the failure of the Alfvén speed profile to accurately reflect structure in the magnetosphere. Noting this, Lysak[45] developed a numerical method to calculate reflection coefficients for general density and magnetic field models.

In the case of ideal MHD, it can be shown that there are two characteristic variables, conventionally denoted by $Z_{\pm}$, which describe the propagation of Alfvén waves either parallel (+) or antiparallel (-) to the magnetic field. These Elsässer variables are defined according to $\mathbf{Z}^{\pm} = \mathbf{u} \pm \mathbf{B}/\sqrt{\mu_0 \rho}$, where $\mathbf{u} = \mathbf{E} \times \mathbf{B}_0 / B_0^2$. Once the Alfvénic electric and magnetic fields can be calculated, the Alfvén wave reflection coefficient can be determined directly from the Elsässer variables.

This method has the advantage of being insensitive to the details of the underlying plasma model being used, unlike the exact equations obtained using the Greifinger model. For example, Lysak used the inhomogeneous power-law density model along with a quasi-dipolar magnetic field to obtain results which showed decent agreement with observations from the Viking satellite[45]. On the other hand, this method has the disadvantage of not providing quantitative information regarding the damping rate of the normal modes (relative strength of the damping can be inferred from the width of the minima). Moreover, the Elsässer variable formulation is only valid for Alfvén waves (or field-aligned magnetosonic waves), and cannot be applied to the waveguide mode.

Reflection Method Description

In terms of the characteristic variables for the IAR cavity mode, the Elsässer variables $Z^{\pm}$ are

$$Z^{\pm} = E_x \mp V_A B_y \tag{4.40}$$

As mentioned above, $Z^{\pm}$ correspond to upwards and downwards propagating Alfvén waves. The complex reflection coefficient for Alfén waves is defined to be the ratio of the Elsässer variable magnitudes,

$$R^A = \frac{Z^+}{Z^-} \tag{4.41}$$

Note that the exact expression derived above for the reflection coefficient (Equation 4.39) of the Greifinger model is simply an analytical expression of (4.41) with the Bessel function expressions for E_x and B_y having been inserted.

Lysak[45] used a dipolar magnetic field profile and two-species density model[12] but was able to ignore the effects of field geometry because of the small perpendicular wavelengths being considered (the primary concern of the paper was the inertial Alfvén wave of Chapter 2 and associated $E_{\|}$), allowing him to use the expressions from Cartesian geometry.[13] However, because we are concerned with mesoscale waves for which geometrical effects may be important, we must consider the equations in proper dipole coordinates.

[12] See Appendix D for details.

[13] This is more or less equivalent to considering the fields directly above the magnetic pole.

Decoupled Alfvén Resonator Equations

The Alfvénic modes are associated with compression-free toroidal or poloidal oscillations.[14] The primary difference between the Cartesian and Dipole models is that the details of the transverse direction are important - the magnetic field and Alfvén speeds can be assumed to be uniform in the $\hat{e}_\phi$-direction, but they vary in the $\hat{e}_\nu$-direction. Thus toroidal oscillations, which produce azimuthal velocity perturbations, may exhibit different properties from the the poloidal oscillations. We will limit our consideration here to purely toroidal modes, as observations indicate that this is the primary polarization of IAR cavity modes.

$$\frac{\partial \mathcal{B}_\phi}{\partial \mu} = i\omega \frac{g_{\phi\phi}}{c_A^2} \mathcal{E}_\nu \tag{4.42}$$

$$\frac{\partial \mathcal{E}_\nu}{\partial \mu} = i\omega g_{\nu\nu} \mathcal{B}_\phi \tag{4.43}$$

These equations can be combined to find a single wave equation for the electric field,

$$\frac{\partial}{\partial \mu} \frac{1}{g_{\nu\nu}} \frac{\partial \mathcal{E}_\nu}{\partial \mu} = -\frac{g_{\phi\phi}\omega^2}{c_A^2} \mathcal{E}_\nu \tag{4.44}$$

This is a standard second-order differential equation which is complicated primarily by the ionospheric boundary condition.[15] Even with the requirement of complex-valued

[14] We can straightforwardly associated the Cartesian components with the dipole components according to $B_x \to \mathcal{B}_\nu$, $B_y \to \mathcal{B}_\phi$, and $B_z \to \mathcal{B}_\mu$ with similar transcriptions for the electric fields.

[15] Specifically, Equation (4.44) is the Sturm-Liouville differential equation. For certain classes of boundary conditions (c.f. Arfken[8]), the solutions of this equation are well-understood and well-behaved. This is not necessarily the case for a conducting ionosphere.

fields, standard numerical integration techniques such as the Runge-Kutta method[73] are sufficient for our purposes.

Reflection in a Dipole Field

Calculation of the reflection coefficient begins by specifying an electric field at the ionosphere and determining the corresponding magnetic field according to the ionospheric jump condition, which in the case of Alfvén waves with a spherical ionosphere is $B_\phi = -\mu_0 \Sigma_P E_\theta$, or in terms of the dipole components,

$$B_\phi = -\mu_0 \Sigma_P \cos\alpha E_\nu \tag{4.45}$$

For a given frequency, the coupled Alfvén wave equations (4.42) and (4.43) are integrated upwards with initial conditions determined by the jump conditions (4.45). Integration proceeds from the ionosphere to some altitude above the Alfvén speed maximum. At this point, the dipole Elsässer variables $Z^\pm$ are constructed,

$$Z^\pm = E_\nu \mp V_A B_\phi \tag{4.46}$$

And the reflection coefficient can be determined from (4.41).

Due to the presence of the Alfvén resonator cavity, the ionospheric reflection coefficient is strongly frequency dependent. Lysak[45] considered the effects of this dependence on signal with an $f^{-5/3}$ frequency spectrum. The resultant signals were shown to be in qualitative agreement with Viking observations[52].

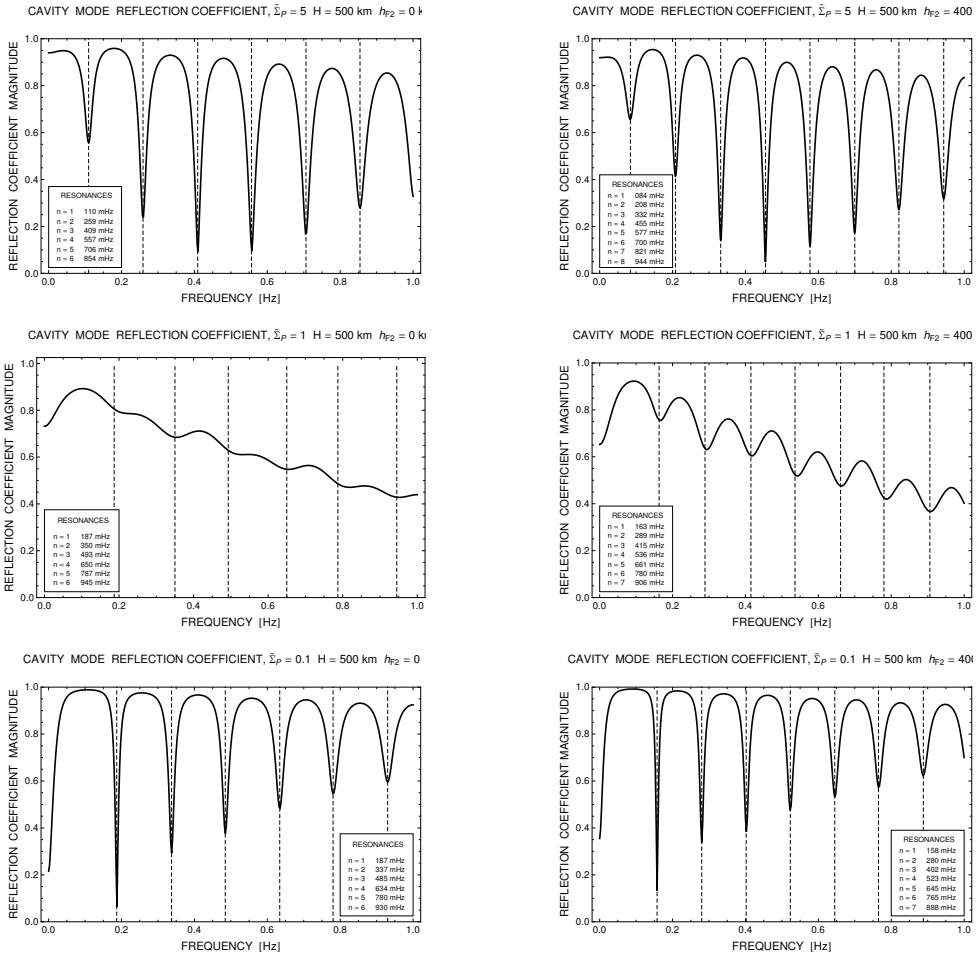

(a) Chapman Density without F_2 (b) Chapman Density with F_2

Figure 4.8: Reflection Coefficient for the IAR Determined from Elsässer Variable Method. Left column is determined for a density profile which maximizes at the Ionosphere, while the right column is for a density profile that maximizes at $400km$. Top Row: $\tilde{\Sigma}_P = 5$. Middle Row: $\tilde{\Sigma}_P = 1$. Bottom Row: $\tilde{\Sigma}_P = 0.1$. Locations of resonances determined using the DIME procedure (described below) are indicated by vertical dashed lines, and the resonant frequencies are given on each plot.

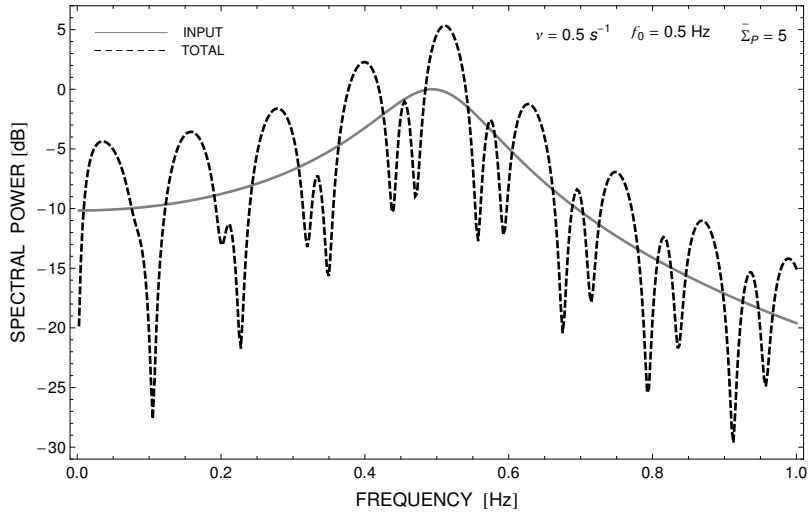

(a) Total Power, $\tilde{\Sigma}_P = 5$

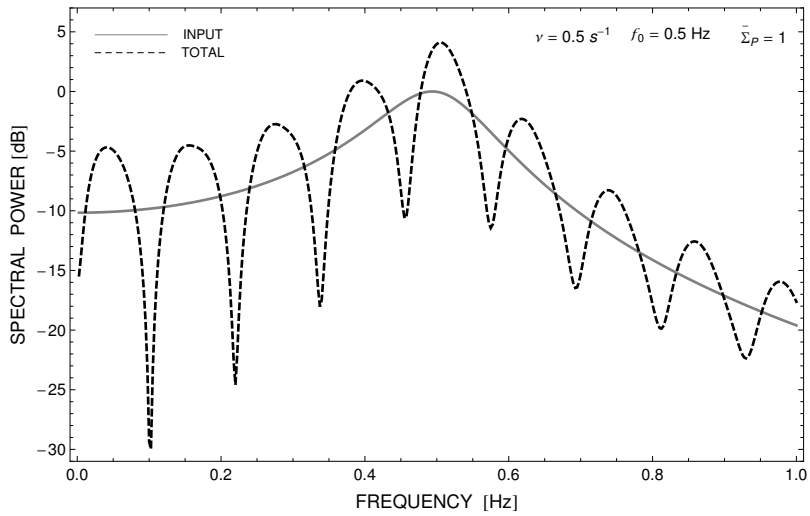

(b) Total Power, $\tilde{\Sigma}_P = 1$

Figure 4.9: Power spectra of electric fields resulting from superposition of incident and reflected waves for an input signal with peak power near 0.5 Hz, observed 1 R_E above IAR peak. a) $\tilde{\Sigma}_P = 5$. b) $\tilde{\Sigma}_P = 1$. Note the presence of small intermediate peaks in the $\tilde{\Sigma}_P = 5$ spectrum occurring near the resonances noted in Figure 4.8. These peaks are not present in the $\tilde{\Sigma}_P = 1$ case, presumably due to the relative shallowness of the resonances caused by increased ionospheric dissipation.

The primary shortcoming of the Reflection Method is that it uses the wave frequency as an input parameter and thus provides no way for the imaginary part of the frequency to be calculated. As we see in Figure 4.8, so long as the damping is not so great (i.e. $\tilde{\Sigma}_P \ll 1$ or $\tilde{\Sigma}_P \gg 1$), the resonances located by the reflection method are very close to the real part of the actual eigenfrequency. However, in the intermediate case, resonances may be offset from the reflection minima by some 10's of mHz. As seen in Figure 4.9, resonance effects on the power spectrum may vary by an order of magnitude on this scale. Thus, in order to properly interpret or predict the effects of the resonator on an input signal, we would like to determine their location as accurately as possible.

In order to address the possible shortcomings of the reflection coefficient approach, we have developed an eigenmode analysis technique that allows us to accurately determine both cavity mode resonant frequencies and damping rates. An additional benefit of this method is that it works equally well for determining eigenvalues of the waveguide mode.

4.6 Downward Integration Method for Eigenvalues (DIME)

In this section, we will outline a numerical method for locating the exact complex frequencies of IAR cavity and waveguide modes in a dipole geometry. We will begin by obtaining systems of coupled equations for the waveguide mode magnetic and electric fields which, along with equations (4.42)-(4.43) for the cavity mode, can be solved using a the DIME procedure, which we will describe below. Using the two-species density model described in Appendix D, we will investigate how the properties of the cavity and waveguide modes determined from a realistic model differ from those obtained from simpler profiles. Finally, we will use DIME to study the characteristics of the IAR eigenmodes for a variety of conditions.

4.6.1 Decoupled Waveguide Equations

There are two possible (decoupled) waveguide modes in dipole coordinates. The first is closely related to the toroidal Alfvén resonator mode, save that it allows for azimuthal variation of the form $e^{im\phi}$,

$$\frac{\partial \mathcal{B}_\phi}{\partial \mu} = \frac{i}{\omega}\left(\frac{g_{\phi\phi}\omega^2}{c_A^2} - m^2\right)\mathcal{E}_\nu \tag{4.47}$$

$$\frac{\partial \mathcal{E}_\nu}{\partial \mu} = i\omega g_{\nu\nu}\mathcal{B}_\phi \tag{4.48}$$

These equations differ from those of the Alfvén resonator mode only in the presence of an azimuthal mode number. The corresponding wave equation is

$$\frac{\partial}{\partial \mu}\frac{1}{g_{\nu\nu}}\frac{\partial \mathcal{E}_\nu}{\partial \mu} = \left(m^2 - \frac{g_{\phi\phi}\omega^2}{c_A^2}\right)\mathcal{E}_\nu \tag{4.49}$$

The presence of m^2 is an important difference, however, as it allows for the possibility of a positive right hand side. When this is the case, waves can exhibit non-oscillatory behavior - including spatial localization due to asymptotic evanescence. Unlike the Cartesian waveguide mode discussed earlier, there are only finite number of values of the transverse wave number allowed. (An arbitrary localized wave structure can still be constructed from a superposition of harmonics, however).

In addition to the finite-m toroidal mode (an azimuthally propagating magnetosonic mode), there is also a poloidal mode. This mode is naturally represented by the remaining Maxwell equations for $\mathcal{E}_\phi$ and $\mathcal{B}_\nu$, and the associated wave equation is

$$\frac{\partial}{\partial\mu}\frac{1}{g_{\phi\phi}}\frac{\partial\mathcal{E}_\phi}{\partial\mu} = -\left(\frac{\partial^2}{\partial\nu^2} + \frac{g_{\nu\nu}^2\omega^2}{c_A^2}\right)\mathcal{E}_\phi \tag{4.50}$$

Equation (4.50) is complicated by the absence of a simple normal-mode structure in the meridional direction. However, if we note that variations in plasma and field parameters is typically slow (except in the vicinity of a sharp plasmapause, when surface wave excitation becomes possible), it makes sense to use a WKB-type approximation for the meridional variations. Let us suppose a characteristic meridional wavelength λ_ν and corresponding wave number $k_\nu = 2\pi/\lambda_\nu$. Under the reasonable assumption of slow meridional variation, we can make the transcription $\partial_\nu \rightarrow ih_\nu k_\nu$, resulting in the poloidal wave equation

$$\frac{\partial}{\partial\mu}\frac{1}{g_{\phi\phi}}\frac{\partial\mathcal{E}_\phi}{\partial\mu} = g_{\nu\nu}\left(k_\nu^2 - \frac{\omega^2}{c_A^2}\right)\mathcal{E}_\phi \tag{4.51}$$

As was the case for the Cartesian waveguide equation, this mode described by (4.51) allows for a spectrum of dependences with respect to the transverse wave number. The only requirement is that the wavelength is smaller that the characteristic scale length of variations in the IAR region plasmas. We can estimate reasonable values of the meridional wave number by considering the meridional waveguide region to have a characteristic length ℓ_ν, which for a waveguide spanning $2 \leq L \leq 20$ is about $0.5R_E$. The corresponding fundamental wavelength of a meridional mode is $\lambda_\nu = 2\ell_\nu = 1R_E$ and the meridional wave number spectrum is given by $k_\nu = 2\pi n R_E^{-1}$.

4.6.2 Numerical Method

The obvious method for solving either the IAR or waveguide equations is to specify an unit electric field at the ionosphere and use the ionospheric jump conditions to obtain an expression relating the electric field and its derivative. Unfortunately, this method does not guarantee that we follow the correct wave mode into the magnetosphere. In fact, it is almost guaranteed to not follow the correct waveguide mode - the asymptotically dominant solution is the exponentially increasing incoming wave rather than the exponentially decreasing outgoing wave.

In order to correctly follow the desired wave modes, we instead begin our integration in the magnetosphere and move down the field line to the ionosphere. In this case, the dominant waveguide mode is the evanescent outgoing wave. The only difficulty with this prescription is finding correct initial conditions.

In order to obtain an expression relating the the electric fields to their derivatives, we make use of the WKB approximation in the distant (relatively speaking) magnetosphere. Although the WKB approximation breaks down in the IAR region due to the exponential density variation, it is quite accurate beyond the Alfvén speed peak, where the electromagnetic fields behave like plane waves. The first-order WKB approximation (Appendix C) gives us the following approximate (but demonstrably accurate) initial conditions

$$\frac{\partial \mathcal{E}_\nu}{\partial \mu} = \pm h_\nu \sqrt{m^2 - \frac{g_{\phi\phi}\omega^2}{c_A^2}}\mathcal{E}_\nu \tag{4.52}$$

$$\frac{\partial \mathcal{E}_\phi}{\partial \mu} = \pm h_\mu \sqrt{k_\nu^2 - \frac{\omega^2}{c_A^2}} \mathcal{E}_\phi \tag{4.53}$$

In both cases, the positive (negative) sign corresponds to an upgoing (downgoing) wave. Note that in the last equation, we have made use of the identity $h_\nu h_\phi = h_\mu$. In addition, in order to follow the asymptotically evanescent modes the $\pm$ should be replaced by $\mp$ in the above initial conditions.

Having specified the correct initial conditions for an outgoing wave, we then proceed to integrate to the ionosphere where the jump conditions are evaluated. Only certain frequencies will allow the jump conditions to be satisfied, and we can identify these as the eigenfrequencies of the Alfvén resonator/waveguide. We locate the eigenfrequencies using a shooting method as discussed in Appendix B.

4.6.3 Cavity Mode Frequencies

As described, the DIME procedure can be used for any magnetic field geometry with any suitable density profile.[16] We will apply the method to the solution of the dipole equations below, but first we will demonstrate the importance of allowing for generalization of the Alfvén speed profile by solving the Cartesian equivalents - essentially, Equations (4.9) and (4.10).

For simplicity, we will use a modification of the Greifinger density profile that allows us to include a minor variation, the presence of a local Alfén speed minimum above the ionosphere. Specifically, we use an Alfvén speed profile given by

[16] We discuss this briefly at the end of his chapter.

$$V_A = \frac{V_I}{\sqrt{\epsilon^2 + e^{1-(z-z_0)/H - e^{-(z-z_0)/H}}}} \tag{4.54}$$

This profile has replaced the normal exponential of the Greifinger model with a Chapman layer centered on z_0. The effective height of a Chapman profile differs from that of an exponential one, but that itself should not result in any qualitative differences and the Alfvén speed profiles look quite similar. In Figures 4.10 and 4.11, we show the results for two similar situations, with $V_I = 700$ km/s, $H = 0.075R_E$, and $\epsilon = 1/100$. The only difference between the two figures is that for Figure 4.10, we use $z_0 = 0$ while in Figure 4.11, we use $z_0 = 0.06R_E$. Comparing these figures, we see that the presence of a minimum away from the ionosphere fundamentally alters the relationship of the cavity modes to the Ionospheric conductance.

Figures 4.11 and 4.10 display a fundamentally different behavior in the neighborhood of $\tilde{\Sigma}_P = 1$. In the absence of a discrete F_2 peak (that is, when the peak does not coincide with the ionospheric boundary), the eigenfrequency decreases through $\tilde{\Sigma}_P$ with increasing Pedersen conductance. On the other hand, when the F_2 peak is separated from the ionospheric layer, the frequency instead decreases.

Recall from the Greifinger solution that the small conductivity case corresponded to frequencies determined by the roots of the J_1 Bessel function while the large conductance case corresponded to roots of the J_0 Bessel function. Since $E_x \propto J_0$ and $E'_x \propto J_1$, this indicates that a Dirichlet-like conditions ($E_x \sim 0$) at the ionosphere correspond to lower frequencies than Neumann-like conditions ($E' \sim 0$). Generally speaking, regions of lower Alfvén speed correspond to regions of lower electric field, and vice versa. When the Alfvén speed minimum and a strongly conducting ionosphere coincide, we would naturally expect the frequency to be dominated by a Dirichlet-like solution. However,

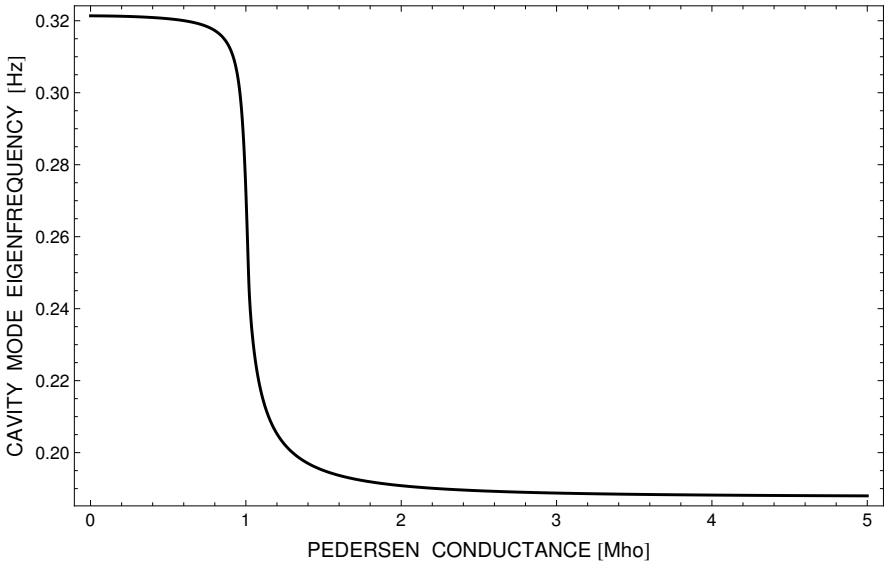

(a) IAR Frequency, Chapman Density without F_2

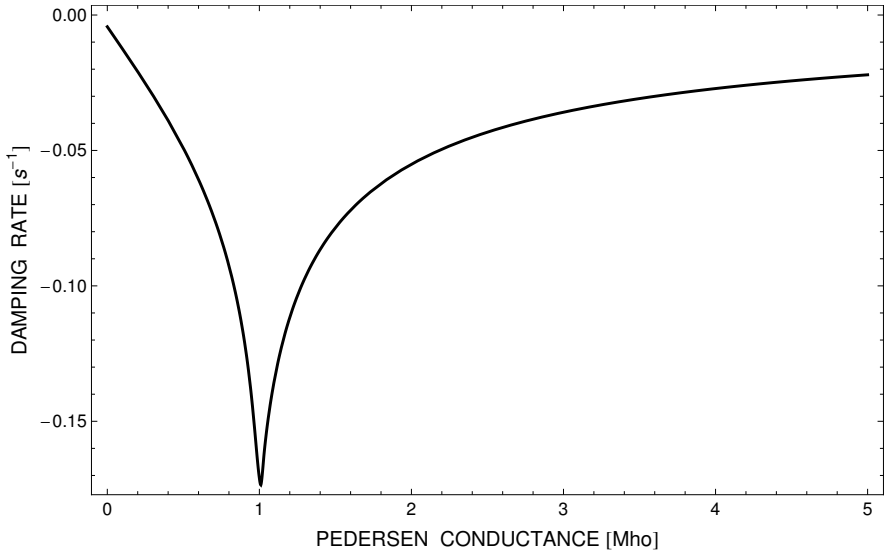

(b) IAR Damping, Chapman Density with F_2

Figure 4.10: Characteristics of IAR Determined from DIME of cavity mode first harmonic with no F_2 peak. A) Oscillation Frequency. B) Damping Rate. Behavior is qualitatively similar to Greifinger's solution.

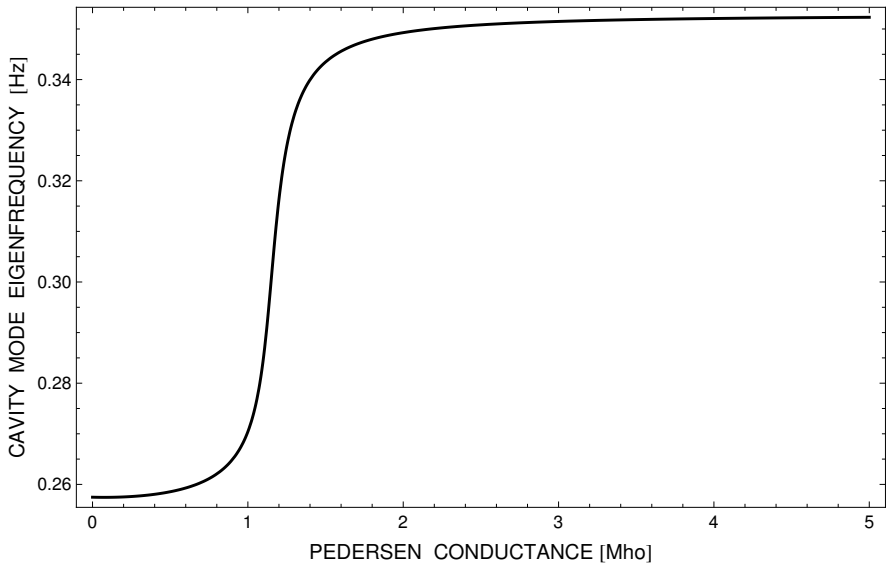

(a) IAR Frequency, Chapman Density with F_2

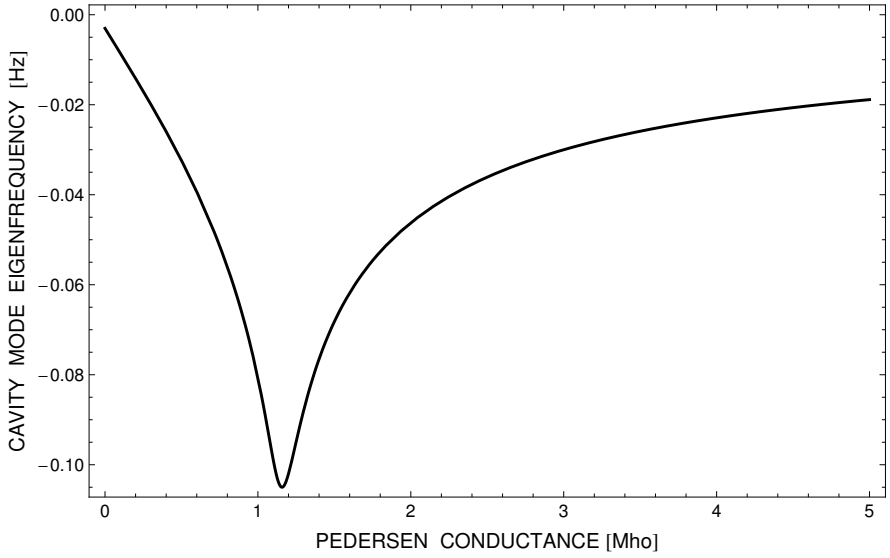

(b) IAR Damping, Chapman Density with F_2

Figure 4.11: Characteristics of IAR Determined from DIME of cavity mode first harmonic with F_2 peak. A) Oscillation Frequency. B) Damping Rate. Note that the presence of a local minimum causes a drastic change in the cavity mode's frequency response, with frequency increasing across $\tilde{\Sigma}_P = 1$ rather than decreasing.

when the Alfvén speed maximum and strongly conducting layer are separated, the function must oscillate more quickly to simultaneously satisfy the need for a local minimum at the Alfvén speed peak and a node at the conducting boundary, thus resulting the in the predicted modification of eigenfrequency as a function of Pedersen conductance. The fact that the frequencies appear to be somewhat reduced in the presence of a separated F_2 layer can be attributed to an increase in the effective scale height of the ionosphere, which we will discuss briefly in the next section.

4.6.4 Waveguide Mode Frequencies

Unlike the cavity mode, the controlling factor of the waveguide mode frequency is not only the Pedersen conductance, but also the perpendicular wavenumber. As a result, the qualitative shift in behavior that was exhibited when the F_2 peak is separated from the ionospheric boundary is absent from the waveguide mode. As earlier noted, the waveguide mode is confined to the region of space surrounding the F_2. By moving the peak to a higher altitude provides an effective increase in the region of space in which the waveguide mode is non-evanescent, resulting in an increase of the effective scale height - for example, with $r_{F2} = 1.06R_E$ and $H = 0.075R_E$, the Alfén speed at the ionosphere and 1000 km are the same, whereas in the coincident case, the speed is monotonically increasing. Since the IAR eigenfrequencies vary inversely with scale height, the eigenfrequency of the waveguide mode decreases when the F_2 layer is separated from the ionosphere.

We demonstrated the effects of including a separated F_2 layer in the previous section, so we will here focus only on the case of a separate F_2 layer. Using the DIME procedure, we obtain the waveguide eigenfrequencies as a function of perpendicular wavenumber (k_ν) and Pedersen conductance (Σ_P), and also the associated group speeds. In Figure

4.6.4, we see that the waveguide frequency is insensitive to k_ν for long perpendicular wavelengths[17] and varies linearly with k_ν at smaller wavelengths. For fixed k_ν, we see that the frequency is relatively insensitive to variations in Pedersen conductance, while the damping shows large variability, although it is never very strong ($\gamma/\omega \sim 0.1$ at most). It is interesting to note that there is no damping in the zero conductance limit, indicating that the waveguide mode is entirely confined to the Alfvén resonator region. This is in contrast to the cavity mode, which has small but finite losses even at $\tilde{\Sigma}_P = 0$ due to leakage from the resonator cavity (see e.g. Figure 4.11(b)).

Waveguide Mode Group Velocity

As shown earlier, the group velocity can be obtained by numerically calculating the derivative of the eigenfrequency with respect to wavenumber. This is the method used to generate Figure 4.14. The solutions obtained using DIME are qualitatively similar to those of the Greifinger model, but the predicted group speeds are much different. Instead of always being somewhere above the minimum Alfvén speed, as was the case in Figure 4.4, it is almost entirely below the minimum (610 km/s, in this case). The exception occurs near $k_\nu = 1\ R_E^{-1}$, which may correspond the trapped/untrapped limit as evidenced by the abrupt change in qualitative behavior of the waveguide mode damping seen in Figure 4.12(b). Unlike the Greifinger model results, only a very small increase in group speed is observed at this transition. This is most likely due to the difference in Alfvén speed profiles along with the effects of geometrical dispersion, which are absent from the Greifinger model.

[17] In this regime the waves are not trapped and act much more like cavity modes.

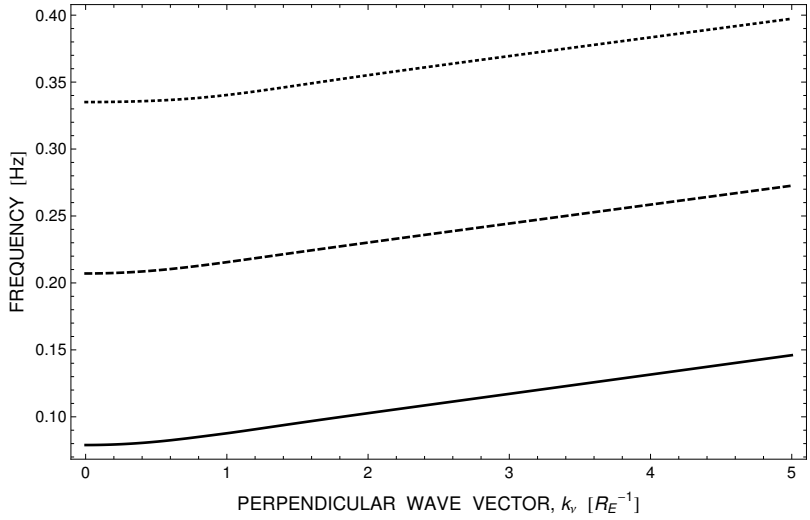

(a) Waveguide Frequency, Chapman Density with F_2

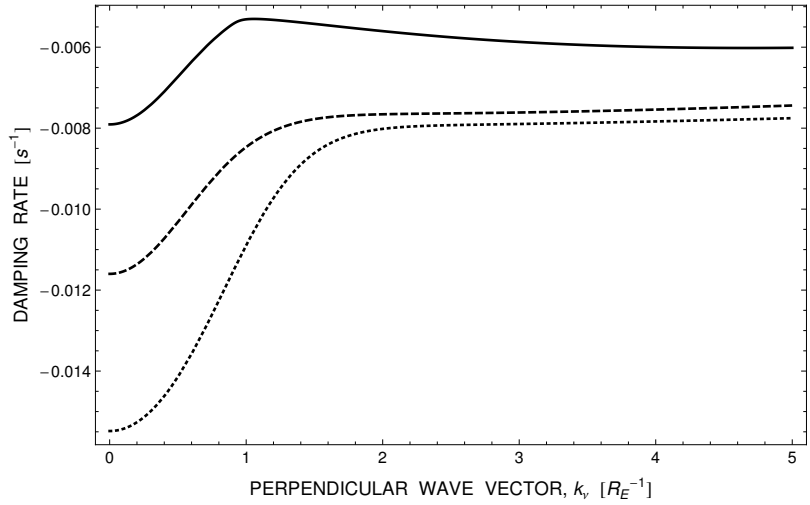

(b) Waveguide Damping, Chapman Density with F_2

Figure 4.12: Eigenfrequency determined from DIME of waveguide mode as a function of perpendicular wave vector. Alfvén speed profile includes F_2 layer. (a) Oscillation frequency. (b) Damping rate. Solid line: fundamental. Dashed line: first harmonic. Dotted line: second harmonic.

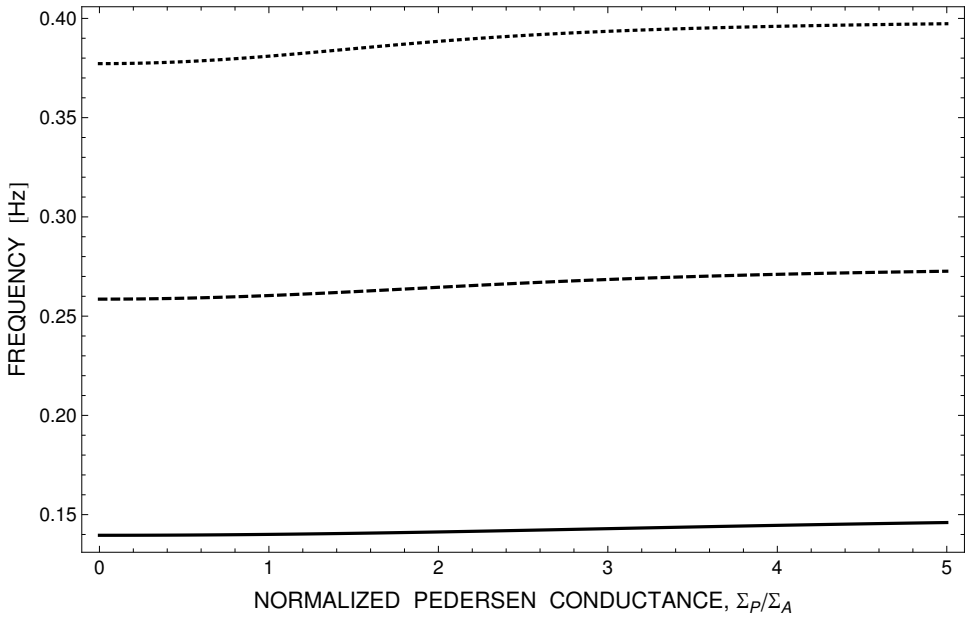

(a) Waveguide Frequency, Chapman Density with F_2

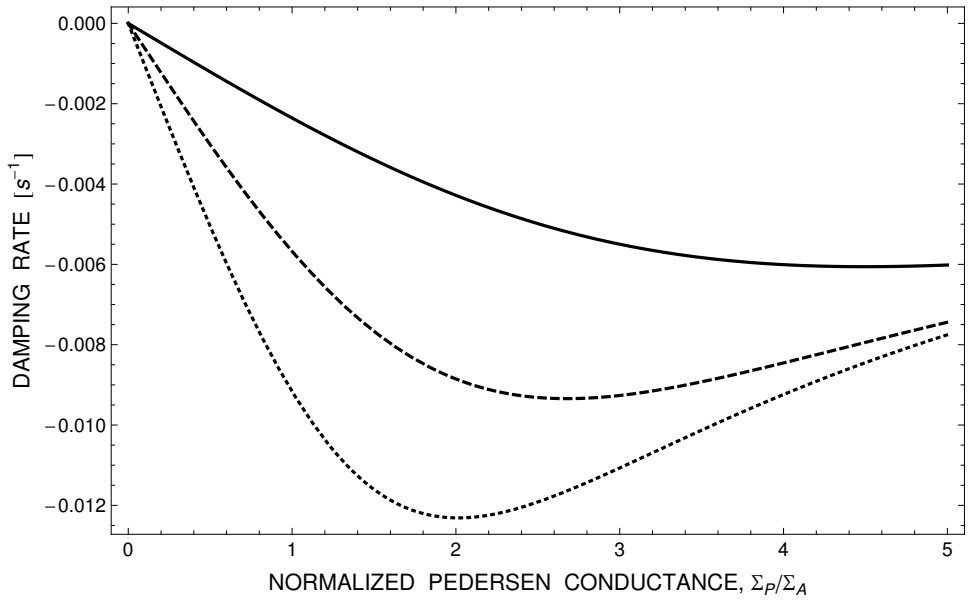

(b) Waveguide Damping, Chapman Density with F_2

Figure 4.13: Eigenfrequency determined from DIME of waveguide mode as a function of Pedersen conductance. Alfvén speed profile includes F_2 layer. (a) Oscillation frequency. (b) Damping rate. Solid line: fundamental. Dashed line: first harmonic. Dotted line: second harmonic.

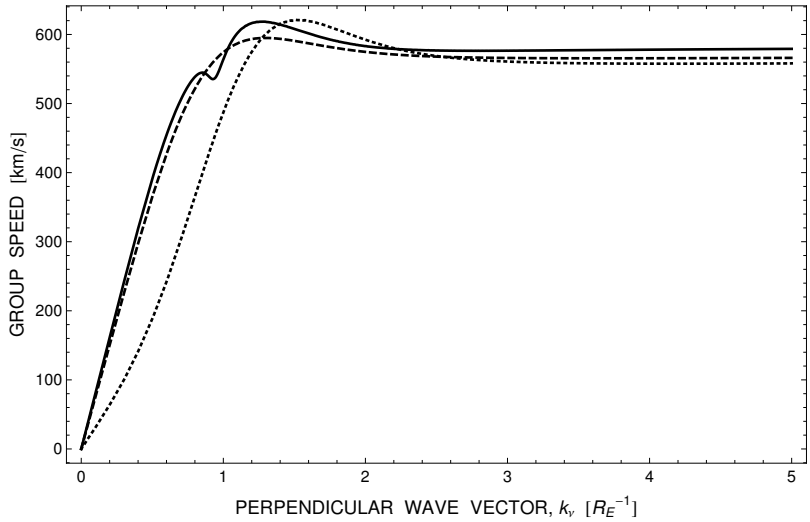

(a) Waveguide Group Speed and Perpendicular Wavevector, Chapman Density with F_2

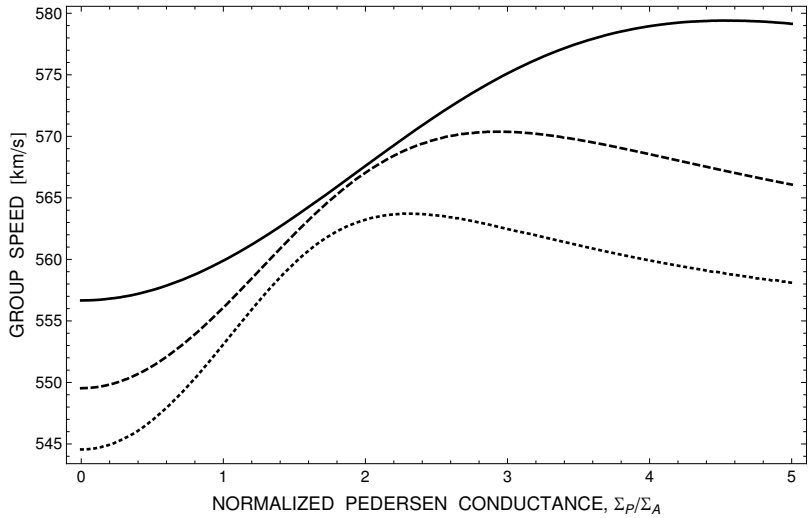

(b) Waveguide Group Speed and Pedersen Conductance, Chapman Density with F_2

Figure 4.14: Group speed determined from DIME of waveguide mode. Alfvén speed profile includes F_2 layer. (a) As function of Pedersen perpendicular wave vector, $\tilde{\Sigma}_P = 5$. (b) As a function of Pedersen conductance, $k_\nu = 5$. Solid line: fundamental. Dashed line: first harmonic. Dotted line: second harmonic.

Chapter 5

Simulation of ULF Wave Propagation

5.1 Background

A well known result from the theory of differential evolution equations is that the amplitudes of non-resonant signals decay exponentially with time while resonances can be maintained without the input of energy over much longer timescales. In the previous chapter, we developed a numerical method for obtaining eigenfrequencies of the Alfvén resonator. In this chapter, we discuss methods for simulating the temporal development of ULF waves in a realistic dipole magnetosphere. The results of this simulation will be used to observe the transition from transient to resonant modes, characterize the spatial structure of magnetospheric ULF waves, and verify the results of the downward integration model in Chapter 4.

5.2 Non-Orthogonal Dipole Coordinates

As earlier discussed, the dipole coordinates of Chapter 2 are very useful for studies of magnetospheric ULF waves. Recall that these coordinates are defined as

$$\nu = -\frac{\sin^2\theta}{r} \qquad \phi = \phi \qquad \mu = \frac{\cos\theta}{r^2} \tag{5.1}$$

However, the utility of dipole coordinates is reduced by the presence of a spherically-symmetric Ionosphere. Since $\mu = \cos\theta/r^2$, the ionosphere ($r = 1$) does not correspond to a coordinate surface. As will be discussed later in this chapter, it is desirable that all boundaries of our simulation coincide with coordinate surfaces. Thus, we need to modify the dipole coordinates so that the Ionosphere is a coordinate surface.

Lysak[48] modified the dipole coordinates by introducing a normalization factor $\mu_I = \sqrt{1+\nu}$ to μ. This has the effect of making the ionosphere a coordinate surface, but it also introduces a dependence of once coordinate upon another. As a consequence of this interdependence, the coordinate surfaces may not be mutually orthogonal and are therefore referred to as non-orthogonal coordinates. The use of such coordinates introduced a number of mathematical complications (discussed in detail in Appendix A), but they retain many of the advantages of ordinary dipole coordinates.

In terms of the dipole coordinates introduced in Chapter 1, the scaled conformal dipole coordinates are

$$x^1 = \nu \qquad x^2 = \phi \qquad x^3 = \frac{\sinh^{-1}(a\mu/\mu_I)}{\sinh^{-1}(a)} \tag{5.2}$$

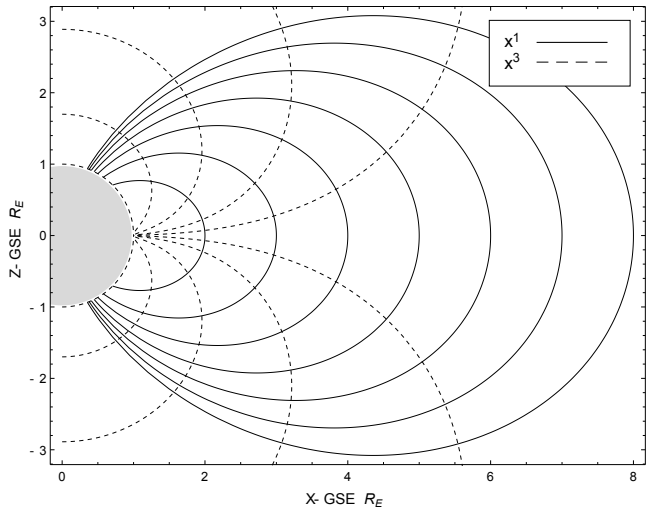

Figure 5.1: Non-Orthogonal Dipole Coordinate Surfaces

Here $\mu_I = \sqrt{1+\nu}$ is the value of μ at the ionosphere and a is a scaling parameter which affects certain properties of quantities derived from the x^3 coordinate, the need for which will be established later on. Note that in the limit $a \to 0$, the coordinate simplifies to that of [Lysak, 2004]. Notice that the coordinates have been normalized so as to be dimensionless.

The contravariant basis vectors of this coordinate system are

$$\varepsilon^1 = h^\nu \hat{e}_\nu \qquad \varepsilon^2 = h^\phi \hat{e}_\phi \qquad \varepsilon^3 = h^3 \left(\cos\gamma \hat{e}_\mu - \sin\gamma \hat{e}_\nu\right) \tag{5.3}$$

Where h^3 and γ are given by

$$h^3 = \frac{\alpha}{\cos\gamma} h^\mu \qquad \gamma = \tan^{-1}\left(\beta \frac{h^\nu}{h^\mu}\right) \tag{5.4}$$

And the parameters α and β are

$$\alpha = \frac{1}{\mu_I} \frac{a}{\sqrt{1 + (a\frac{\mu}{\mu_I})^2}\sinh^{-1}(a)} \qquad \beta = \frac{\mu}{2\mu_I^2} \tag{5.5}$$

The covariant basis vectors can be obtained from the contravariant vectors as discussed in Appendix A (and briefly, below).

A comparison the contravariant non-orthogonal basis vectors $\varepsilon^1, \varepsilon^2, \varepsilon^3$ and the orthogonal dipole basis vectors are shown in Figure 5.2. Notice that the angle between these basis vectors approaches 90° at the equator, where they coincide with the orthogonal dipole bases.

Ionospheric Limits

At the ionosphere, $\cos\gamma$ simplifies to

$$\cos\gamma = \frac{2\cos\theta}{\sqrt{1 + 3\cos^2\theta}} \tag{5.6}$$

We note in Appendix D that the RHS of (5.6) is equal to the cosine of the angle between the dipole magnetic field and the radial unit vector, $\hat{e}_r \cdot \mathbf{B}_0/B_0$. This equality isn't really surprising, though, since we know that the ε_3 is parallel to to the background magnetic field and we know that $r = R_I$ is an iso-surface of the x^3 coordinate,[1] which indicates

[1]There is a potential issue at $\theta = \pi/2$, where it switches from $-\hat{e}_r$ to $\hat{e}_r$, but we don't include the

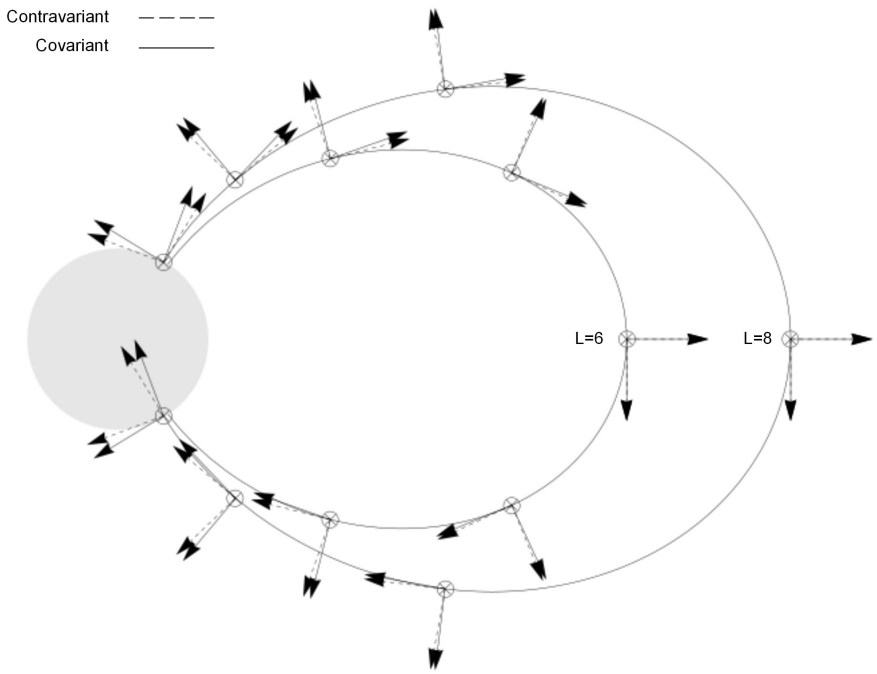

Figure 5.2: Basis Vectors of Non-Orthogonal Dipole Coordinates

that ε^3 should be (anti)parallel to $\hat{e}_r$ at the ionosphere. Consequently, ε_1 should be (anti)parallel to the $\hat{e}_\theta$ unit vector at the ionosphere, e.g. (5.8). Explicit expressions for these basis vectors at the ionosphere are

$$\varepsilon^3 = \mp\frac{\alpha h^\mu}{\cos\gamma}\hat{e}_r \qquad \varepsilon_1 = \mp\frac{h_\nu}{\cos\gamma}\hat{e}_\theta \tag{5.7}$$

Where $\pm$ apply to the Northern and Southern hemisphere, respectively. These expressions are valuable because they allow us to treat the ionosphere as a spherical boundary while dealing directly with the components still expressed in non-orthogonal dipole coordinates.

Interpretation of γ

Although they are not normalized, complementary covariant and contravariant basis vectors are orthogonal, i.e. $\varepsilon^i \cdot \varepsilon_j = \delta^j_i$.[2] If we consider either of the products $\varepsilon^1 \cdot \varepsilon_1$ or $\varepsilon^3 \cdot \varepsilon_3$, we find that γ is the angle between the orthogonal dipole basis vectors and the non-orthogonal basis vectors. This is consistent with the ionospheric result, but more general.

5.2.1 Covariant Bases

Knowing the contravariant bases and the Jacobian, we can determine the covariant basis vectors using

equatorial ionosphere and don't encounter this.

[2]This can be demonstrated directly from the cross-product formula which relates them.

$$\varepsilon_i = J(\varepsilon^j \times \varepsilon^k) \tag{5.8}$$

Where the $J^{-1} = \varepsilon^1 \times \varepsilon^2 \cdot \varepsilon^3$ is the Jacobian. Using our expressions for the contravariant bases from earlier, we find

$$J = \frac{1}{h^\nu h^\phi h^\mu \alpha} \tag{5.9}$$

We see that the Jacobian of the non-orthogonal system differs from that of orthogonal dipole coordinates by a factor of α^{-1}.

Explicit expressions for the covariant dipole basis vectors are

$$\varepsilon_1 = h_1 \left(\cos\gamma \hat{e}_\nu + \sin\gamma \hat{e}_\mu\right) \qquad \varepsilon_2 = h_\phi \hat{e}_\phi \qquad \varepsilon_3 = \frac{h_\mu}{\alpha}\hat{e}_\mu \tag{5.10}$$

Where

$$h_1 = \frac{h_\nu}{\cos\gamma} \tag{5.11}$$

Comparison to Orthogonal Dipole Coordinates

As previously mentioned, the Jacobian is locally scaled by the α parameter as are the covariant x_1 and contravariant x^3 scale factors. Given that all of these factors are geometrical quantities, it is not too surprising that such relationships to the ordinary dipole coordinates should exist. Indeed, the orthogonal dipole coordinates are simply

one limit of a more general system - if the simultaneous limits $a \to 0$ and $\mu_I \to 1$ are taken, the orthogonal system of Chapter 2 is obtained.

5.3 Numerical Solution of Maxwell's Equations

In Chapter 4, we studied the IAR region using both analytical and numerical models. Although the analytical models were satisfying in that they provide a definite expression for an answer, we were only able to obtain such answers for specific plasma models. In a similar manner here, analytical solutions of Maxwell's equations are not easily (if at all) obtainable in this model. Not only are we dealing with a more complicated system of coordinates, we must also acknowledge the intrinsic multi-dimensionality of the magnetosphere system. Consequently, we must - as before - resort to numerical methods.

5.3.1 Yee's Formulation

The time evolving Maxwell equations involve a number partial derivatives relating various components of the electromagnetic field. It was shown by Yee[98] that the Maxwell equations can be represented on a discrete grid by arranging the field components on a cube. As shown in Figure 5.3, the electric fields are arranged on midpoints of each edge, and the magnetic fields are arranged on the midpoint of each face. This arrangement allows for the central difference approximation to be used for every spatial derivative. More information about this approach, commonly known as the Finite-Difference Time Domain (FDTD) method, can be found in a comprehensive text by Taflove and Hagness[90].

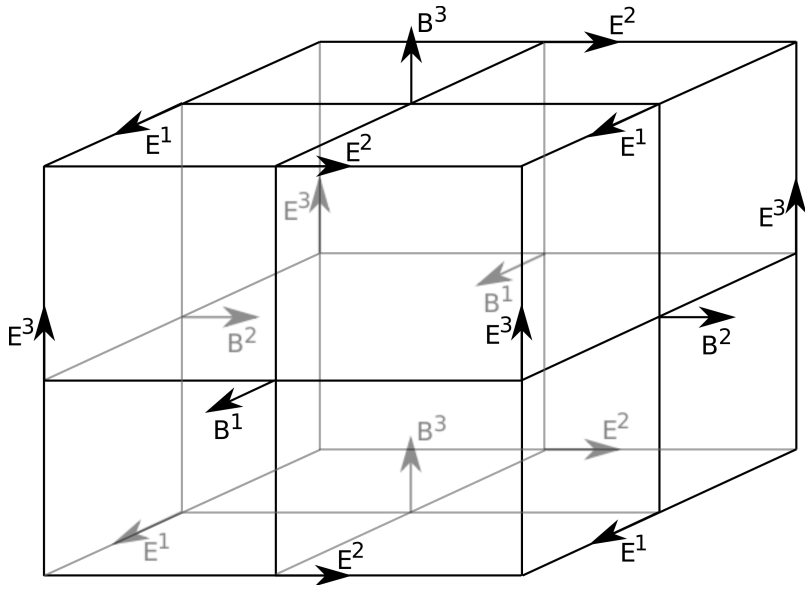

Figure 5.3: Yee's Grid for the Finite Difference Time Domain Method

5.3.2 Computational Grid

The full 3-D grid is obtained from the tensor product of three uniform 1-D grids. The domain is bounded in latitude and longitude by selecting a low- and high- L-shell; since $x^1 = -1/L$, it is sufficient to specify a desired range of L-shells (or invariant latitude). We allow for arbitrary azimuthal structure by considering the entire x^2 axis. The domain is bounded from below by the ionosphere, which is a surface of constant x^3, with $x^3 = \pm 1$ for the Northern and Southern hemispheres, respectively. The domain is bounded from above by a second surface of constant x^3 whose value can be freely specified.[3]

[3]In practice, we define the outer boundary by specifying a radial distance on some L-shell.

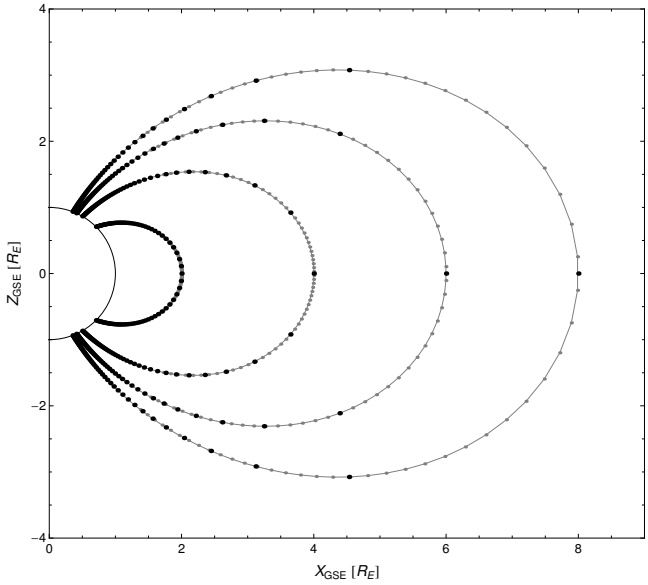

Figure 5.4: Comparison of coordinate spacing. One hundred and one points of both dipole coordinates and scaled dipole coordinates are plotted on each field line. Normal dipole coordinates are plotted in black, scaled dipole coordinates are in gray.

5.3.3 Grid Point Spacing

In the specification of the non-orthogonal dipole coordinates above, there is a scaling parameter a which appears in x^3. We have included this in our FDTD formulation because it allows for the control of physical spacing between points on a uniform x^3 grid.

Using a uniformly spaced grid has the advantage of allowing us to use the FDTD method to solve Maxwell's equations while formally maintaining second order accuracy [90]. However, traditional dipole coordinates require a large number of points along a field line to provide good resolution in physical space. The scaled dipole coordinate fixes this problem, allows for nearly uniform spacing along an entire field line with many

fewer points.[4]

5.3.4 Maxwell's Equations on a Non-Orthogonal Grid

Let us suppose that the electric and magnetic fields are defined on a staggered Yee-type grid. If the electric fields are defined on the ionosphere and $\mathcal{E}_2$ and $\mathcal{B}_1$ are defined at the high- and low- latitude boundaries as mentioned previously, then we can represent the magnetospheric fields at any given point in time with 3-dimensional matrices having the dimensions

$$\begin{matrix} \mathcal{E}_1(n_1, n_2, n_3+1) & \mathcal{E}_2(n_1+1, n_2, n_3+1) \\ \mathcal{B}_1(n_1+1, n_2, n_3) & \mathcal{B}_2(n_1, n_2, n_3) & \mathcal{B}_3(n_1, n_2, n_3+1) \end{matrix} \tag{5.12}$$

With these matrices, we can use the FDTD in non-orthogonal dipole coordinates[5] to solve Maxwell's equations. Time derivatives are approximated over a small step Δt, defined according to the Courant condition, which must be satisfied at every grid point

$$\Delta t \leq \frac{1}{V_A \sqrt{\left(\frac{1}{h_1 \Delta x^1}\right)^2 + \left(\frac{1}{h_2 \Delta x^2}\right)^2 + \left(\frac{1}{h_3 \Delta x^3}\right)^2}} \tag{5.13}$$

Optimally, the FDTD method would have $V_A \Delta t = 1$ everywhere, but this is not possible due to the inhomogeneity of the Alfvén speed profile. Instead, we evaluate (5.13) at

[4] For a discussion of particular values of a, see [36].
[5] See [90], Chapter 11 for more details.

every grid point[6] and adopt the smallest Δt. In order to guarantee numerical stability, it may also be necessary to reduce the timestep by a small amount, for instance using a value fractionally smaller than that determined from (5.13).

The fully discretized equations are

$$\mathcal{E}^1\left(i,j,k;t+\frac{\Delta t}{2}\right)=\mathcal{E}^1\left(i,j,k;t-\frac{\Delta t}{2}\right)+ \frac{\Delta t c_A^2}{J}\left(\frac{\mathcal{B}_3(i,j+1,k;t)-\mathcal{B}_3(i,j,k;t)}{\Delta x^2}- \frac{\mathcal{B}_2(i,j,k+1;t)-\mathcal{B}_2(i,j,k;t)}{\Delta x^3}\right) \tag{5.14}$$

$$\mathcal{E}^2\left(i,j,k;t+\frac{\Delta t}{2}\right)=\mathcal{E}^2\left(i,j,k;t-\frac{\Delta t}{2}\right)+ \frac{\Delta t c_A^2}{J}\left(\frac{\mathcal{B}_1(i,j,k+1;t)-\mathcal{B}_1(i,j,k;t)}{\Delta x^3}- \frac{\mathcal{B}_3(i+1,j,k;t)-\mathcal{B}_3(i,j,k;t)}{\Delta x^1}\right) \tag{5.15}$$

$$\mathcal{B}^1(i,j,k;t+\Delta t)=\mathcal{B}^1(i,j,k;t)+ \frac{\Delta t}{J}\left(\frac{\mathcal{E}_2\left(i,j,k;t+\frac{\Delta t}{2}\right)-\mathcal{E}_2\left(i,j,k-1;t+\frac{\Delta t}{2}\right)}{\Delta x^3}\right) \tag{5.16}$$

[6]Given that our plasma model is azimuthally symmetric, we can ignore the x^2 dimension.

$$\mathcal{B}^2(i,j,k;t+\Delta t) = \mathcal{B}^2(i,j,k;t) - \frac{\Delta t}{J}\left(\frac{\mathcal{E}_1\left(i,j,k;t+\frac{\Delta t}{2}\right) - \mathcal{E}_1\left(i,j,k-1;t+\frac{\Delta t}{2}\right)}{\Delta x^3}\right) \tag{5.17}$$

$$\mathcal{B}^3(i,j,k;t+\Delta t) = \mathcal{B}^3(i,j,k;t) - \frac{\Delta t}{J}\left(\frac{\mathcal{E}_2\left(i,j,k;t+\frac{\Delta t}{2}\right) - \mathcal{E}_2\left(i-1,j,k;t+\frac{\Delta t}{2}\right)}{\Delta x^1} - \frac{\mathcal{E}_1\left(i,j,k;t+\frac{\Delta t}{2}\right) - \mathcal{E}_1\left(i,j-1,k;t+\frac{\Delta t}{2}\right)}{\Delta x^2}\right) \tag{5.18}$$

In equations (5.14) - (5.18), time is given as a parameter of the field matrices (it is not a proper dimension). Notice that $\mathcal{E}$ is defined at half-steps in time, while $\mathcal{B}$ is defined at full-steps. This allows us to make use of the same discretization in time as in space. This method is not self-starting, in the vernacular of numerical analysis, in that it requires knowledge of previous steps (such as $t = -\Delta t/2$ for the initial step).

One method to deal with the absence of prior information is to use an alternative, self-starting method such as Runge-Kutta to advance the electric fields from $t = 0$ to $t = \Delta t/2$.[7] This is especially important when dealing with an initially specified configuration of fields (such as those within a resonating cavity). However, if the signals are introduced into the system from an outer boundary, then the magnetic field is actually zero until the point at which the signal is introduced into the system. Because

[7] See e.g. [73], Chapter 19. This is the same method used for integrating the IAR equations in Chapter 4.

this is our approach, we can safely assume that the fields at $t = -\Delta t/2$ are known (and zero).[8]

Once the contravariant fields have been obtained using the Maxwell equations, the covariant fields are obtained using the metric tensor. Since $\mathcal{E}_3 = 0$, the covariant electric fields can be obtained from

$$\mathcal{E}_1 = \frac{\mathcal{E}^1}{g^{11}} \qquad \mathcal{E}_2 = g_{22}\mathcal{E}^2 \tag{5.19}$$

The covariant magnetic field $\mathcal{B}_2$ can be obtained in the same manner as $\mathcal{E}_2$, but it is a little more complicated matter to obtain the covariant magnetic fields $\mathcal{B}_1$ and $\mathcal{B}_3$. Since the fields are not defined at the same location in space, it is necessary to perform an averaging of the each field to obtain it at the position of the other. The most straightforward method (which we adopt) is to perform a four-point average of each field. In this case, the covariant magnetic field $\mathcal{B}_1$ is given by

$$\begin{aligned}\mathcal{B}_1(i,j,k) &= g_{11}\mathcal{B}^1(i,j,k) + \\ &\frac{g_{13}}{4}\left(\mathcal{B}^3(i,j,k) + \mathcal{B}^3(i+1,j,k) + \mathcal{B}^3(i,j,k+1) + \mathcal{B}^3(i+1,j,k+1)\right)\end{aligned} \tag{5.20}$$

And similarly $\mathcal{B}_3$ is given by

[8] Depending on the order of the Runge-Kutta method being used, different results might be obtained by these two methods, but the difference should be negligibly small after a few time steps.

$$\mathcal{B}_3(i,j,k) = g_{33}\mathcal{B}^3(i,j,k)+ \\ \frac{g_{31}}{4}\left(\mathcal{B}^1(i,j,k) + \mathcal{B}^1(i-1,j,k-1) + \mathcal{B}^1(i,j,k-1) + \mathcal{B}^1(i-1,j,k-1)\right) \tag{5.21}$$

At the ionospheric boundary, $\mathcal{B}_3$ is obtained from a slight modification of the above expression,

$$\mathcal{B}_3(i,j,k) = g_{33}\mathcal{B}^3(i,j,k) + \frac{g_{31}}{2}\left(\mathcal{B}^1(i,j,k) + \mathcal{B}^1(i-1,j,k)\right) \tag{5.22}$$

We choose to use this expression rather than make use of the fields below the ionosphere because the distance between grid cells at the ionosphere is much smaller than typical ULF scale lengths and so we expect the fields to be approximately uniform over that distance (whereas screening and rotation effects might result in an unphysical distortion of the fields if the atmospheric fields were used in a four-point average).

Proehl[77] notes that the averaging used in obtaining covariant fields may also serve to remove small-scale noise (smoothing) and to prevent staggered grid decoupling, a form of numerical instability to which the Leapfrog method is susceptible[73].

5.3.5 Boundary Conditions

In our model, there are six boundaries to be considered - low latitude, high latitude, low azimuth, high azimuth, ionosphere, and magnetosphere. The ionospheric boundary condition is based on ideas similar to those discussed in Chapter 3 for Cartesian geometry, but it is much more mathematically involved. Details on the implementation of

the ionospheric boundary condition can be found in Appendix B.

Azimuthal Boundaries

Since we are considering a full 2π radians of azimuth, the natural choice for an azimuthal boundary conditions is periodic boundary conditions (PBCs). That is, we assume that the value after the last value is the first value, and the value before the first value is the last value; implementation is simply matter of properly assigning indices.

From the Maxwell equations above, only (5.14) and (5.18) involve x^2 derivatives. With B^3 being set at $x^2(j)$ and E_1 being at $x^2(j) + \Delta x^2/2$, PBCs are implemented by evaluating the derivatives at the boundary as

$$\mathcal{E}^1\left(i,N,k;t+\frac{\Delta t}{2}\right) = \mathcal{E}^1\left(i,N,k;t-\frac{\Delta t}{2}\right) + \frac{\Delta t c_A^2}{J}\left(\frac{\mathcal{B}_3(i,1,k;t)-\mathcal{B}_3(i,N,k;t)}{\Delta x^2} - \frac{\mathcal{B}_2(i,N,k+1;t)-\mathcal{B}_2(i,N,k;t)}{\Delta x^3}\right) \tag{5.23}$$

and

$$\mathcal{B}^3(i,1,k;t+\Delta t) = \mathcal{B}^3(i,1,k;t) - \frac{\Delta t}{J}\left(\frac{\mathcal{E}_2\left(i,1,k;t+\frac{\Delta t}{2}\right) - \mathcal{E}_2\left(i-1,1,k;t+\frac{\Delta t}{2}\right)}{\Delta x^1} - \frac{\mathcal{E}_1\left(i,1,k;t+\frac{\Delta t}{2}\right) - \mathcal{E}_1\left(i,N,k;t+\frac{\Delta t}{2}\right)}{\Delta x^2}\right) \tag{5.24}$$

Low- and High- Latitude Boundaries

We choose to place $\mathcal{B}_1$ and $\mathcal{E}_2$ on the upper and lower latitude boundaries, and then impose Dirichlet conditions, $\mathcal{B}_1 = \mathcal{E}_2 = 0$. It follows from Maxwell's equations that $\mathcal{B}^1 = 0$ on the boundary, and $\partial\mathcal{B}_3/\partial x^1 = 0$ is likewise implied.

Magnetospheric Boundary

We truncate the domain along a surface of $x^3 = \text{constant}$.[9] This does not correspond to an actual physical boundary, so we must careful to prevent the introduction of non-physical effects into the simulation. This boundary is used for introducing time-dependent electromagnetic signals (by specifying an electric potential ϕ to introduce Alfvén waves or by specifying a compressional magnetic field $\mathcal{B}_3$ to introduce compressional waves), and it allows for outward propagating Alfvén waves by using Elsässer variables, which we discussed in Chapter 4. Specifically, the electric fields at the outer boundary are modified by removing outgoing waves, i.e. assuming that the corresponding Elsässer variable vanishes, $\mathbf{Z}^+ = 0$. At each timestep, the boundary electric fields

[9] Of particular interest may be the case of $x^3 = 0$, corresponding to waves launched from the equator, and $x^3 = -1$ which includes the entire field line. The latter case requires special handling, however, as the methods for introducing signals differ depending on how the boundaries are defined.

are updated according to

$$\mathcal{E}_1(i,j,N+1;t+\Delta t) = \mathcal{E}_1(i,j,N+1;t) - \frac{V_A(i,j,N+1)}{g^{11}(i,j,N+1)h_2(i,j,N)}B_2(i,j,N)$$
$$\mathcal{E}_2(i,j,N+1;t+\Delta t) = \mathcal{E}_2(i,j,N+1;t) + \frac{g_{22}(i,j,N+1)V_A(i,j,N)}{h_1(i,j,N)}B^1(i,j,N) \tag{5.25}$$

As a consequence, parallel propagating waves - all Alfvén waves - are allowed to pass out of the simulation. Obliquely propagating magnetosonic waves are not removed, but we do not expect these waves to be present outside of the Alfvén resonator region.

Ionospheric Boundary

Proper treatment of the ionospheric boundary is made using the ionospheric jump conditions as discussed by Lysak[48],[50]. The method is very similar to the approach discussed in Chapter 3, except that the solution to the atmospheric fields is rather more complicated. Full details of the method for a spherical ionosphere-atmosphere cavity as applied to this simulation are given in Appendix B.

Chapter 6

Simulation of IAR/F2 Signal Evolution

In this Chapter, we compare the time-dependent behavior of signals in the IAR to the properties predicted from the numerical models of the previous chapters. Using results from numerical simulations of ULF wave propagation in a realistic dipolar magnetosphere using the FDTD method described in Chapter 5, we obtain data that can be analyzed directly through waveforms and spectrally using wavelet analysis. We begin this chapter by describing the expected spectral properties of signals entering the IAR and theoretical estimates of IAR mode properties. We will then describe our analysis methods and apply those methods to the simulation data. Spatial properties obtained from spectral estimates will be used as input for the downward integration method of Chapter 4 to confirm the eigenmode nature of the signals.

Having determined the characteristics of the waves seen above the ionosphere, we will analyze the magnetic ground signatures in order to determine what characteristics of

the driving signal can be properly inferred from ground observations. We will then suggest possible implications for the study of Pc1 and Pi1b magnetic pulsations.

6.1 The Spectrum of Scales in the IAR

6.1.1 Temporal Processes

As a rule of thumb, auroral phenomena occur on a one second time scale (although they may be longer, as in the case of stable auroral arcs or shorter, as is the case for flickering aurora). This may change by a factor of a few, depending on conditions in the ionosphere, but is typically the case (due to a relationship between the wave frequency and the ion cyclotron frequency). For example, a survey of Pc1 observed by the AMPTE satellite by Anderson et al. [7] found that Pc1 occurring at $L \geq 6$ were predominantly in the frequency range $0.1 \leq f \leq 1$ Hz. Previous theoretical studies, such as those of Greifinger and Greifinger [28], Fujita and Tamao [22],[23], and the review paper by Lysak and Yoshikawa [50] have identified the characteristic IAR frequency as $V_I/2H$, where V_I is the Ionospheric Alfvén speed and H is the ionospheric scale height. Both cavity and waveguide harmonics are found to be related by some manner of dispersion function (the roots of Bessel functions [28],[50] or a transcendental equation involving complex exponentials [22],[23]) which is on the order of a few. Assuming that $400 \leq V_I \leq 1000$ km/s and $250 \leq H \leq 500$ km, the fundamental frequency is expected to be 0.21 ± 0.15 Hz, suggesting that the first few harmonics of the IAR modes should be at or below 1 Hz, although harmonics - especially when the fundamental frequency is large - can easily exceed 1 Hz. Given the inverse relationship between frequency and wavelength and our focus on mesoscale phenomena, we will consequently limit our consideration to signals with frequencies below 1 Hz.

6.1.2 Spatial Distribution of Input Signals

For the same reason that we don't have a good understanding of the spatial scales of waves in the Alfvén resonator region, the scales of signals which drive these waves are poorly characterized. Multi-satellite conjunctions, either by fortune or design, are infrequent in the near-Earth region. Attempts to measure spatial scales using networks of ground magnetometers have been made by a variety of researchers (for example, [19],[3],[57],[62]), with the typical conclusion being that the perpendicular scale size of the waves is less than the inter-station spacing of the magnetometers (usually a few hundred kilometers).

Gaussian Approximation

The eigenmode problem of Chapter 4 involves the specification of a single perpendicular scale length. However, in practice, most signals are composed of a spectrum of different scale sizes. For example, localized disturbances are often modeled as Gaussian, having an amplitude distribution which is (in one dimension) proportional to

$$F(x) = e^{-\frac{x^2}{2\delta^2}} \qquad f(k) = \delta e^{-\frac{k^2\delta^2}{2}} \tag{6.1}$$

It is well known that the Fourier transform of a Gaussian is itself a Gaussian (given as $f(k)$ above), so we know that such a signal will be characterized by a spectrum of characteristic lengths. Since the wavenumber is essentially an inverse scale length, this spectrum is concentrated at large scales, with 67% of the spectral power[1] being at scales larger than δ.

[1]We define the power of a spectrum $\psi(k)$ as $P(k) = \psi^*(k)\psi(k)$.

Although the majority of signals are probably not Gaussian, we might reasonably expect that the input spectrum of spatial scales should be continuously distributed around some central value. The analytic properties of the Gaussian make it a good starting point for our studies, as it is well characterized and any deviations from a Gaussian distribution can be readily discerned.

6.1.3 Development of Spatial Scales

If a continuous spectrum such as a Gaussian is introduced into an inhomogeneous system, the presence of inhomogeneities should introduce additional structures on the same scale as the inhomogeneity. In the Alfvén resonator region, there are two primary inhomogeneities, the Alfvén speed profile and the Ionospheric conductance. The continuous variation of resonant frequency with latitude resulting from these inhomogeneities allows for the growth of wave power at smaller spatial scales via linear phase-mixing processes.

Linear Phase Mixing

Often discussed in the context of Pc3 field line resonances, phase mixing is a general process which occurs when resonant frequencies are spatially dependent. Let us suppose a simple case where the resonant frequency is an increasing function of a perpendicular coordinate, $\omega_R = \alpha x$. Let us consider points x_1 and x_2. If we simultaneously excite cavity mode oscillations at two points, x_1 and x_2, then the phase at some time t later will $\phi_1 = \alpha x_1 t$ and $\phi_2 = \alpha x_2 t$. From WKB theory, we know that $k_x = d\phi/dx$, giving us $k_x = \alpha t$. Since k_x is related to the transverse scale length of the wave, we find $L_x = (\alpha t)^{-1}$. It follows from the same argument that for a sufficiently smooth transverse variation of resonant frequency, the transverse scale size is given by

$$L_\perp = \frac{1}{|\nabla_\perp \omega_R| \, t} \tag{6.2}$$

Thus, in the presence of a spatially variable resonant frequency, we expect that increasingly small transverse scales should be generated as a function of time. For a cavity mode oscillation on an $L = 10$ field line with ionospheric conductance $\tilde{\Sigma}_P = 5$, Alfvén speed $V_I = 700$ km, and scale height $H = 500km$, the phase mixing length for the fundamental mode is is $L_\perp \approx 8R_E/t$ (where t is in seconds), while for the first harmonic it is $L_\perp \approx 5R_E/t$, and the second harmonic is $L_\perp \approx 3R_E/t$. Since the damping rate of the harmonics is smaller than that of the fundamental, this indicates that cavity mode harmonics should be more effective for generating spatial scales through phase mixing, with the harmonic losing less power to dissipation and/or leakage over the same duration.

Relationship Between Frequency and Spatial Scale

Waveguide modes are dependent upon a combination of frequency and spatial scale. Thus, only frequencies with a certain spectrum of transverse scale sizes will have resonances in the neighborhood of any given frequency. We saw in Chapter 4 that the frequency and perpendicular scale size were inversely proportional, with numerical results suggesting that the lowest waveguide frequency is set by the geometry of the atmosphere-ionosphere-magnetosphere system while the upper frequency is determined by the transverse wave number, with $\omega \propto k_\perp V_I$.

Let us consider a single fundamental eigenfrequency ω_k^0. This mode is excited by a wave having perpendicular scale size λ and oscillation frequency ω. A wave with slightly different k will excite a different ω_k. These eigenmodes will be very similar. Thus, if a

wave has a spectrum of frequencies near ω_k and a spectrum of scale lengths near λ, the result should be an excitation of an additional frequency spectrum near ω_k. This suggests that a waveguide eigenmode should be identifiable as a spectral enhancement at multiple closely-spaced frequencies and at multiple closely-spaced spatial scales. (Contrast this with an IAR excitation, which should excite only isolated frequencies which should show up as narrow spectral peaks, as opposed to the broad peaks of waveguide excitation).

Scale Filtering by the Alfvén Speed Inhomogeneity

As a heuristic, consider the propagation of a fast mode wave with perpendicular wavenumber $k_\perp$ and frequency ω along a straight field line. If we limit ourselves the the WKB approximation, then the parallel wave number is given by $k_\parallel = \sqrt{\omega^2/V_A^2 - k_\perp^2}$. A monochromatic fast mode wave packet will be effectively filtered by the inhomogeneity, resulting in the confinement of small perpendicular scale waves to the regions of low Alfvén speed. It should therefore be expected that, once the initial signal has propagated through the system, that perpendicular scales will be distributed along the field line such that larger perpendicular scales are observable at larger radial distances while smaller perpendicular scales are confined to the region surrounding the F_2 peak (Alfvén speed minimum).

As demonstrated previously in Chapter 4, waveguide modes are effectively limited to the region below the Alfvén speed maximum (a distance of about 1 R_E, under normal circumstances). Any small-scale fast mode components of the original signal (which should be small due to the Alfvénic nature of the driving pulses) should be screened from the IAR region by the same peak which confines signals inside. As a consequence, any fast mode signals with $k_\perp > \omega/V_A^{\max}$ in the IAR region can be reasonably assumed

to have originated in the IAR, due either to ionospheric coupling via Hall currents or the effects of transverse inhomogeneity (both are observed).

In addition to confinement of signals to the region below the Alfvén speed peak, smaller scale signals generated by phase mixing processes are more effectively shielded from the ground, a consequence of the atmospheric shielding effect as discussed in Chapter 3.

6.2 Spectral Estimation of Parameters

The physics of ULF waves in the Alfvén resonator is fairly well understood, but due to relative paucity of observations, the properties of such waves are not. Single satellite observations of IAR processes cannot tell us the waves' spatial scale sizes nor their directions of propagation (though this may be inferred using minimum variance methods). The global resolution afforded to us by numerical simulation allows us to obtain reasonable estimates on the relationship between fundamental wave properties, such as frequency, scale size, and propagation velocity. In this section we will discuss the methods for obtaining estimates of these quantities.

6.2.1 Resonant Frequencies

Suppose we did not know either γ or ω_0, and were instead furnished with a discrete series of N data points sampled at points ψ_N sampled at points t_N. The most common method for estimating the oscillation frequency ω from ψ_N is using the Fast Fourier Transform[73]. However, as noted by Anderson[6], the time scale of Fourier analysis is often longer than the coherence timescale of the wave being analyzed, which may be as short as a few wave cycles. To overcome the limitations of Fourier methods, we use the

Morlet wavelet analysis techniques described by Torrence[93].

Wavelet analysis is often superior to Fourier methods in that it simultaneously evaluates a signal on multiple scales and provides good localization in both time and frequency (or, similarly, position and wave vector). Thus it becomes possible to estimate the instantaneous power spectrum of a signal across a range of frequencies without making use of windowing techniques (cf. Press et al.[73]).

In Chapter 4, we showed that a spectrum of different characteristic frequencies exist, dependent on the ionospheric conductance and transverse wavenumber. In the case of excitation by a relatively narrow-banded spectrum of frequencies, we should expect that resonances in the neighborhood of the of the excitation frequencies should be most strongly excited. In addition to providing superior localization of signals, the wavelet method allows for a finer resolution of frequencies, especially in the neighborhood of the IAR resonances.

6.2.2 Spatial Scales

Just as it is possibly to study the structure of a signal in time using the wavelet method, so too is it possible to study spatial structure via wavelets. This is complicated by the uniform distribution of points on a dipole grid, which is spatially uniform in configuration space. One way to deal with this is to interpolate the data from a uniform dipole grid to a uniform latitude grid, then perform the wavelet analysis on the interpolated signal.

A more straightforward approach is to directly analyze waveforms. Either one- or two-dimensional displays suffice for describing the large scale structure of IAR eigenmodes,

but knowledge of the structure in all three dimensions is required to properly characterize any given signal.

6.2.3 Propagation Speeds

In Chapter 4, we demonstrated two methods for determining the group velocity of waveguide modes. Unfortunately, one of these methods cannot be used in the context of a full numerical simulation. The second method - relating the transverse Poynting flux to the wave energy density, can be used. However, in Chapter 4, calculation of the group velocity by the Poynting flux method revealed a complication even monochromatic waveforms exhibit spatially varying group velocity. Accepting both methods as valid, we would propose to reconcile this discrepancy by considering the derivative of frequency result to be an average of sorts, while the Poynting flux is taken to represent the true spatial distribution.

The situation is additionally complicated by the presence of multiple Poynting flux maxima, which are present for every mode except the fundamental. We suggest that these maxima may be identified with multiple waveguides having different propagation speeds. Previous observations[42] support the notion that multiple waveguides with different propagation speeds can be simultaneously excited.

Given the questions arising from the relationship of these two methods, we propose two addition methods to determine the group velocity of IAR waveguide modes. The first of these is based on the correlation of waveforms between locations. If we consider a wave packet $\Psi(x,t)$ moving with average group speed v_g from point x_0 to point x_1, then the observations at these points should be maximally correlated with a time delay of $(x_1 - x_0)/v_g$. Application and implementation of the cross-correlation is discussed in Chapter

13 of Press[73]. Along with this correlation approach, we can estimate propagation speeds by examining space-time plots of compressional magnetic field intensity. If we plot time on the x-axis and latitude on the y-axis, then the propagation speed can be determined graphically with the slope of the propagation trace being proportional to the propagation speed according to $v_g = R_E \times \Delta y/\Delta x$.

6.3 IAR Excitation and Inhomogeneity Effects

In Chapters 3 and 4, we discussed the physics of wave interaction in the ionosphere and the eigenmode structure of signals that can exist in the Alfvén resonator. We have discussed the possibility of introducing additional spatial scales by inhomogeneity and phase mixing effects, but this development cannot be well studied using eigenmode methods such as DIME[2] or the reflection method for power spectra. Time domain simulation, on the other hand, allows us to understand not only the temporal development of the signals but also the effects of transverse inhomogeneity, which have been considered only in the WKB limit up to this point.

Previous work by authors such as Glassmeier[26] and Waters[97] have demonstrated that inhomogeneous ionospheric conductance can significantly affect the structure of signals both above and below the ionosphere. However, these authors have considered primarily Pc3-5 frequency signals which are unlikely to have significant interaction with the Alfvén resonator. In this section, we will study the development of signals in the Pc1/Pi1 frequency range with a realistically inhomogeneous ionospheric conductance profile. These results will then be compared to the case of uniform ionospheric conductance.

[2] Although it is possible to obtain quantitative results by analyzing the spatial variations of eigenfrequencies.

6.3.1 Ionospheric Conductance Model

Hurtaud[35] provided expressions from an earlier study by Senior et al. which we will use to establish our conductance profiles. Using three years of data from the EISCAT[3] radar array, Senior derived the following empirical expressions for the Pedersen and Hall conductance as a function of solar azimuth angle, χ

$$\Sigma_P = 1.81 + 8.88\cos\chi \quad \Sigma_H = 21.58 - 0.21\chi \tag{6.3}$$

The solar azimuth angle is a function of latitude, longitude, season, and local time. Further details of this model and its parameters can be found in Appendix D. Profiles of the conductance as a function of L-shell and longitude are shown in Figure 6.1.

The primary source of inhomogeneity in this conductance model is the non-uniform solar illumination of the Earth's ionosphere. As mentioned in Chapter 1, one primary source for ionospheric plasmas is photoionization by solar UV radiation. As a consequence, the nightside ($18 < \mathrm{LT} < 6$) is much more weakly conducting in this model than the dayside. Note that the conductance profiles in this model are symmetric with respect to the noon-midnight meridian, so if we wish to study the effects of non-symmetric inhomogeneities it is necessary drive the system at a local time other than 0 or 12.

6.3.2 Run Descriptions

For all runs, an constant Pedersen/Hall conductance ratio of 5 is assumed, regardless of inhomogeneity. The purpose of this is to facilitate comparison with the eigenmode

[3]European Incoherent SCATter

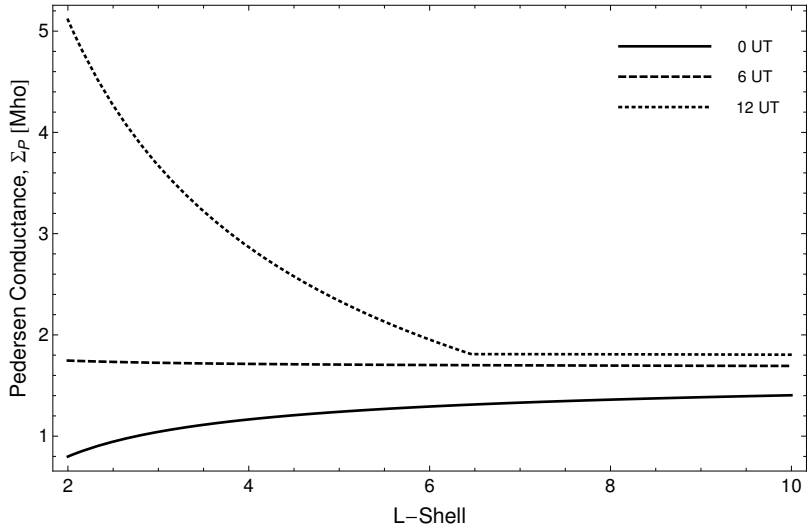

(a) L-Shell Profile

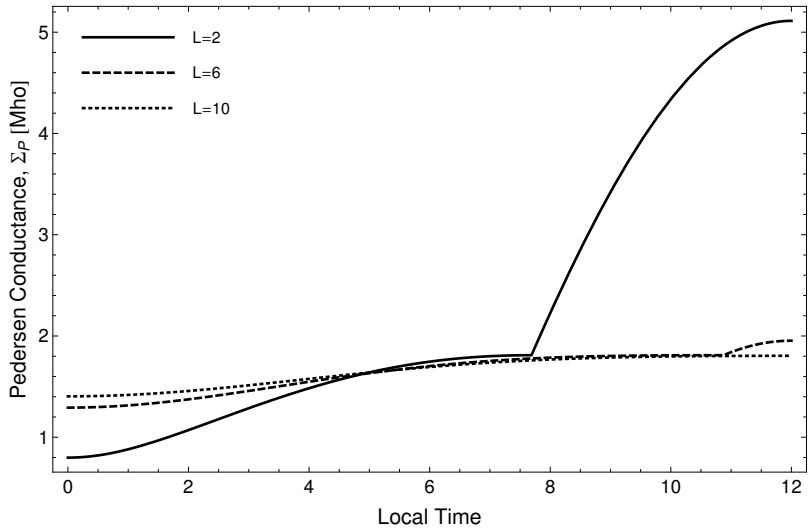

(b) Longitudinal Profile

Figure 6.1: Pedersen conductance profiles. (A) As a function of L-shell. Notice that the conductance near 0 LT is always small, while a large variation exists at 12 LT which depends on L-Shell. (B) As a function of local time. Abrupt changes in the profile behavior of the profile are associated with the day/night terminator region, which occurs at different local times for different L-shells.

analysis of Chapter 4, which assumed that Hall effects could be neglected (which is not the case if $\tilde{\Sigma}_H \geq \tilde{\Sigma}_P$).

Driver Description

An Alfvén wave is introduced into the system by specifying $\mathbf{E} = -\nabla\Phi$ on the outer boundary. The amplitude of the signal is given by

$$\Phi(L, \phi, t) = e^{-t/\tau} \sin(2\pi t/\tau)\, e^{-\left(\frac{L-L_0}{\Delta L}\right)^2 - \left(\frac{\phi-\phi_0}{\Delta\phi}\right)^2} \tag{6.4}$$

The parameters are chosen to be $L_0 = 6$, $\Delta L = 1$, $\phi_0 = 180°$, and $\Delta\phi = 10°$. The characteristic time of the driver,τ, is set at 3s.

Note that although this signal has a pure oscillation frequency ($f = 1/\tau$), the input power spectrum is not purely monochromatic, but is rather a distribution with a strong peak near $1/\tau$. The peakedness and distribution of the frequencies arises from the assumption that the signal vanishes for $t < 0$. The general form of our driving signal's time behavior is

$$f(t) = e^{-\nu t} \sin(\omega_0 t)\Theta(t) \tag{6.5}$$

Where $\Theta(t)$ is the Heaviside theta function[4], and $\nu = 1/\tau$. The power spectrum of this signal is

[4]Defined to be zero for negative arguments and one for positive arguments

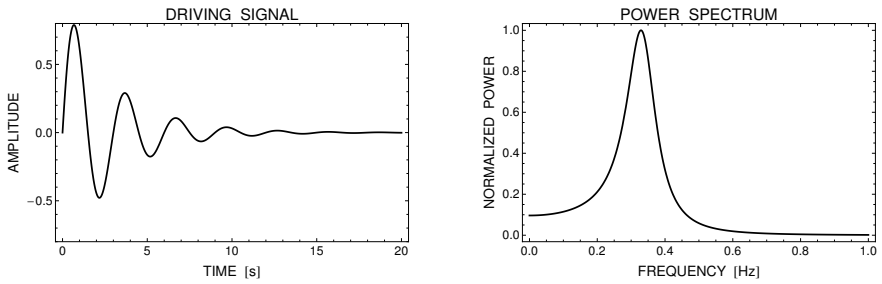

Figure 6.2: $\tau = 1$ input signal and associated power spectrum. Notice the strong peak in the power spectrum near 0.33 Hz, along with the asymmetric falloff favoring power at lower frequencies.

$$P(\omega) = \frac{1}{\sqrt{2\pi}} \frac{\omega_0^2}{(\omega^2 - (\omega_0^2 - \nu^2))^2 + 4\nu^2\omega_0^2} \tag{6.6}$$

The driving signal (6.5) and its power spectrum (6.6) are shown in Figure 6.2.

The 3s driving signal and its associated power spectrum are shown in Figure 6.2.

The maximum power occurs at $\omega = \sqrt{\omega_0^2 - \nu^2} = 0.329$ Hz and the peak has a full width at half maximum (FWHM) given by $FWHM = (\sqrt{\omega_0^2 - \nu^2 + 2\nu\omega_0} - \sqrt{\omega_0^2 - \nu^2 - 2\nu\omega_0})/2\pi$, which is about 0.109 Hz. As seen in Figure 4.8, only one IAR cavity mode is expected to exist in the range of excitation from this driver, with the possibility of two distinct waveguide modes (one at shorter wavelengths corresponding to a lower waveguide harmonic and one at longer wavelengths corresponding to a higher harmonic). Because of the asymmetry of the spectral shape, there may be enough power at lower frequencies to excite a fundamental cavity mode, but such excitation should be relatively weak.

Magnetospheric Parameters

An identical magnetospheric plasma model is used for each run, a two-species Chapman model which represents the ionosphere as a Chapman layer at $400km$ and the magnetosphere as a power-law of hydrogen. In order to remove phase-mixing effects from the plasmapause boundary, we use the same profile at all latitudes,

$$n(r) = n_O e^{1-z-e^{-z}} + n_H r^{-\gamma} \tag{6.7}$$

Where $z = (r - r_{F2})/H$ is the normalized distance from the F_2 density peak, $r_{F2} = 300$ km, $H = 500$ km is the ionospheric scale height, $\gamma = -1$ is the Hydrogen power law index, $n_H = 1000$ cm^{-3}, and n_O is chosen such that the Alfvén speed at the F_2 peak is 700 km/s. A plot of the Alfvén speed profile used in our simulation runs is shown in Figure 6.3.

6.4 Uniform Conductance with 0.33 Hz Oscillation

6.4.1 Temporal Response and Harmonic Structure

The strongest excitation is a first harmonic Alfvén resonator cavity mode, as evidenced by the E_2 waveforms shown in Figure 6.4 The power spectrum (Figure 6.5(a)) is also consistent with this observation, as the signal at 15000 km (close to the outer boundary) is characterized by a persistent narrow-band signal, which must be representative of an Alfvénic signal, owing to the filtering of compressional power by the Alfvén peak (as evidence by the lack of compressional power at at same location). There is evidence

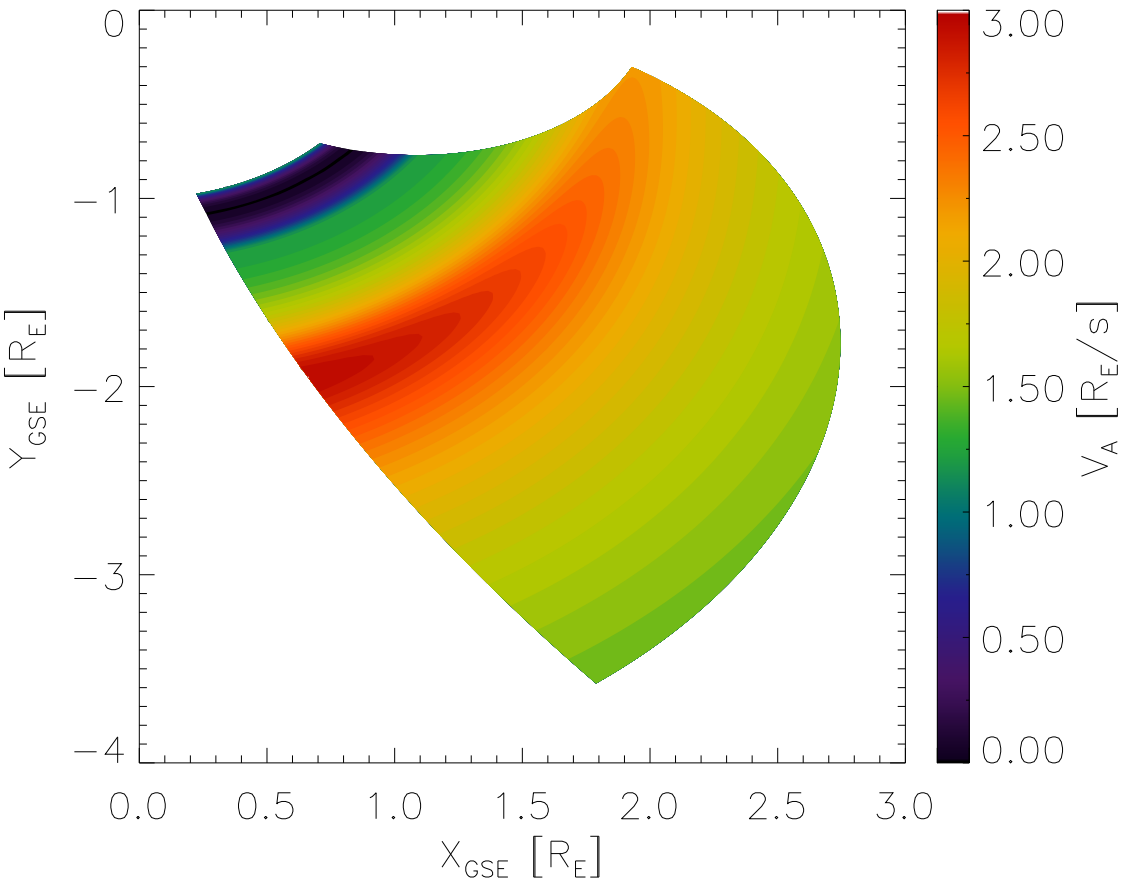

Figure 6.3: Meridional profile of Alfvén speed profile used in all runs. Since Alfvén speed is independent of azimuthal coordinate, the same profile applies at all longitudes. The Alfvén speed maximum occurs at a height of about 1 R_E, but the speed has increased by over a factor of 10 within a few tenths of an R_E. The effective height of the IAR within this cavity is not well determined, owing largely to dearth of relevant observations.

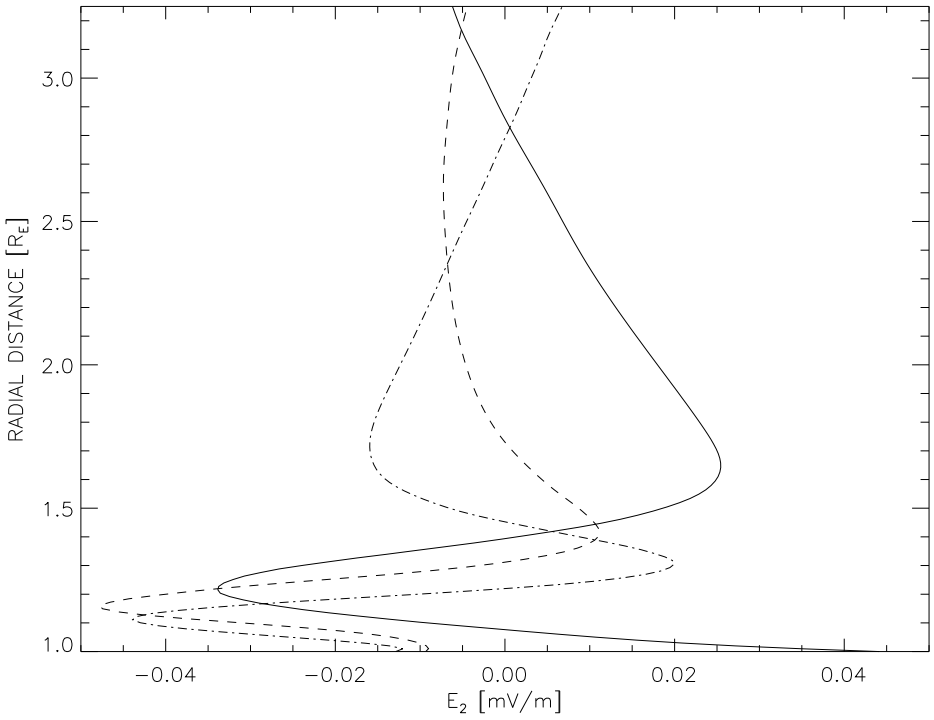

Figure 6.4: Waveforms of azimuthal electric at different latitudes, 77° away from the injection center. Solid: -68° latitude, Dashed: -73° latitude, Dot-Dashed: -63° latitude.

of a possible fundamental cavity mode in the spectrum at 1000 km, but it weaker by nearly two orders of magnitude.

In addition to the cavity modes, a relatively weak waveguide mode signal observed. We presume this is generated by the combined action of the ionospheric Hall currents and phase mixing processes, although results from other runs (not shown) lead us to believe that the dominant source is actually phase mixing due to plasma and/or ionospheric inhomogeneity. Hall effects are responsible for the strong signal at the ionospheric boundary, however, which is an evanescent surface mode which draws power from Hall

coupling to the cavity mode. The presence of this waveguide mode is evidenced by a persistent signal near 3s in the B_3 power spectrum (Figure 6.5(b)) and the vertical structure of the waveform (the solid line in Figure 6.13(a)) which maximizes near the Alfvén speed minimum (about 640 km).

Also interesting is the temporal development of power in B_3 at 1000 km, which appears to be coincident with the decrease in E_2 power at that altitude. This may be related to the exponential decrease in the driving signal amplitude since the exponentially decreasing signal essentially vanishes at t = 15s, and coupled with the (approximately) 5s propagation time from the outer boundary to the ionosphere, t = 20s corresponds to the point at which the system transitions from driven to undriven. From Figure 6.4, we see that 1000 km is between successive peaks in E_2, located rather near a node - hence, the absence of power in E_2 at this location. The increase in B_3 power can be attributed to the generation of propagating waveguide modes, which may originate at either higher or lower altitudes but propagate meridionally through the observation point. That the power in B_3 is greater at lower altitudes is likely related to the previously mentioned wavenumber filtering effect, with shorter wavelength signals being confined below 1000 km.

6.4.2 Fields on the Ground

One of the key capabilities of our simulation method is the ability to obtain magnetic fields below the ionosphere. Ideally, these fields can be used for studying the apparent propagation of signals as a function of both space and time. As mentioned in Chapter 3, Pc1 pulsations are often observed at multiple ground-based magnetic observatories without any clear indication of their origin. With the information provided by our simulations, it is possible to correlate observations on the ground directly with the

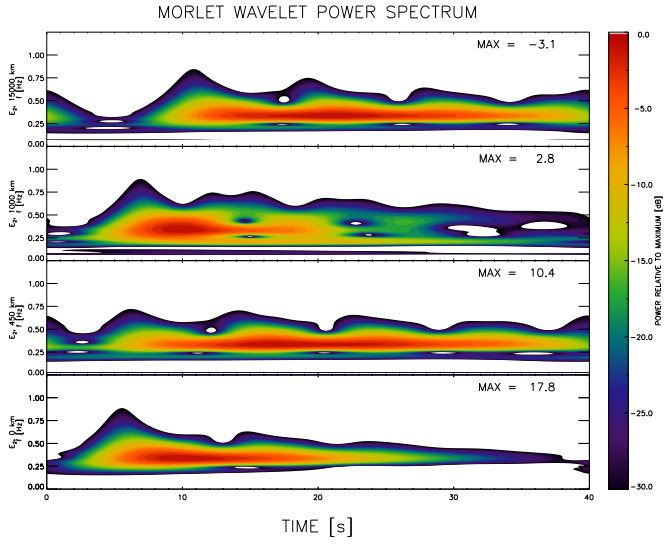

(a) E_2 Spectrum, Uniform Ionosphere

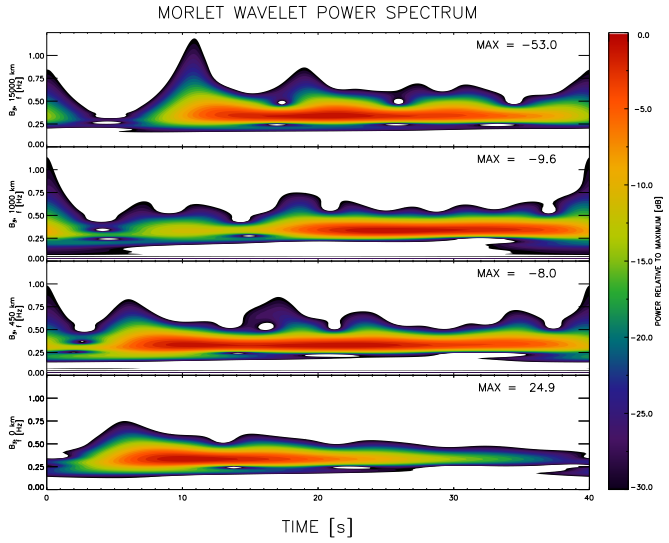

(b) B_3 Spectrum, Uniform Ionosphere

Figure 6.5: Power spectra of E_2 and B_3 fields. (A) E_2. (B) B_3. Individual panels display spectra from different altitudes. From bottom: 0 km (Ionosphere), 450 km (Below Alfvén minimum), 1000 km (Above Alfvén minimum), 15000 km (Near outer boundary).

known characteristics of the source without needing to make use of polarization or time-of-flight analysis.[5]

In Figure 6.6, we show the azimuthal magnetic fields on the ground just after the driving signal has reached the ionosphere. There are two different signals observable, a large-amplitude oscillation associated with the incident FAC and a small amplitude, phase-lagged wave which presumably corresponds to a transversely propagating waveguide mode.

In Figure 6.7, we show the power spectra for both B_θ and B_ϕ at two locations. Although both components are excited in the neighborhood of the injection center, the power in B_ϕ is only a tenth of that in B_θ. However, nearly 2000 km away, the azimuthal field is

6.4.3 Propagation and Damping

For the driver parameters used in this run, it is difficult to determine a reliable value for the azimuthal propagation of waveguide modes owing to a rapid azimuthal expansion of the driving signal in the region just below the Alfvén speed peak. Both methods for determining azimuthal propagation speed indicate velocities on the order of 3000-4000 km/s, which is physically possible (being on the order of the Alfvén speed slightly below the peak at 1 R_E), but may not necessarily be physically real. It may be that this apparent motion is due to dispersive broadening of the downgoing wavepacket at and above the Alfvén speed peak. This possibility is suggested by Figure 6.8, where apparent azimuthal expansion of the signal occurs before the signal ever reaches the ionosphere. It may be easier for the signal to disperse azimuthally since the plasma is uniform in this direction, although some latitudinal expansion of the downgoing wavepacket is observed.

[5]However, the application of these analyses to simulation data may someday make for an interesting study.

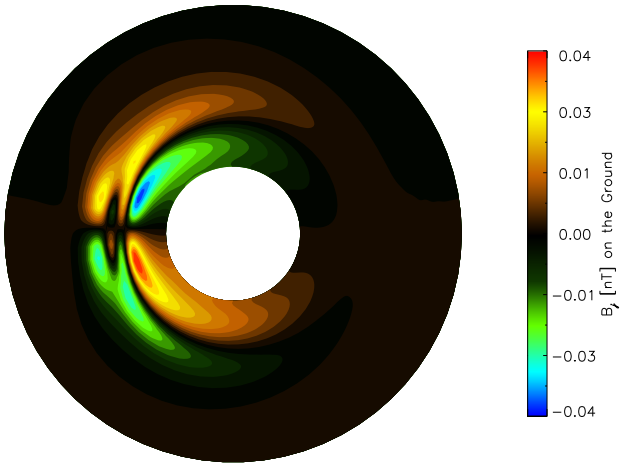

(a) B_ϕ, t=7s, uniform ionosphere

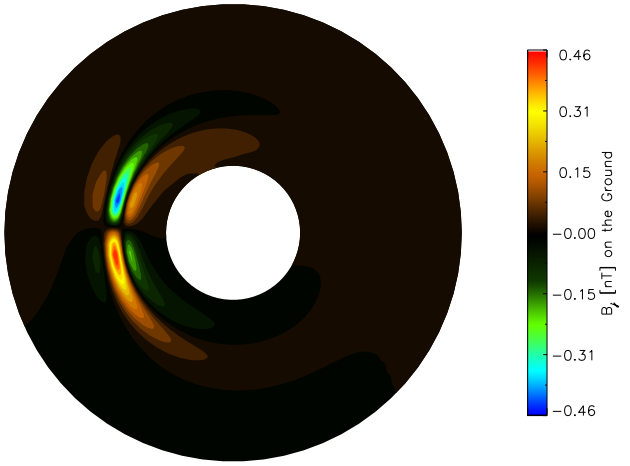

(b) B_ϕ, t=7.8s, uniform ionosphere

Figure 6.6: Azimuthal magnetic fields on the ground. (A) t=7s (B) t=7.8s. Since the period of this oscillation is about 3s, this represents a difference of one quarter period such that the strong signal in (B) is at a minimum in (A), revealing that a small amplitude wave has expanded to a much greater longitudinal and latitudinal extent than the larger one.

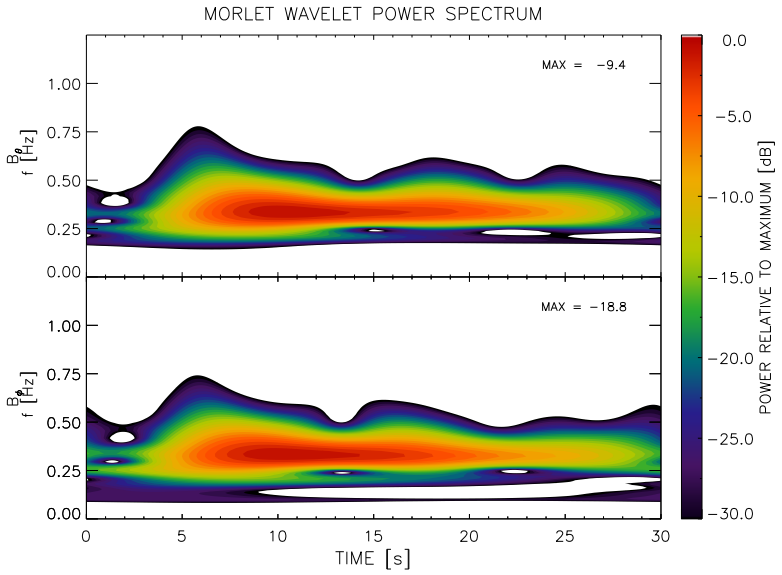

(a) Power Spectra of Perpendicular Fields on the Ground, Near Center

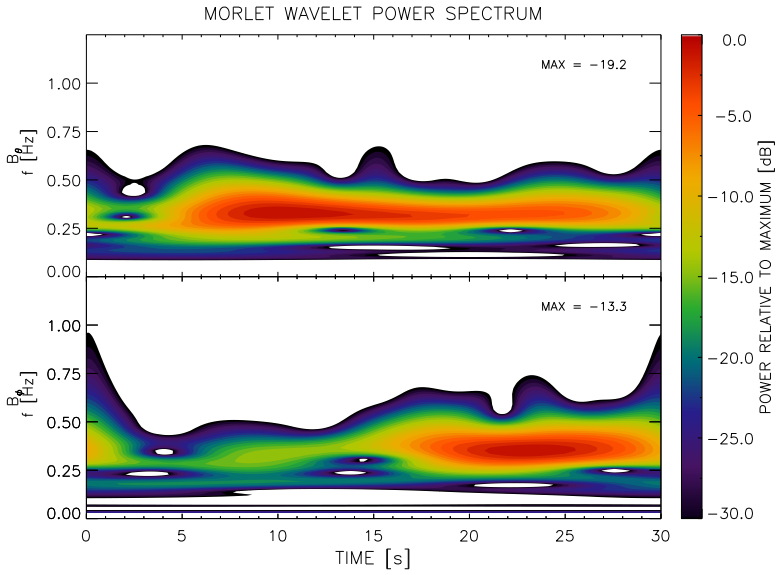

(b) Power Spectra of Perpendicular Fields on the Ground, Away From Center

Figure 6.7: Power spectra of B_θ and B_ϕ fields at L = 4. (A) Below injection center (B) 77° away from injection center.

This wavepacket expansion is very evident in the ground signal (Figure 6.6). Moreover, once the incident signal has begun to interact in the lower Alfvén resonator, a smaller-amplitude waveguide signal propagates even further, being observable a few thousand kilometers beyond the injection center (Figure 6.7). However, the strongest signal is still directly below the injection center, so the ground fields are unambiguous as to the location of the injection center.

We calculate the meridional group velocity of the waveguide mode (as determined from magnetospheric Poynting flux data) to be 750±50 km/s in the waveguide region between 400 and 1000 km and 1200±100 km/s in the waveguide between 2000 and 3000 km. This is consistent with the idea of Chapter 4 that waveguide modes should propagate at different speeds depending on altitude and the characteristics of the particular mode being considered, and that the velocity increases with the local Alfvén speed. These velocities are themselves consistent with the space-time plots of meridional Poynting flux shown in Figure 6.9.

As signals propagate in the waveguide, they are damped by a combination of effects: ionospheric energy dissipation, mode conversion, phase mixing, and (at long wavelengths) leakage to the magnetosphere. In Figure 6.10, we show waveforms of the ground magnetic fields at different spatial locations. Based on the amplitudes and positions relative to the known injection center, we can infer a meridional damping rate between 20 and 35 dB per 1000 km. The signals are more weakly damped azimuthally, with an apparent decrease of 5 db per 1000 km. This is likely due to the fact that azimuthal propagation does not require the wave to cross any transverse gradients in the background plasma, thus mitigating the associated effects of wave dispersion and mode coupling.

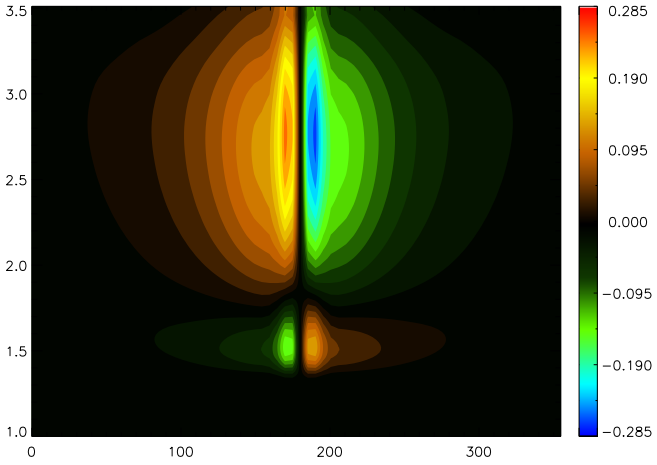

(a) E_2 azimuthal profile, t=2.5s, uniform ionosphere

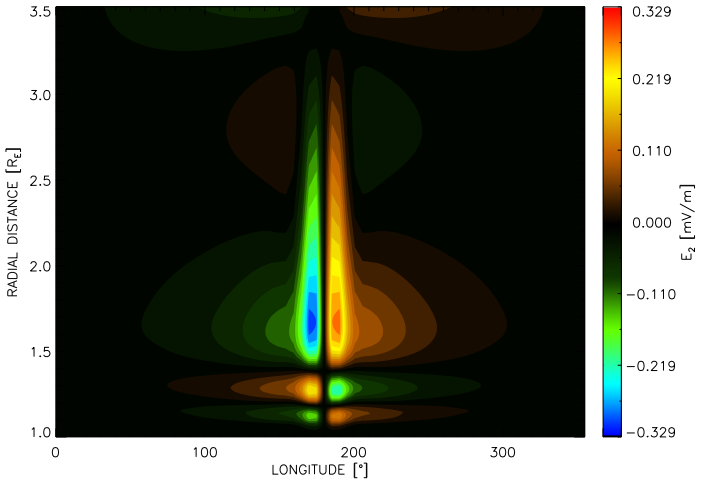

(b) E_2 azimuthal profile, t=5s, uniform ionosphere.

Figure 6.8: Azimuthal profile of downward propagating azimuthal electric field. (A) At t=2.5 s. (B) At t=5s. The original latitudinal extent is represented by the pair of enhancements along the field lines on either side of the node at 180°, but outward propagation of the signal in the upper IAR and the downward propagation of the signal is evidenced by "bulging" above the Alfvén peak and near 1.7, 1.3, and 1.1 R_E below the Alfvén peak (note that the wave has not yet reached the ionosphere by this time, so this is purely due to inhomogeneity and geometrical effects).

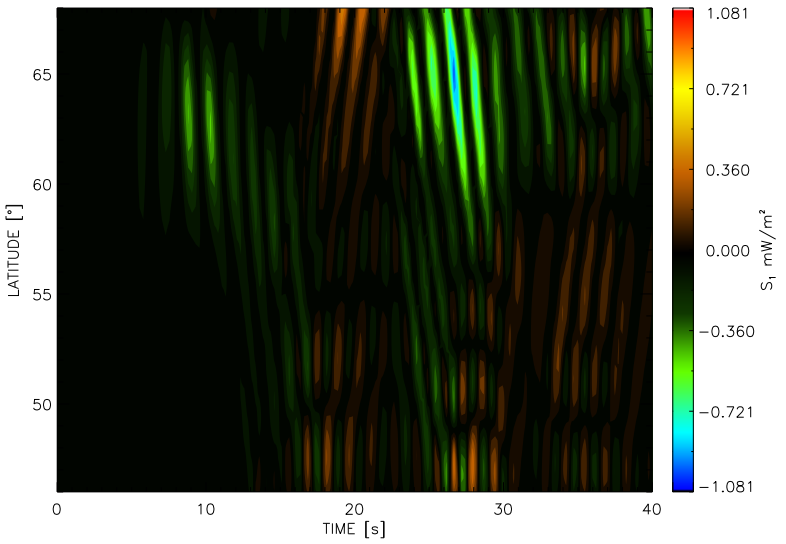

(a) Meridional Poytning flux at 1000 km.

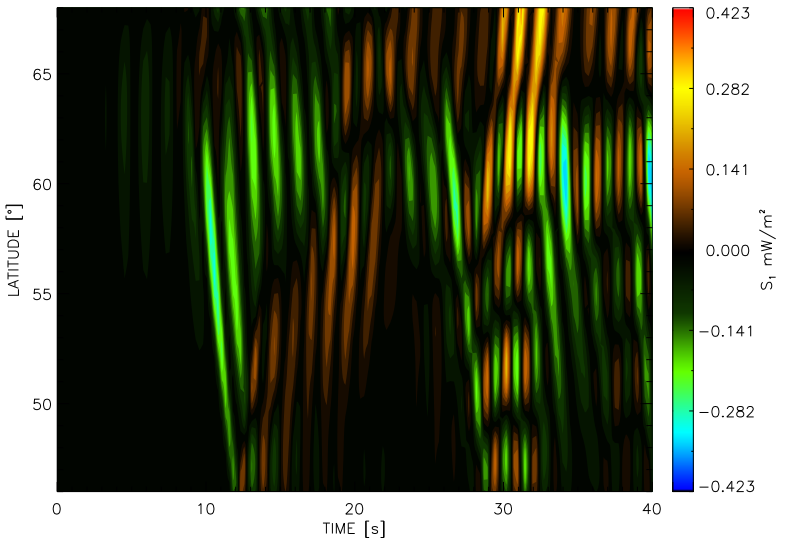

(b) Meridional Poynting flux at 2000 km.

Figure 6.9: Space-time plots of meridional Poynting flux. (A) At 1000 km. (B) At 2000 km. The slope of the waveform is proportional to the propagation speed of the wave.

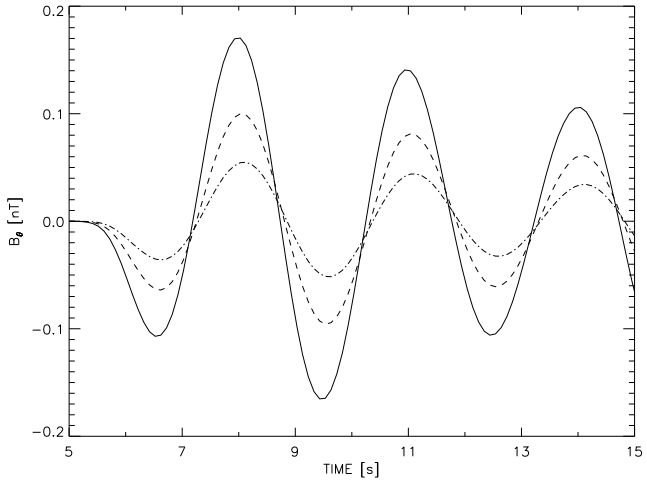

(a) Ground meridional fields (B_θ) at different longitudes.

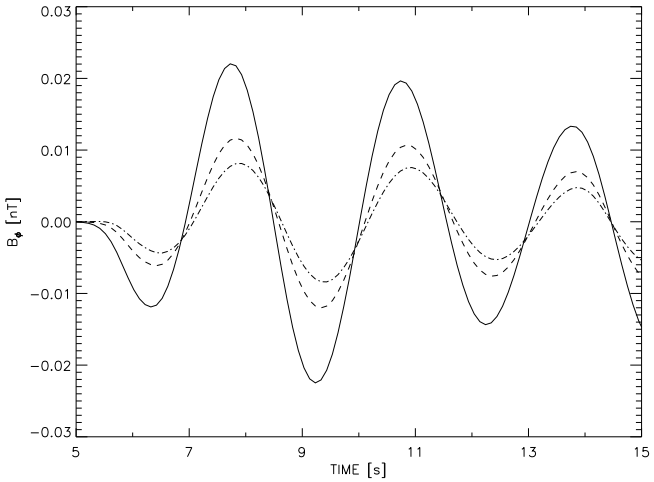

(b) Ground azimuthal fields (B_ϕ) at different latitudes.

Figure 6.10: Ground magnetic field waveforms. (A) Meridional field at different longitudes. Solid: 154°, Dashed: 129°, Dash-Dotted: 103°. Due to the Hughes effect, the ground meridional field corresponds to the azimuthal field in space, associated with azimuthal propagation in the waveguide. (B) Azimuthal field at different latitudes. Solid: -58°, Dashed: -56°, Dash-Dotted: -54°. The associated magnetospheric magnetic field is meridional, as is the Poynting flux.

6.5 Non-Uniform Conductance with 0.33 Hz Oscillation

In contrast to the run previously discussed, here we make use of the empirical conductance models defined in Equation (6.3). The Pedersen conductance[6] is shown in Figure 6.11. Note that the conductance varies by nearly a factor of 20 from midnight to noon, going from $\tilde{\Sigma}_P \ll 1$ to $\tilde{\Sigma}_P \gg 1$.

6.5.1 General Characteristics

The most striking difference between the uniform and non-uniform ionosphere simulations is the rapid damping of the IAR cavity mode. Figure 6.12 shows a comparison between the azimuthal electric field at the same timestep (t=30s) for a uniform ionosphere and dayside driving with a non-uniform ionosphere. Accounting for the 5s propagation time of the signal from outer boundary to the ionosphere, Figure 6.12 indicates the strong cavity mode of Figure 6.12(a) is damped by a factor of 10 over the course of 25 seconds ($\gamma \sim 0.09$, comparable to the strongest damping rate possible in the uniform ionosphere case of Chapter 4).[7]

Although we can unambiguously detect the presence of both a cavity and waveguide mode in Figure 6.12(b), it is not at all apparent that such a signal would be easily detectable in the presence of a noisy background. This rapid damping may account for the relative difficulty of directly detecting cavity modes from spikes in power spectra[30], but the apparent persistence of small amplitude signatures still allows for polarization properties to be used, as in [30] and [100].

[6] And essentially also the Hall conductance, since $\Sigma_P/\Sigma_H = 5$ everywhere

[7] This is not just due to a phase shift, both plots are shown near amplitude maximum.

Figure 6.11: Empirical profile of Ionospheric Pedersen conductance. Outer boundary represents the footprint of an L=2 field line while the inner boundary is the footprint of an L=20 field line. The configuration as shown corresponds to a dayside driver; rotation by 90° and 180° result in the dawn and nightside driver cases, respectively. Conductance gradients are much stronger on the dayside and at the terminators, so increased phase mixing due to inhomogeneity effects should be expected in these regions.

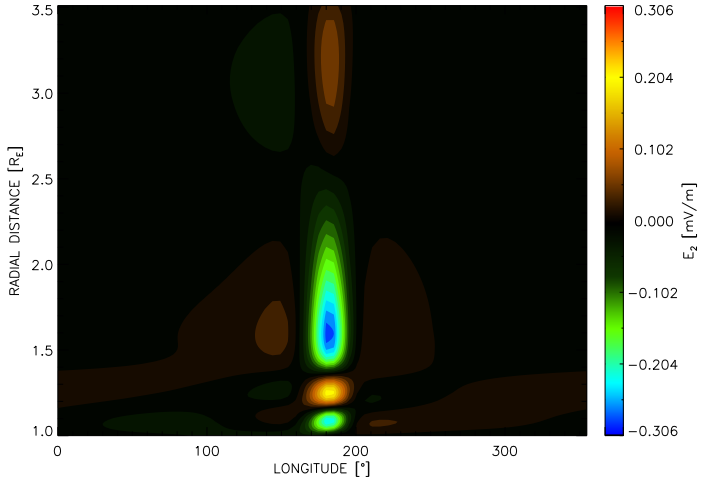

(a) E_2 azimuthal profile, t=30s, uniform ionosphere

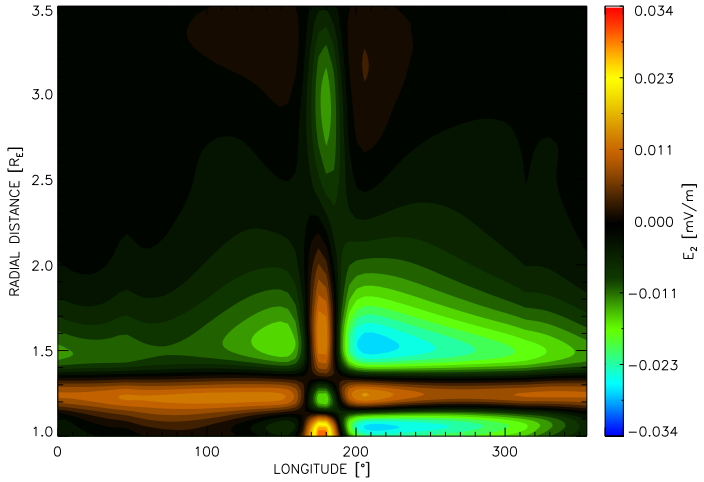

(b) E_2 azimuthal profile, t=30s, non-uniform ionosphere.

Figure 6.12: IAR cavity mode damping by phase mixing effects. (A) E_2 at t=30s, uniform ionosphere. (B) E_2 at t=30s, non-uniform ionosphere (dayside driver). The smaller amplitude signals in (B) are also present in (A), but not visible due to the first harmonic IAR mode being so much stronger in the uniform case. An m=1 (azimuthal wavenumber) waveguide mode is apparent in (B). Weaker but relatively strong damping occurs for the nightside and dawn drivers (not shown).

6.5.2 Comparison of Different Profiles

As mentioned above, the presence of strong inhomogeneities in the ionospheric conductance can result in the rapid damping of IAR cavity modes. Ionospheric inhomogeneities have the opposite effect on the waveguide modes, however, as the resultant phase mixing results in the production of smaller scale structure which can be efficiently trapped and propagated in the Alfvén resonator. As noted in Chapter 4, the frequency and mode structure of the compressional waves are reasonably insensitive to variations in the ionospheric conductance. For example, in Figure 6.13(a), we show the vertical profile of the mangetic field on the same field line, at the essentially the same point in time,[8] for four different arrangements of ionosphere and driver: uniform ionosphere, dayside driver, dawn driver, and nightside driver. In each case, a first harmonic waveguide mode has been excited; additional waveforms at different latitudes and longitudes show that this n=1 mode is established throughout the waveguide regardless of the conductance profile.

Although the structure above the ionosphere does not exhibit a great deal of variation, inhomogeneous conductance does have a marked effect on the development of signals on the ground. In Figure 6.13(b), we show ground fields are enhanced by inhomogeneities in the ionospheric conductance. In each case, the waveguide modes are temporarily enhanced following the termination of the driving signal before decreasing to pre-enhancement levels. This decrease is due to a combination of mode coupling and phase mixing effects in the waveguide fields.

[8]Because the waves vary in phase, the maximum closest to t = 30s was chosen.

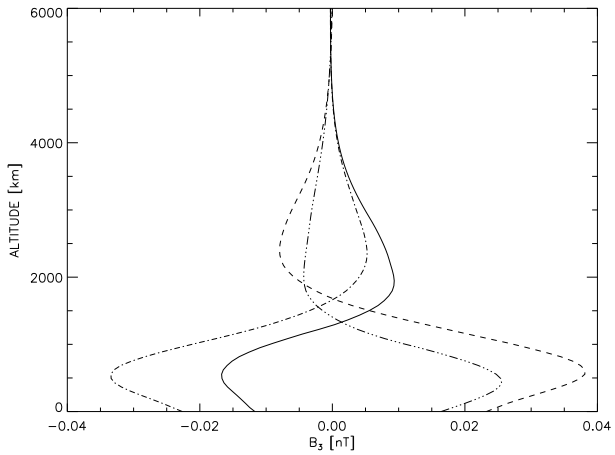

(a) B_3 waveforms on L=4 field line.

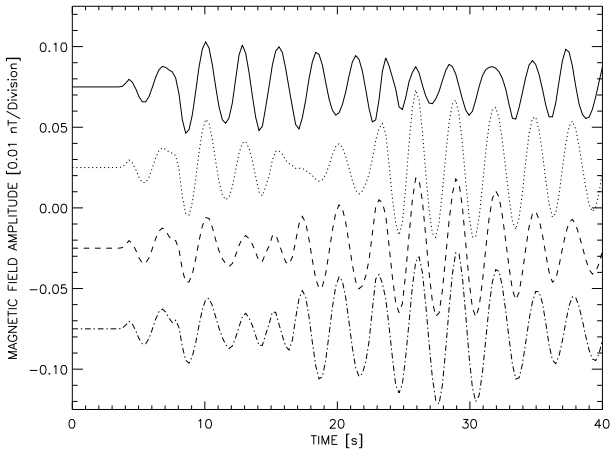

(b) B_ϕ time series for different ionospheric conditions.

Figure 6.13: (A) Compressional magnetic field profiles along an L=3.6 field line, 77° from injection center. Note that the primary maximum occurs near 600 km and a secondary maximum occurs near 2000 km. These very nearly the same maxima of E_2 seen in Figure 6.12(b) where we identified the presence of an m=1 azimuthal waveguide mode. Solid: uniform ionosphere, Dashed: dayside driver, Dot-Dashed: dawn driver, Dot-dot-dot-dashed: nightside driver. (B) Azimuthal magnetic field (B_ϕ) at -60◦ latitude and 102° longitude. Solid: uniform ionosphere, Dotted: nighside driver, Dashed: dawn driver, Dot-dashed: dayside driver. For inhomogeneous profiles, the field increases after t=20s, while the fields remain essentially constant for the uniform case.

6.6 Discussion

In this chapter, we have used results from a simulation of magnetospheric wave propagation using a realistic ionospheric conductance profile to study the excitation of the Alfvén resonator by an FAC impulse. Although we might have expected the frequency of the IAR cavity modes to vary greatly depending on the ionospheric conductance (as was found in Chapter 4), this was found to be the case. This is likely due to a variety of effects, the most important of which might be the effective conductance of the ionosphere arising due to the imperfect shielding effect (see Chapter 3).

One simplifying assumptions of the DIME method is wave propagation in only one direction, or equivalently, uniformity in one direction. Under this assumption, the Alfvén resonator equations conveniently decouple and we find that the cavity mode generates no fields below the ionosphere, i.e. the ionosphere perfectly shields the ground. However, in the presence of a localized FAC, the resonator equations do not decouple and the fields associated with the FAC are partially transmitted to the ground. This increases the effective conductance of the ionosphere, thus changing the dependence of the cavity mode frequency on the ionospheric Pedersen conductance.

When the ionosphere is spatially inhomogeneous, we found that the cavity mode is subject to strong damping while the waveguide mode is (at least temporarily) enhanced. This appears to be due to phase mixing-type effects occuring on the inhomogeneity scale of the ionospheric conductance profile. Because the dayside profile is much more strongly inhomogeneous, we find that the cavity mode should be more persistent on the night side than on the day side, but in either case the damping due to the inhomogeneity should result in a rapid reduction in undriven cavity mode amplitude. Given that waveguide mode power is observed to increase at the same time as the cavity mode power decreases,

we are lead to think that at least part of this loss is due to enhanced coupling between IAR eigenmodes.

Chapter 7

Conclusions

The physics of ULF waves is a long-standing area of research in Space Plasma Physics. As we have demonstrated in this thesis, even simplified theoretical models produce complicated results which themselves require sophisticated analysis techniques to fully understand. In the course of our studies, we have endeavored to develop our methods of numerical analysis and computer simulation as logical extensions of a unified physical framework.

7.1 What We Have Done

This thesis began with a brief review of certain relevant topics in magnetospheric physics, and then provided a theoretical development of the mathematical formalism needed for the study of waves in plasmas. We then considered the interaction of ultra-low frequency plasma waves with the Earth's ionosphere and their relation to magnetic pulsation phenomena.

Having introduced the Alfvén resonator and suggested its role in the structuring of pulsations, we developed the "Downward Integration Method", a numerical approach for determining properties of the Alfvén resonator applicable to both cavity and waveguide modes. We examined the parametric dependences implied by these models and suggested how results might be useful in the interpretation of certain observations.

Finally, we simulated the excitation of the Alfvén resonator excitation by localized field-aligned current impulses in the presence of a realistic ionospheric conductance profile. Using the results of these simulations, we have found that the frequency and harmonic response is rather well predicted by the high-conductance predictions from DIME. The cavity modes are observed to be strongly damped in the presence of inhomogeneous profile, while the spectral power of the waveguide modes is somewhat enhanced. We also find that the frequency response of the cavity mode to variations in the Pedersen conductance is greatly reduced owing to the imperfect shielding of magnetospheric fields by the ionosphere and subsequent transmission of fields to the ground.

As much as we have done to this point, there is much that our work has not yet explained, or even examined. This should not be seen as a discouraging, however, since it was not our goal to answer every question but, rather, to develop methods by which questions can be answered. Building upon the work of this thesis, there are numerous questions regarding the propagation, coupling, and observation of waves and their structure that can be readily answered. Moreover, the methods which we have used can be extended beyond the scope seen in this work, clearing the way for further investigation of additional problems.

7.2 Future Work

The Downward Integration Method developed in Chapter 4 is much more versatile than its application in this paper. Previous work in Cartesian coordinates by Greifinger[28],[29] included various models of ionospheric Hall and Pedersen conductivity, and full-wave model in pseudodipole coordinates by Lysak[47] made use of a multiple Chapman profile ionosphere model. It is possible to use any arbitrary model for plasma parameters - and, in fact, any arbitrary set of coordinates. The choice of orthogonal dipole coordinates and our particular Alfvén speed profile was motivated by a desire to validate results via comparison to the simulation results of Chapter 6.

Ground observations of magnetic pulsations are frequently available when spacecraft are not. The Alfvén resonator region, on which we focused our study, is naturally coupled to the ground by ionospheric currents, as discussed in Chapter 3. Although we examined ground signatures to some extent in Chapter 6, there is much more that can be done, for example studying the propagation of signals across a virtual magnetometer chain with dimensions and spacing similar to existing chains for which there are existing observations.

The polarization state of waves is a theoretically important quantity with practical implications. As explained by Anderson[6], polarization characteristics "provide definitive tests of mechanisms for wave propagation and growth." Moreover, as demonstrated by Grzesiak[30] and Zhao[100], the cross-spectral phase relationship between electromagnetic field components can be used as an effective indicator of eigenmode excitation which can supplement power spectral methods such as those used in Chapter 6. In addition to cross-spectral methods, simpler approaches such as the hodograph technique

or minimum variance analysis (MVA) can be used to determine the transverse polarization ellipse (which reveals both ellipticity and handedness), and MVA of the magnetic field may also be used to determine the local direction of the wave vector. These approaches could augment or replace the spectral methods for determining polarization characteristics, in certain circumstances.

Although the non-orthogonal system of coordinates used in our simulation has allowed us to realistically treat the ionospheric boundary, the high- and low- latitude boundaries are still represented by Dirichlet and Neumann conditions on the fields. Physically, this corresponds to the presence of an artificial reflecting barrier at those latitudes. We discovered in the course of our analysis that meridionally ducted waveguide modes would often propagate to these boundaries and be reflected. It would be desirable to allow the waves to exit the simulation through both the high- and low- latitude boundaries, but the methodology of doing so is not straightforward. We allow for Alfén waves to leave the top of the simulation by using an impedance matching method[1], but this cannot be used for obliquely propagating magnetosonic waves. A recently developed technique known as the Perfectly Matched Layer (PML) has shown great promise for problems of this type, and we should consider its application for improving the effects of artificial boundaries on our simulation results.

[1] equivalent to an Elsaässer variable approach, as noted in Chapter 5

Bibliography

[1] M. Abramowicz and I. Stegun. *Handbook of Mathematical Functions*. Dover, 1964.

[2] S.-I. Akasofu. The development of the auroral substorm. *Planetary and Space Science*, 12:273–282, 1964.

[3] E. L. Althouse and J. R. Davis. Five-station observatiosn of pc1 micropulsation propagation. *Journal of Geophysical Research*, 83(132), 1978.

[4] C. Altman and E. Fijalkow. The horizontal propagation of pc1 pulsations in the ionosphere. *Planetary and Space Science*, 28, 1980.

[5] B. J. Anderson and D. C. Hamilton. Electromagnetic ion cyclotron waves stimulated by modest magnetospheric compressions. *Journal of Geophysical Research*, 98(A7), 1993.

[6] Denton-R. E. Anderson, B. J. and S. A. Fusilier. On determining the polarization characteristics of ion cyclotron wave magnetic field fluctuations. *Journal of Geophysical Research*, 101(A6), 1996.

[7] Erlanson-R. E. Anderson, B. J. and L. J. Zanetti. A statistical study of pc1-2 magnetic pulsations in the equatorial magnetosphere 1. equatorial occurrence distributions. *Journal of Geophysical Research*, 97(A3), 1992.

[8] G. Arfken and H. Weber. *Mathematical Methods for Physicists, 6th edition*. Academic Press, 2005.

[9] Kozlov-V. V. Arnold, V. I. and A. I. Neishtadt. *Mathematical Aspects of Classical and Celestial Mechanics*. Springer, 3 edition, 2006.

[10] Posch-J. L. Engebretson M. J. Fukunishi H. Arnoldy, R. L. and H. J. Singer. Pi1 magnetic pulsations in space and at high latitudes on the ground. *Journal of Geophysical Research*, 103(10):23581–23591, 1998.

[11] W. Baumjohann and K.-H. Glassmeier. The transient response mechanism and pi2 pulsations at substorm onset - review and outlook. *Planetary and Space Science*, 32(11), 1984.

[12] C. M. Bender and S. A. Orszag. *Advanced Mathematical Methods for Scientists and Engineers*. Springer, 1999.

[13] A. Brandenburg. Solar interior. In *Handbook of the Solar-Terrestrial Environment*, chapter 2. Springer-Verlag, 2007.

[14] Thorne-R. M. Baumjohann W. Daglis, I. A. and S. Orsini. The terrestrial ring current: Origin, formation, and decay. *Reviews of Geophysics*, 4, 1999.

[15] Trakhtengerts-V. Y. Demekhov, A. G. and T. Bosinger. Pc 1 waves and ionospheric alfvén resonator: Generation or filtration? *Geophysical Research Letters*, 27(23), 2000.

[16] M. H. Duong and B. J. Fraser. Ducted propagation of pc1 hydromagnetic waves in the upper ionosphere. *Planetary and Space Science*, 24, 1976.

[17] M. H. Duong and B. J. Fraser. Propagation of pc1 pulsations in off-meridian directions. *Planetary and Space Science*, 25, 1977.

[18] Peterson-W. K. Posch J. L. Klatt M. R. Anderson B. J. Russell C. T. Singer H. J. Arnoldy R. L. Engebretson, M. J. and H. Fukunishi. Observation of two types of pc1-2 pulsations in the outer dayside magnetosphere. *Journal of Geophysical Research*, 107(A12), 2002.

[19] B. J. Fraser. Ionospheric duct propagation and pc 1 pulsation sources. *Journal of Geophysical Research*, 80(19), 1975.

[20] B. J. Fraser and T. S. Nguyen. Is the plasmapause a preferred source region of electromagnetic ion cyclotron waves in the magnetosphere. *Journal of Atmospheric and Solar-Terrestrial Physics*, 63(11), 2001.

[21] Grew-R. S. Morley S. K. Green J. C. Singer H. J. Toto'aniu T. M. Fraser, B. J. and M. F. Thomsen. Storm time observatiosn of electromagnetic ion cyclotron waves at geosynchronous orbit: Goes results. *Journal of Geomagnetic Research*, 115, 2010.

[22] S. Fujita and T. Tamao. Duct propagation of hydromagnetic waves in the upper ionosphere 1. electromagnetic field disturbances in high latitudes associated with localized incidence of a shear alfvén wave. *Journal of Geophysical Research*, 93(A12), 1988.

[23] S. Fujita and T. Tamao. Duct propagation of hydromagnetic waves in the upper ionosphere 2. dispersion characteristics and loss mechanism. *Journal of Geophysical Research*, 93(A12), 1988.

[24] N. Fukushima. Generalized theorem for no ground magnetic effect of vertical currents connected with pedersen currents in the uniform-conductivity ionosphere. *Rep. Ionos. Space Res. Jap*, 30:35–50, 1974.

[25] Craven P. D. Gallagher, D. L. and R. H. Comfort. Global core plasma model. *Journal of Geophysical Research*, 105(A8):18819–18833, 2000.

[26] K.-H. Glassmeier. Reflection of mhd-waves in the pc4-5 period range at ionospheres with non-uniform conductivity distributions. *Geophysical Research Letters*, 10, 1983.

[27] Poole Jr. C. P. Goldstein, H. and J. L. Safko. *Classical Mechanics*. Pearson Education, 3 edition, 2000.

[28] C. Greifinger and P. Greifinger. Theory of hydromagnetic wave propagation in the ionospheric waveguide. *Journal of Geophysical Research*, 73(23):7473–7490, 1968.

[29] C. Greifinger and P. Greifinger. Wave guide propagation of micropulsations out of the plane of the geomagnetic meridian. *Journal of Geophysical Research*, 78(22):4611–4618, 1973.

[30] M. Grzesiak. Ionospheric alfven resonator as seen by freja satellite. *Geophysical Research Letters*, 27(7):923–926.

[31] A. V. Guglielmi and O. A. Pokhotelov. *Geoelectromagnetic Waves*. Institute of Physics Publishing, 1996.

[32] W. D. Hayes. Conservation of action and modal wave action. *Proceedings of the Royal Society of London A*, 320, 1970.

[33] W. J. Hughes. The effect of the atmosphere and ionosphere on long period magnetospheric micropulsations. *Planetary and Space Science*, 22, 1974.

[34] B. Hultqvist. Acceleration of ionospheric outflowing ions. *Physics and Chemistry of the Earth*, 24(1-3), 1999.

[35] Peymirat C. Hurtaud, Y. and A.D. Richmond. Modeling seasonal and diurnal effects on ionospheric conductances, region-2 currents, and plasma convection in the inner magnetosphere. *Journal of Geophysical Research*, 112:1–17, 2007.

[36] Sugiyama T. Watanabe K. Kageyama, A. and T. Sato. A note on the dipole coordinates. *Computers and Geosciences*, 32, 2006.

[37] Y. Kamide and Y. P. Maltsev. Geomagnetic storms. In *Handbook of the Solar-Terrestrial Environment*, chapter 14. Springer-Verlag, 2007.

[38] Guglielmi A. Kangas, J. and O. Pokhotelov. Morphology and physics of short-period magnetic pulsations (a review). *Space Science Reviews*, 83:435–512, 1998.

[39] H. P. Kramer. A generalized sampling theorem. *J. Math. Phys.*, 38, 1959.

[40] J. Lemaire. The 'roche-limit' of ionospheric plasma and the formation of the plasmapause. *Planetary and Space Science*, 22, 1974.

[41] Lund E. J. Jones S. L. Arnoldy R. L. Posch J. A. Engebretson M. J. Lessard, M. R. and K. Hayashi. Nature of pi1b pulsations as inferred from ground and satellite observations. *Geophysical Research Letters*, 33, 2006.

[42] R. L. Loadabrand and L. T. Dolphin Jr. Starfish prime. Technical report, Defense Atomic Support Agency, 1962.

[43] R. L. Lysak. Theory of auroral zone pib pulsation spectra. *Journal of Geophysical Research*, 93(A6), 1988.

[44] R. L. Lysak. Feedback instability of the ionospheric resonant cavity. *Journal of Geophysical Research*, 96(A2), 1991.

[45] R. L. Lysak. Generalized model of the ionospheric alfvén resonator. In Bob Lysak, editor, *Auroral Plasma Dynamics*. AGU Press, 1993.

[46] R. L. Lysak. Propagation of alfvén waves through the auroral ionosphere. *Physics and Chemistry of the Earth*, 22(7-8), 1997.

[47] R. L. Lysak. Propagation of alfvén waves through the auroral ionosphere: Dependence on ionospheric parameters. *Journal of Geophysical Research*, 104(A5), 1999.

[48] R. L. Lysak. Magnetosphere-ionosphere coupling by alfven waves at midlatitudes. *Journal of Geophysical Research*, 109, 2004.

[49] R. L. Lysak and Y. Song. A three-dimensional model of the propagation of alfvén waves through the auroral ionosphere: First results. *Advances in Space Research*, 28(5), 2001.

[50] R.L. Lysak and A. Yoshikawa. Resonant cavities and waveguides in the ionosphere and atmosphere. In Chi P. J. Denton R. E. Takahashi, K. and R. L. Lysak, editors, *Magnetospheric ULF Waves: Synthesis and New Directions*. AGU Press, 2006.

[51] I. R. Mann and A. N. Wright. Finite lifetime of ideal poloidal alfven waves. *Journal of Geophysical Research*, 100, 1995.

[52] Blomberg L. G. Fälthammar C.-G. Erlandson R. E. Marklund, G. T. and T. A. Potemra. Signatures of the high-altitude polar cusp adn dayside aurora regions as seen by the viking electric field experiment. *Journal of Geophysical Research*, 95, 1990.

[53] J. C. Maxwell. On the physical lines of force. *London, Edinburgh, and Dublin Philosophical Magazine and Journal of Science*, 4, 1861.

[54] R. L. McPherron. Growth phase of magnetospheric substorms. *Journal of Geophysical Research*, 75:5592–5599, 1970.

[55] R. L. McPherron. Magnetospheric substorms. *Reviews of Geophysics*, 17(4), 1979.

[56] R. L. McPherron. Physical processes producing magnetospheric substorms and mangetic storms. In J. A. Jacobs, editor, *Geomagnetism*, volume 4, chapter 7. Academic Press, 1991.

[57] Fraser B. J. Hansen H. J. Newell P. T. Menk, F. W. and C. I. Meng. Multistation observatiosn of pc1-2 ulf pulsations in the vicinity of the polar cusp. *Journal of Geomagnetism and Geoelectricity*, 45, 1993.

[58] Rae I.J. Mann I.R. Murphy K.R. Kale A. Russell C.T. Angelopolous V. Milling, D.K. and S. Mende. Ionospheric localisation and expansion of long-period pi1 pulsations at substorm onset. *Geophysical Research Letters*, 35(17), 2008.

[59] Rae I.J. Mann I.R. Milling D.K. Watt C.E.J. Ozeke L. Frey H.U. Angelopolous V. Murphy, K.R. and C.T. Russell. Wavelet-based ulf wave diagnosis of substorm expansion phase onset. *Journal of Geophysical Research*, 114, 2009.

[60] Braysy T. Niskala K. Mursula, K. and C.T. Russell. Pc1 pearls revisited: Structured electromagnetic ion cyclotron waves on polar satellite and on ground. *Journal of Geophysical Research*, 106(A12):29543–29553, 2001.

[61] K. Mursula. Satellite observations of pc 1 pearl waves: The changing paradigm. *Journal of Atmospheric and Solar-Terrestrial Physics*, 69, 2007.

[62] Fraser B. J. Menk F. W. Waters C. L. Burns G. B. Neudegg, D. A. and R. J. Morris. Ulf wave attenuation in the high latitude ionospheric waveguide. *Advances in Space Research*, 25(7-8), 2000.

[63] T. Obayashi. Hydromagnetic whistlers. *Journal of Geophysical Research*, 70, 1965.

[64] J. V. Olson. Pi2 pulsations and substorm onsets: A review. *Journal of Geophysical Research*, 104(A8):7999–8020, 1999.

[65] E. N. Parker. Solar wind. In *Handbook of the Solar-Terrestrial Environment*, chapter 4. Springer-Verlag, 2007.

[66] R. Penrose. A generalized inverse for matrices. *Proc. Cambridge Phil. Soc.*, 51:406–413, 1955.

[67] Mazur N. G. Fedorov E. N. Pilipenko, V. A. and M. J. Engebretson. Interaction of propagating magnetosonic and alfvén waves in a longitudinally inhomogeneous plasma. *Journal of Geophysical Research*, 113, 2008.

[68] Shalimov S. L. Fedorov E. N. Engebretson M. J. Pilipenko, V. A. and W. J. Hughes. Coupling between field-aligned current impulses and pi1 noise bursts. *Journal of Geophysical Research*, 104(A8), 1999.

[69] Khruschev I. V. Parrot M. Senchenkov S. Pokhotelov, O. A. and V. P. Pavlenko. Ionospheric alfvén resonator revisited: Feedback instability. *Journal of Geophysical Research*, 106(A11), 2001.

[70] Pokhotelov D. Streltsov A. Khruschev V. Pokhotelov, O. A. and M. Parrot. Dispersive ionospheric alfvén resonator. *Journal of Geophysical Research*, 105(A4), 2000.

[71] S.V. Polyakov. On properties of ionospheric alfven resonator. In *Symposium KAPG on Solar-Terrestrial Physics. Theses of Reports, Part III.*, pages 72–73. Nakua, 1976.

[72] Engebretson M. R. Mende S. B. Frey H. U. Arnoldy R. J. Lessard M. R. Lanzerotti L. J. Watermann J. Moldwin M. B. Posch, J. A. and P. V. Ponamarenko. Statistical observations of spatial characteristics of pi1b pulsations. *Journal of Atmospheric and Solar-Terrestrial Physics*, 69:1775–1796, 2007.

[73] Teukolsky S. A. Vetterling W. T. Press, W. H. and B. P. Flannery. *Numerical Recipes in Fortran*. Cambridge University Press, 2 edition, 1992.

[74] E. R. Priest. Solar atmosphere. In *Handbook of the Solar-Terrestrial Environment*, chapter 3. Springer-Verlag, 2007.

[75] Mursula K. Feygin F. Z. Kangas J. Kerttula R. Pikkarainen T. Pokhotelov O. A. Prikner, K. and V. Vagner. Non-stationary alfvén resonator : vertical profiles of wave characteristics. *Journal of Atmospheric and Solar-Terrestrial Physics*, 62, 2000.

[76] Mursula K. Kangas J. Kerttula R. Prikner, K. and F. Z. Feygin. An effect of the ionospheric alfvén resonator on multiband pc1 pulsations. *Annales Geophysicae*, 22, 2004.

[77] Lotko W. Kouznetsov I. Proehl, J.A. and S. D. Geimer. Ultralow-frequency magnetohydrodynamics in boundary-constrained geomagnetic flux coordinates. *Journal of Geophysical Research*, 107(A9), 2002.

[78] H. R. Radoski. A note on oscillating field lines. *Journal of Geophysical Research*, 72(1), 1967.

[79] Mann I.R. Murphy K.R. Milling D.K. Parent A. Angelopolous V. Frey H.U. Kale A. Watt C.E.J. Mende S.B. Rae, I.J. and C.T. Russell. Timing and localization of ionospheric signatures associated with substorm expansion phase onset. *Journal of Geophysical Research*, 114, 2009.

[80] G. Rostoker. Substorms. In *Handbook of the Solar-Terrestrial Environment*, chapter 15. Springer-Verlag, 2007.

[81] J. C. Samson. Geomagnetic pulsations and plasma waves in the earth's magnetosphere. In J. A. Jacobs, editor, *Geomagnetism*, volume 4, chapter 6. Academic Press, 1991.

[82] M. D. Sciffer and C. L. Waters. Propagation of ulf waves through the ionosphere: Analytic solutions for oblique magnetic fields. *Journal of Geophysical Research*, 107(A10), 2002.

[83] Waters C. L. Sciffer, M. D. and F. W. Menk. Propagation of ulf waves through the ionosphere: Inductive effect for oblique magnetic fields. *Annales Geophysicae*, 22, 2004.

[84] C. Senior. Solar and particle contributions to auroral height-integrated conductivities from eiscat data: A statistical study. *Annales Geophysicae*, 9, 1991.

[85] M. Shulz. Eigenfrequencies of geomagnetic field lines and implications for plasma-density modeling. *Journal of Geophysical Research*, 101, 1996.

[86] M. Shulz. Magnetospheres. In *Handbook of the Solar-Terrestrial Environment*, chapter 7. Springer-Verlag, 2007.

[87] D. P. Stern. A brief history of magnetospheric physics during the space age. *Reviews of Geophysics*, 34(1):1–31, 1996.

[88] B. Stewart. On the great magnetic disturbance which extended from august 28 to september 7, 1859, as recorded by photography at the kew observatory. *Phil. Trans. R. Soc.*, 151:423–430, 1861.

[89] B. Stewart. On the magnetic disturbance which took place on the 14th of december 1862. *Phil. Trans. R. Soc.*, 12:663–668, 1863.

[90] A. Taflove and S. C. Hagness. *Computational Electrodynamics: The Finite-Difference Time Domain Method*. Artech House, 2000.

[91] Ohtani S.-i. Hughes W. J. Takahashi, K. and R. R. Anderson. Crres observations of pi2 pulsations: Wave mode inside and outside the plasmasphere. *Journal of Geophysical Research*, 106(A8), 2001.

[92] B. J. Thompson and R. L. Lysak. Electron acceleration by inertial alfvén waves. *Journal of Geophysical Research*, 101(A3), 1996.

[93] C. Torrence and G. P. Campo. A practical guide to wavelet analysis. *Bulletin of the American Meteorological Society*, 79(1), 1998.

[94] C. Uberoi. Space plasmas. In *Handbook of the Solar-Terrestrial Environment*, chapter 10. Springer-Verlag, 2007.

[95] U. Villante. Ultra low frequency waves in the magnetosphere. In Y. Kamide and A. Chian, editors, *Handbook of the Solar-Terrestrial Environment*, chapter 16. Springer-Verlag, 2007.

[96] P. J. Coleman W. D. Cummings, R. J. O'Sullivan. Standing alfvén waves in the magnetosphere. *Journal of Geophysical Research*, 74(3):778–793, 1969.

[97] C. L. Waters and M. D. Sciffer. Field line resonant frequencies and ionospheric conductance: Results from a 2-d mhd model. *Journal of Geophysical Research*, 113, 2008.

[98] K.S. Yee. Numerical solution of initial boundary value problems involving maxwell's equations in isotropic media. *IEEE Transactions on Antennas and Propagation*, AP-14(3), 1966.

[99] A. Yoshikawa and M. Itonaga. Reflection of shear alfven waves at the ionosphere and the divergent hall current. *Geophysical Research Letters*, 23(1):101–104, 1996.

[100] Z. Y Zhao and B. B. Ni. Signatures of the ionospheric alfvén resonator from aureol-3 ulf/elf fluctuation measurements. *Journal of Atmospheric and Solar-Terrestrial Physics*, 68, 2006.

Appendix A

Differential Geometry

A.1 Covariance and Contravariance

A position in 3-dimensional space is naturally located using 3 coordinates, (x^1, x^2, x^3). Coordinate surfaces are defined by holding one variable constant and allowing the other two to vary. For example, the spherical coordinate system (r, θ, ϕ) has coordinate surfaces which are a sphere, cone, and cylindrical shell. The orthogonal dipole coordinate system has a surfaces which are formed by rotating a dipole field line around the polar axis and by tracing magnetostatic potential contours. The i^{th} contravariant basis vector is orthogonal to the x^i coordinate surface, while the i^{th} covariant vectors are orthogonal to the x^j and x^k basis vectors. The covariant and contravariant basis vectors are parallel when the coordinates are orthogonal, but this is not the case otherwise.

A.1.1 General Definitions

Given a triplet of coordinates (x^1, x^2, x^3), contravariant basis vectors are defined by

$$\varepsilon^i = \nabla x^i \tag{A.1}$$

Covariant basis vectors are defined with respect to the contravariant basis,

$$\varepsilon_i = \frac{\varepsilon^j \times \varepsilon^k}{\varepsilon^i \cdot \varepsilon^j \times \varepsilon^k} \tag{A.2}$$

Note that this definition is such that covariant basis vectors ε_i are orthogonal to the contravariant basis vectors,

$$\varepsilon_i \cdot \varepsilon^j = \delta_i^j \tag{A.3}$$

It is also possible to start with the covariant basis and obtain the contravariant basis,

$$\varepsilon^i = \frac{\varepsilon_j \times \varepsilon_k}{\varepsilon_i \cdot \varepsilon_j \times \varepsilon_k} \tag{A.4}$$

The quantity $\varepsilon_{\mathbf{1}} \cdot (\varepsilon_2 \times \varepsilon_{\mathbf{3}})$ is conventionally referred to as the Jacobian determinant, denoted J. The Jacobian determinant may also be related to the contravariant basis vectors, as it can be straightforwardly shown that

$$J = \varepsilon_{\mathbf{1}} \cdot (\varepsilon_2 \times \varepsilon_{\mathbf{3}}) = \frac{1}{\varepsilon^1 \cdot (\varepsilon^2 \times \varepsilon^3)} \tag{A.5}$$

The covariant and contravariant bases can be related by means of the metric tensors, $\mathbb{G}^{ij}$ and $\mathbb{G}_{ij}$. The components of these metrics are defined as

$$\eth^{ij} = \varepsilon^i \cdot \varepsilon^j \qquad \eth_{ij} = \varepsilon_i \cdot \varepsilon_j \tag{A.6}$$

Covariant and contravariant components of a vector $\mathbf{V}$ are then related by the formulas

$$V^i = \eth^{ij} V_j \qquad V_i = \eth_{ij} V^j \tag{A.7}$$

Note (A.7) actually indicates the operation of the metric tensors $\eth_{ij}$ and $\eth^{ij}$ upon the vector $\mathbf{V}$. The repetition of index implies summing over that index from 1 through 3, e.g. $V_1 = g_{11}V^1 + g_{12}V^2 + g_{13}V^3$, where g_{lm} is the l, m component of $\eth_{ij}$.

If a metric tensor has no off-diagonal terms, then the coordinate system is said to be orthogonal. The presence of any off-diagonal terms means that the system is non-orthogonal. The most common systems - Cartesian, Cylindrical, Spherical - are orthogonal. However, as we discussed earlier, the Earth's magnetic field does not conform to one of these basic systems. Even though it can be modeled using a so-called Dipole coordinate system, inclusion of the Ionosphere as a coordinate surface requires us to extend our consideration to nonorthogonal coordinates.

A.2 Generalized Vector Calculus

Let f be a scalar function and $\mathbf{V}$ be a vector function. The scale factors h^i and h_i are related to the basis vectors by

The components of the basis vectors are called scale factors,

$$h^i = \sqrt{g^{ii}} \qquad h_i = \sqrt{g_{ii}} \tag{A.8}$$

A.2.1 Basic Operations

The gradient is defined by

$$\nabla f = \frac{\partial f}{\partial x^i}\varepsilon^i \tag{A.9}$$

Where, again, repeated indices indicate summation over 1-3.

The divergence is defined by

$$\nabla \cdot \mathbf{V} = \frac{1}{J}\frac{\partial}{\partial x^i} JV^i \tag{A.10}$$

And the curl is defined by

$$\nabla \times \mathbf{V} = \frac{\delta^{ijk}}{J}\frac{\partial V_k}{\partial x^j}\varepsilon^i \tag{A.11}$$

Here δ^{ijk} is the familiar Levi-Citiva or permutation symbol.

Note that both the gradient and curl are contravariant vectors, that is, they are directed along the contravariant basis. If the covariant and contravariant bases do not coincide, then it is necessary to use metric tensors (A.6) to relate the expressions.

In addition to these differential operations, familiar integral operations can be generalized using the notions of covariance and contravariance.

A.2.2 Area, Length, and Volume

The differential path length is defined in terms of the covariant basis vectors as

$$d\ell = dx^i \varepsilon_i \tag{A.12}$$

The differential area is defined as

$$d\mathbf{a}^i = (\varepsilon_j \times \varepsilon_k) dx^j dx^k \tag{A.13}$$

The differential volume is given by

$$dV = \varepsilon_{\mathbf{1}} \cdot (\varepsilon_2 \times \varepsilon_{\mathbf{3}}) dx^1 dx^2 dx^3 \tag{A.14}$$

Comparing (A.13) and (A.2), it is seen that the area vector is parallel to the contravariant basis vector. Using (A.5), we can write the area formula as

$$d\mathbf{a}^i = \varepsilon^i J dx^j dx^k \tag{A.15}$$

A.2.3 Derivatives

The most straightforward way to calculate derivatives with respect to dipole coordinates is to make use of the directional derivative.

$$\frac{\partial}{\partial x^i} = \varepsilon_i \cdot \nabla \tag{A.16}$$

Application to Dipole Coordinates

From (A.16) it follows that derivatives with respect to the dipole coordinates can be expressed in spherical coordinates as

$$\frac{\partial}{\partial \nu} = \frac{r^2}{\sin\theta(1+3\cos^2\theta)}\left(\sin\theta\frac{\partial}{\partial r} - \frac{2\cos\theta}{r}\frac{\partial}{\partial\theta}\right) \tag{A.17}$$

$$\frac{\partial}{\partial \mu} = \frac{r^3}{1+3\cos^2\theta}\left(2\cos\theta\frac{\partial}{\partial r} + \frac{\sin\theta}{r}\frac{\partial}{\partial\theta}\right) \tag{A.18}$$

A.2.4 Curvature

The curvature is a vector directed towards the center of curvature whose magnitude is inversely proportional to the local radius of curvature. We include this for reference purposes, because it is helpful for understanding e.g. how well the magnetic field may be locally approximated as Cartesian. Specifically, if the local radius of curvature of the field line is much larger than the local wavelength, geometrical effects should not be

very important and the field may be considered locally straight. For instance, the quasi-dipolar models of Lysak[45],[49] consider inertial scale waves for which this assumption essentially correct.

Functionally, the curvature can be determined by taking the directional derivative of a vector along itself,

$$\kappa = \mathbf{v} \cdot \nabla \mathbf{v} \tag{A.19}$$

This expression is a little troublesome, though, because it requires us to evaluate the derivatives of the unit vectors as well as the magnitude of the vector. However, it is possible to avoid this problem by making use of the vector identity

$$\mathbf{v} \cdot \nabla \mathbf{v} = (\nabla \times \mathbf{v}) \times \mathbf{v} + \nabla \frac{\mathbf{v} \cdot \mathbf{v}}{2} \tag{A.20}$$

Moreover, if we are specifically interested in calculating the curvature of a unit vector, then $\hat{e}_v \cdot \hat{e}_v = 1$ and consequently $\nabla(\hat{e}_v \cdot \hat{e}_v) = 0$. In practice, this is a significant simplification, because we can make use of equation (A.11).

For example, it can be shown that the curvature of the $\hat{e}_\mu$ basis vector associated with the orthogonal dipole coordinate system is given by

$$\kappa_\mu = -\frac{1}{h_\nu} \frac{\partial}{\partial \nu} \log h_\mu \tag{A.21}$$

While the curvature of the $\hat{e}_\nu$ basis vector is given by

$$\kappa_\nu = -\frac{1}{h_\mu}\frac{\partial}{\partial \mu}\log h_\nu \hat{e}_\mu \tag{A.22}$$

And the curvature of the $\hat{e}_\phi$ is given by

$$\kappa_\phi = -\left(\frac{1}{h_\nu}\frac{\partial}{\partial \nu}\log h_\phi \hat{e}_\nu + \frac{1}{h_\mu}\frac{\partial}{\partial \mu}\log h_\phi \hat{e}_\mu\right) \tag{A.23}$$

A much simpler expression is obtained if analyzed in cylinder coordinates, where it is found that

$$\kappa_\phi = -\frac{\hat{e}_s}{s} \tag{A.24}$$

Where $s = r\sin\theta$ is identical to the covariant scale factor h_ϕ and $\hat{e}_s$ is the cylinder radius vector - precisely what one would expect based on purely geometrical considerations. Equations (A.23) and (A.24) are equivalent, but the dipole expression is obviously more complicated. This is the price for dealing with dipole coordinates - they reduce the complexity of Maxwell's equations, but are generally intractable for analytical operations.

Finally, note that a scalar curvature coefficient can be defined as the quadrature sum of the individual curvatures, $\kappa = \sqrt{\kappa_\nu^2 + \kappa_\phi^2 + \kappa_\mu^2}$. For a wave with local wavelength λ, $\kappa\lambda \ll 1$ is the validity criterion for considering the fields to be locally straight.

Appendix B

The Atmospheric Solution

The magnetic field in the Earth's atmosphere is both divergenceless, and curl-free, allowing us to represent it in terms of a scalar potential,

$$\mathbf{B}_A = \nabla\Psi \tag{B.1}$$

And then to determine that scalar potential from Laplace's equation,

$$\left(\frac{1}{r^2}\frac{\partial}{\partial r}r^2\frac{\partial}{\partial r} + \frac{1}{r^2\sin^2\theta}\frac{\partial^2}{\partial\phi^2} + \frac{1}{r^2\sin\theta}\frac{\partial}{\partial\theta}\sin\theta\frac{\partial}{\partial\theta}\right)\Psi = 0 \tag{B.2}$$

Note that we have used the spherical representation of the Laplacian operator here because the geometry of the Earth-Atmosphere cavity is that of a thin spherical shell.

The solution to (B.2) can be obtained using Separation of Variables[8], yielding $\Psi(r,\theta,\phi) = R(r)\Phi(\phi)\Theta(\theta)$, where the radial and azimuthal solutions are given by

$$R(r) = A_\ell^m r^{\nu_\ell^m} + \frac{B_\ell^m}{r^{\nu_\ell^m+1}} \qquad \Phi(\phi) = e^{im\phi} \tag{B.3}$$

Here $m = -\infty...\infty$ is the azimuthal mode number, $\ell = |m|...\infty$ is the eigenvalue index, and ν_ℓ^m is related to the separation constant, which can be determined by solving the remaining polar equation,

$$\frac{1}{\sin\theta}\frac{\partial}{\partial\theta}\sin^2\theta\frac{\partial\Theta}{\partial\theta} + \left(\lambda_\ell^m - \frac{m^2}{\sin^2\theta}\right)\Theta = 0 \tag{B.4}$$

Where $\lambda_\ell^m = \nu_\ell^m(\nu_\ell^m + 1)$.

The general solution to (B.2) is a sum over all ℓ and m.

B.1 Solution of the Polar Equation

B.1.1 Associated Legendre Eigenfunctions

Using the substitution $x = \cos\theta, P(x) = \Theta(\theta)$ in (B.4), we have

$$\frac{d}{dx}\left((1-x^2)\frac{dP}{dx}\right) + \left(\lambda - \frac{m^2}{1-x^2}\right)P = 0 \tag{B.5}$$

When $-1 \le x \le 1$, the solutions to (B.5) are the Associated Legendre Functions, $P_\lambda^m(x)$, with $\lambda = \ell(\ell+1)$,$\nu = \ell$ $m = \infty...\infty$ and $\ell = |m|...\infty$. However, when either $\theta = 0$ or $\theta = \pi$ (or both) is excluded, λ is no longer an integer and these past few relations do not directly hold. Instead, (B.5) must be treated numerically as a Sturm-Liouville

eigenvalue problem. Much of the following discussion is based on Chapter 9 of [8].

B.1.2 Sturm-Liouville Theory

The most general form of a Sturm-Liouville eigenvalue problem is

$$\frac{d}{dx}\left(p(x)\frac{dy}{dx}\right) + (q(x) + w(x)\lambda)\,p(x) = 0 \tag{B.6}$$

Along with homogeneous boundary conditions

$$A_1 y(x_1) + B_1 \frac{dy}{dx}(x_1) = 0 \qquad A_2 y(x_2) + B_2 \frac{dy}{dx}(x_2) = 0 \tag{B.7}$$

With the requirement that $A_{1,2}, B_{1,2}$ are real numbers and $w(x) \geq 0$ for $x_1 \leq x \leq x_2$.

Equations of the form (B.6) are guaranteed to have an infinite number of eigenvalues λ with $\lambda_n < \lambda_{n+1}$. Moreover, these solutions are guaranteed to be orthogonal with respect to the weight function $w(x)$ (which happens to be 1 for Legendre's equation). Two functions y_1 and y_2 are orthogonal on (x_1, x_2) if their inner product vanishes,

$$\int_{x_1}^{x_2} y_1^*(x) y_2(x) w(x) dx = 0 \tag{B.8}$$

We can show that any two eigenfunctions of the Sturm-Liouville equation are orthogonal under the given conditions by considering the equations for y_1^* and y_2.[1] We multiply the equation for y_1^* by y_2 and vice versa, take the difference of the results, and use

[1] If we have a complex eigenfunction y with complex eigenvalue λ, then y^* is the solution for eigenvalue λ^*.

integration by parts to obtain

$$y_1^* \frac{dy_2}{dx} - y_2 \frac{d\psi_1^*}{dx}\bigg|_{x_1}^{x_2} = \int_{x_1}^{x^2} y_1^*(x) y_2(x) w(x) dx \tag{B.9}$$

If either ψ or its derivative vanishes at both x_1 and x_2, then Equation (B.9) shows that the eigenfunctions are orthogonal. This is the case for our application of Legendre's equation (B.5). Thus, the Legendre eigenfunctions are orthogonal.

In addition to orthogonality, solutions of the Sturm-Liouville equation are complete - that is, any function $f(x)$ that satisfies the same boundary conditions as the eigenfunctions $y(x)$ may be represented on (x_1, x_2) by a linear superposition of eigenfunctions,

$$f(x) = \sum_n C_n y_n(x) \tag{B.10}$$

Where $y_n(x)$ is the eigenfunction corresponding to the eigenvalue λ_n. The coefficients C_n can be obtained by making use of the orthogonality relationship (B.9), giving us

$$C_n = \frac{\int_{x_1}^{x_2} y_n^*(x) f(x) w(x) dx}{\int_{x_1}^{x_2} |y_n(x)|^2 w(x) dx} \tag{B.11}$$

B.2 Fitting on a Discrete Grid

Unlike the usual case of Associated Legendre functions, the solutions of Legendre's equation over a limited range of polar angles is not expressible in terms of standard functions. This makes the evaluation of (B.11) for the fitting coefficients C_n rather

costly. Perhaps more prohibitive, however, is the discrete sampling of $f(x)$ that arises in practical applications. While it is, in principle, possible to interpolate the data points and perform the indicated integration, we prefer to determine the fitting coefficients by converting the eigenfunction representation to a matrix equation and inverting the resultant coefficient matrix.

B.2.1 Calculation of Eigenvalues and Eigenfunctions

The eigenvalue of Legendre's equation must be real, as required by Sturm-Liouville theory, but need not be integral as is the case when $0 \leq \theta \leq \pi$. Instead, we must consider the eigenvalues to be an unknown (albeit well-behaved) function of the boundary points. This is the starting point for developing an effective numerical routine for their calculation.

Shooting Method

Numerical solution of first order differential equations is typically easier than the solution of second order equations. This is true even for systems of equations, as standard methods are predominantly first order[73]. With this in mind, we can express Legendre's equation can be written as a first-order system of differential equations,

$$\frac{d}{dx}\begin{pmatrix} P \\ Q \end{pmatrix} = \begin{pmatrix} 0 & \dfrac{Q}{1-x^2} \\ \dfrac{m^2}{1-x^2} - \lambda & 0 \end{pmatrix} \cdot \begin{pmatrix} P \\ Q \end{pmatrix} \tag{B.12}$$

Where $Q = (1-x^2)\dfrac{dP}{dx}$.

Systems like (B.12) can be readily integrated using Runge-Kutta methods[73]. However, in order to do so, we must consider the boundary conditions in order to determine appropriate initial conditions.

The boundary conditions are uniform and homogeneous, either $P(x_1) = P(x_2) = 0$ or $Q(x_1) = Q(x_2) = 0$. This means that one of P and Q remain unspecified at each boundary. This is not a problem, however, because (B.12) is a linear set of equations, and any multiple of a solution is likewise a solution. We can simply set the unspecified quantity to a reasonable value - say, 1 - at x_1. If the eigenvalue λ is known, then the system can then be integrated to x_2, where it should satisfy the specified boundary conditions.

Locating and Calculating Eigenvalues

Let us consider the wave equation for a uniform string in one dimension. Solutions to this equation provide an indication for how we can locate eigenvalues of Legendre's equation.

$$\frac{\partial^2 y(x)}{\partial x^2} = -\lambda^2 y(x) \tag{B.13}$$

The eigenvalue of this equation is related to the length of the string, L, by relation $\lambda = 2\pi n/L$, where $n = 1, 2, 3...$ is the harmonic number. It is apparent from this that the magnitude of the eigenvalue is inversely related to the length of the interval on which the eigenfunction is defined.[2]

[2] Asymptotic methods can be used to show that the spacing between adjacent eigenvalues converges on $\pi/(\sin^{-1}(x_1) - \sin^{-1}(x_0))$.

Our method for locating roots is a simple marching method, which starts with a guess for the eigenvalue λ_g. We integrate (B.12) from x_1 to x_2 to obtain $P(\lambda_g; x_2)$. If λ_g is an actual eigenvalue of the equation, then we will find $P(\lambda_g; x_2) = 0$, but it will most likely not be. Instead, we make a second guess at λ, increasing our guess for λ by some fixed increment $\delta\lambda$, finding $P(\lambda_g + \delta\lambda; x_2)$. If $P(\lambda_g; x_2)P(\lambda_g + \delta\lambda; x_2) > 0$, then we add another $\delta\lambda$ and $P(\lambda_g + 2\delta\lambda; x_2)$. We continue this iteration until $P(\lambda_g; x_2)P(\lambda_i; x_2) < 0$, where $\lambda_i = \lambda_g + i\delta\lambda$ is the i^{th} guess. The intermediate value theorem guarantees that $P(\lambda; x_2 = 0$ for some value of $\lambda_g < \lambda < \lambda_i$, and if $i \neq 1$, it is actually better, guaranteeing that that $\lambda_{i-1} < \lambda < \lambda_i$.

Once the root of $P(\lambda; x_2)$ has been bracketed, it can be evaluated using numerical root-finding techniques such as Brent's method. (See Chapter 9 of [73] for more details.)

Calculating Numerical Eigenfunctions

Once a given eigenvalue has been determined, the eigenfunction may be determined using step-by-step integration. Starting at the initial point x_i, Legendre's equation is integrated to the next point where the value is needed, x_{i+1}. The value of the function at x_{i+1} is then used as the initial condition for the integration from x_{i+1} to x_{i+2}, and so on, until we have obtained values for all x_n on the entire interval $x_1 \leq x \leq x_2$.

B.2.2 Determining Eigenfunction Coefficients

Let M be the maximum azimuthal order of the truncated eigenfunction fit. For each value of m, we determine $M - |m| + 1$ eigenfunctions[3] This means that we must determine

[3]This is consistent with standard approach for spherical harmonics, were the sum is taken over index $\ell = 0...\infty$ and $m = -\ell...\ell$.

the $M(M+1)$ coefficients of our eigenfunctions. If the function being fit is defined on an $n_1 \times n_2$ grid, where n_1 is the number of sampling points along the latitudinal direction and n_2 is the number of points along the longitudinal direction, then we can represent the fitting with a matrix equation,

$$\begin{pmatrix} \ddots & & \\ & \mathbb{C}^{i,j}_{\ell,m} & \\ & & \ddots \end{pmatrix} \cdot \begin{pmatrix} \vdots \\ A^{\ell,m} \\ \vdots \end{pmatrix} = \begin{pmatrix} \vdots \\ F^{i,j} \\ \vdots \end{pmatrix} \tag{B.14}$$

Here ℓ is the index of the eigenvalue, not the eigenvalue itself. Components of the matrix $\mathbb{C}^{i,j}_{\ell,m}$ are given by

$$c^{i,j}_{\ell,m} = \nu R_I^{\lambda^m_\ell} \left(1 - \left(\frac{R_E}{R_I}\right)^{2\lambda^m_\ell + 1}\right) P^m_\lambda(x_i) e^{im\phi_j} \tag{B.15}$$

Typically, $m(m+1) \neq n_1 n_2$. Since $\mathbb{C}^{i,j}_{\ell,m}$ is non-rectangular, we cannot determine the coefficients $A^{\ell,m}$ from (B.14) by multiplying it by the inverse of the coefficient matrix $\mathbb{C}^{-1}$. This is because, for a non-rectangular matrix, the system is either under- or over-determined.[4] We can, however, find a so-called pseudoinverse[66]. The pseudoinverse does not exactly solve the system of equations (i.e. the pseudoinverse times the matrix is not necessarily a unit matrix), but it does provide a best fit in the least-squares sense.[5]

[4] That's to say, there are either infinitely many or not necessarily any solutions.

[5] For a discussion of the numerical technique used to determine the pseudoinverse of a matrix, see Chapter 2 of [73].

B.2.3 Choosing the Order of the Legendre Expansion

A theorem due to Kramer[39] extends Shannon's sampling theorem[8] to the case of discrete eigenfunction expansions, provided that the average sampling frequency exceeds the Nyquist sampling rate. The meaning of these ideas is obvious in the case of a Fourier expansion, but not so obvious for Legendre functions. However, one can readily show that the average distance between roots of a the n^{th} Legendre function is equal to $(x_1 - x_0)/n$. Because we are beginning with a discretely sampled signal, rather than sampling a continuous signal, we are forced to believe that the most rapid possible variation is a frequency of $1/2N\Delta x$[1]; any more rapid variations would not be physically represented by the underlying discrete model and would be effectively undetectable. In any event, the representation of an N point sampling requires at most N discrete modes.

The Legendre function expansion involves a double summation over N meridional modes and $2N+1$ azimuthal modes. According to Kramer's theory, we can fully represent the meridional function sampled at N points with N eigenmodes. For any given meridional value, $2N + 1$ azimuthal modes allows for the fitting of $2N + 1$ points. Optimally, therefore, if there are M azimuthal grid points, we would choose the maximum order of the Legendre function expansion to be $\ell_{\rm MAX} = (M - 1)/2$. Unless $N = \ell_{\rm MAX}$ we will be under-representing the meridional function. However, this under-representation may not be a problem since the atmospheric shielding effect should screen out signals with perpendicular scale sizes on the order of the ionospheric width, which we take to be about 40 km. For the bounded region $2 \leq L \leq 20$ with $M = 89$, the meridional Nyquist scale size is 40 km,[6] and we expect any smaller scale signals to be damped.

Thus, for construction of signals at the ground, we can reasonably choose the order of

[6]For comparison, the azimuthal scale length is 320 km at $L = 2$ and 100 km at $L = 20$.

the expansion based on the optimal representation of azimuthal modes. The number of azimuthal grid points should itself be chosen so that the meridional Nyquist scale length is approximately equal to the width of the atmosphere, permitting us to ignore smaller scale perturbations.

Appendix C

The WKB Method

C.1 Description

Generally speaking, the WKB Method is a mathematical prescription for obtaining an asymptotic series representation to the solution of a differential equation. Although it is actually quite a general method[12], it is especially well-known for its solutions to second-order differential equations, such as the Schrödinger and Wave equations.

C.1.1 Mathematical Basis

Suppose we have the second order differential equation

$$\frac{\partial^2 f}{\partial x^2} + 2P(x)\frac{\partial f}{\partial x} + Q(x)f = 0 \tag{C.1}$$

If $P(x)$ and $Q(x)$ are constant, then the solution to the equation is given by $f =$

$Ae^{ik_{\pm}x} + Be^{ik_{\mp}x}$ where $k_{\pm} = -p \pm \sqrt{p^2 - Q}$. This is the familiar harmonic oscillator solution.

The WKB method proceeds by assuming that so long as $P(x)$ and $Q(x)$ are slowly varying relative to $f(x)$, the solution remains similar to the oscillator, allowing for a slight variation in the effective wave vector. We introduce the WKB series,

$$f(x) \sim exp\left(\frac{1}{\delta}\sum_{n=0}^{\infty} S_n \delta^n\right) \tag{C.2}$$

Where where δ is assumed to be a small parameter and $\sim$ indicates that the two expressions are asymptotically equivalent - that is, if we truncate the series after N terms, the error goes as $\delta^N, \delta \to 0$.

Although it is possible to extend the WKB series to an arbitrary number of terms, we will consider only the two most common approximations - those which truncate after only one or two terms.

C.2 WKB Approximations to the Wave Equation

C.2.1 Cartesian Coordinates

In Chapter 4, we studied a pair of equations for the cavity and waveguide modes of the IAR. The general equation for these modes was

$$\frac{d^2E}{dz^2} + \left(\frac{\omega^2}{V_A^2(z)} - k_{\perp}^2\right)E = 0 \tag{C.3}$$

Inserting the WKB ansatz from (C.2) into the IAR mode equation, we find

$$\left(\frac{1}{\delta}\sum_{n=0}^{\infty}\delta^n S_n'(z)\right)^2 + \frac{1}{\delta}\sum_{n=0}^{\infty}\delta^n S_n''(z) + k_z^2(z) = 0 \tag{C.4}$$

Where $k_z^2 = \omega^2/V_A^2(z) - k_\perp^2$ and $'$ indicates differentiation with respect to z. Truncating the WKB series at $n = 1$ and retaining terms up to order δ^{-1}, we find

$$\frac{(S_0')^2}{\delta^2} + \frac{2S_0'S_1'}{\delta} + \frac{S_0''}{\delta} + k_z^2(z) = 0 \tag{C.5}$$

Since δ is a small parameter, we find that $(S_0')^2 \approx k_z^2$. Solving this equation for S_0 gives us the geometrical optics or eikonal approximation,

$$S_0(z) = i\int_{z_0}^{z} k_z(z')dz' \tag{C.6}$$

This eikonal approximation describes the phase variation of the solution as we proceed from point z_0 to z, but it provides no information regarding variation in amplitude. We can, however, use the eikonal solution to determine the next order correction by solving the same equation with our known S_0 at order δ^{-1}. Doing so, we find

$$S_1(z) = -\frac{1}{4}\log\left(k_z^2\right) \tag{C.7}$$

This is the so-called physical optics approximation, and the resultant WKB series describes both phase and amplitude variations,

$$f(z) \sim \sqrt{\frac{k_z(z_0)}{k_z(z)}} \left(A e^{i \int_{z_0}^{z} k_z(z')dz'} + B e^{-i \int_{z_0}^{z} k_z(z')dz'} \right) \tag{C.8}$$

For the IAR cavity modes, $k_z = \omega / V_A(z)$, so we have

$$E_x(z) \sim \sqrt{\frac{V_A(z)}{V_A(z_0)}} \left(A e^{i\omega\tau} + B e^{-i\omega\tau} \right) \tag{C.9}$$

Where $\tau = \int_{z_0}^{z} \frac{dz'}{V_A(z')}$ is the Alfvén speed travel time. Note that in this approximation, the background magnetic field is constant and the Alfvén speed variation depends only on the density. We therefore find $E_x \propto^{-4} \sqrt{\rho}$. Thus we would expect the electric field decreases in regions larger density and increases in regions of lower density.

For the IAR waveguide mode, $k_z = \sqrt{\omega^2 / V_A(z)^2 - k_x^2}$. Unlike the cavity mode, the waveguide mode has a potential cutoff, where $k_x = \omega / V_A(z)$. Indeed, it is because of this cutoff that the waveguide mode can exist - if the Alfvén speed is such that $\omega > k_x V_A(z)$ for all z, then the waveguide mode does not exist, being rather a variation on the cavity mode. This was discussed in context of a particular density model in Chapter 4. Note that the amplitude of the waveguide mode is predicted to be zero at the cutoff, which is consistent with our expectations.

C.2.2 Dipole Coordinates

A somewhat more complicated situation is found if we consider oscillations in a dipole magnetic field. We can represent the cavity and waveguide modes using the general equation

$$\frac{1}{g_{ii}}\frac{\partial}{\partial\mu}\frac{1}{g_{jj}}\frac{\partial\mathcal{E}_j}{\partial\mu} - \frac{1}{g_{ii}}\left(\frac{\partial^2}{\partial x_i^2} + g_{ii}\frac{\omega^2}{V_A^2}\right)\mathcal{E}_j = 0 \tag{C.10}$$

We can safely assume that the geometrical factors g_{ii} and g_{jj} vary much more slowly than the (covariant) electric field. Ignoring derivatives of these factors, we can write the previous equation in a more familiar form,

$$\frac{\partial^2\mathcal{E}_j}{\partial\mu^2} - g_{\mu\mu}\left(\frac{1}{g_{ii}}\frac{\partial^2}{\partial x_i^2} + \frac{\omega^2}{V_A^2}\right)\mathcal{E}_j = 0 \tag{C.11}$$

Instead of k_z we find k_μ, but the process is otherwise similar, yielding

$$k_\mu = \sqrt{\frac{\omega^2}{V_A^2} + \frac{1}{g_{ii}}\frac{\partial^2}{\partial x_i^2}} \tag{C.12}$$

In this context, it doesn't make much sense to consider the square root of a differential operator, but if we assume wave-like behavior in the transverse directions, we have

$$k_\mu = h_\mu\sqrt{\frac{\omega^2}{V_A^2} - k_\perp^2} \tag{C.13}$$

Where $k_\perp$ is some suitably determined transverse wave number. Making this assumption allows us to use the same equations as in the Cartesian case. For instance, the IAR cavity mode has

$$\mathcal{E}_\nu = \sqrt{\frac{h_\mu(\mu_I)V_A(\mu)}{h_\mu(\mu)V_A(\mu_I)}}\left(Ae^{i\omega\tau} + Be^{-i\omega\tau}\right) \tag{C.14}$$

Here the travel time is given by $\tau = \int_{\mu_I}^{\mu} \frac{h_\mu d\mu'}{V_A(\mu')}$, where $h_\mu = \sqrt{g_{\mu\mu}}$ is the covariant scale factor along the magnetic field and $h_\mu d\mu$ is a differential unit of length along the field.

Note that $h_\mu = B_{EQ}/B_0$, so given that $V_A \propto B_0$ the product $h_\mu V_A$ is independent of magnetic field. As a consequence the amplitude factor in dipole coordinates ends up being identical to that of Cartesian coordinates, giving us

$$\mathcal{E}_\nu = \left(\frac{\rho(\mu_I)}{\rho(\mu)}\right)^{1/4} \left(Ae^{i\omega\tau} + Be^{-i\omega\tau}\right) \tag{C.15}$$

C.3 Validity of the WKB Approximation

As discussed earlier, the WKB series is asymptotic to the actual function which it approximates. Unlike Taylor series, WKB series do not necessarily converge on the function which they approximate. Instead, it is often the case that the optimal WKB approximation uses just a few terms (a property characteristic of asymptotic series in general). The physical optics approximation is, fundamentally, much more accurate than the equivalent Taylor series. Indeed, for potentially dispersive phenomena in slowly-varying media, WKB solutions are typically excellent approximations to the true solution.

If L is the scale length of variations of any background parameter (e.g. magnetic field, density, scale factors), the physical optics approximation is valid so long as the following conditions apply:

$$S_0' \gg \frac{S_0}{L} \qquad |S_0| \gg |S_1| \qquad (S_0')^2 \gg S_0'' \tag{C.16}$$

Notice that the existence of a turning point invalidates the second validity requirement, since it results in $S_1 \to \infty$ while S_0 remains finite. It is possible to extend the WKB framework to include this case (via linearization around the turning point and the use of Airy's equation), but that is beyond the scope of this discussion.

Appendix D

Models of Physical Parameters

D.1 Alfvén Speed and Density Profiles

D.1.1 Greifinger's Model

$$V_A^2 = \frac{V_{A,0}^2}{\epsilon^2 + e^{-z/H}} \tag{D.1}$$

As noted earlier, the hydromagnetic wave equation with this Alfvén speed profile admits of an analytic solution in terms of Bessel functions of complex order and argument.

Applicability

Because of its aforementioned analytical properties, this is a convenient and useful profile for studies of hydromagnetic wave structure in the near-Earth magnetosphere. However, given the asymptotic constancy of the Alfvén speed profile makes it unsuitable

for distances beyond $\approx 1R_I$, since it is known that the Alfvén speed beyond this point decreases as a power-law.

D.1.2 Two-Species Density Model

Lysak[48] modeled the magnetospheric density using a combination of an exponential to represent the near-Earth heavy ion population and the a power-law to represent the magnetospheric population. In context of the parameters used in this thesis, Lysak's model is

$$\rho = n_H(L)\left(\frac{r}{R_I}\right)^{-\alpha} + 16n_o e^{-\frac{r-R_I}{H}} \tag{D.2}$$

Where the $L-$dependence of the the hydrogen density n_H is given by

$$\frac{n_H^{hi}+n_H^{lo}}{2} + \frac{n_H^{hi}-n_H^{lo}}{2}\tanh\left(\frac{L-L_{PP}}{\Delta_{PP}}\right) \tag{D.3}$$

With n_H^{hi} being the base density in auroral zone, n_H^{lo} the base density in the plasmasphere, and a transition between the plasmasphere being represented through a hyperbolic tangent profile where L_{PP} is the $L-$shell of the plasmapause, Δ_{PP} the equatorial width of the plasmapause in R_I.

Chapman Variation

One of the more striking properties of the near-Earth plasma is the F_2 density peak. The density rises rapidly (somewhat faster than exponentially) from the ionospheric

base, reaching a maximum at $\approx$ 400 km. The density then decreases exponentially, smoothly joining into the magnetospheric density profile at $\approx$ 1000 km. This rapid rise and exponential decay can be well-modelled using Chapman's function,[46]

$$n_o = n_F \left(\frac{r}{R_I} \right)^{-\alpha} + 16 n_F e^{1-z-e^{-z}} \tag{D.4}$$

Where $z = (r - R_F)/H$ and n_F is the density of oxygen ions at the F_2 peak, $r = R_F$.

There is some evidence that the presence of a well-defined F_2 peak can result in the structuring of hydromagnetic waves in the Alfvén resonator region.

D.2 Ionospheric Conductance

D.2.1 Uniform Conductance

Although the ionospheric conductance is known to vary by orders of magnitude as a function of local time, it is often convenient to consider the ionosphere as being either locally or entirely uniform. For example, explicit expressions for the reflection of hydromagnetic waves are usually possible only when the conductance is uniform. This approximation is justified locally when the spatial gradients of the conductance are small and the transverse scale length of the hydromagnetic wave is much smaller than the conductance scale length.

Earlier, we applied a uniform ionosphere model to obtain reflection and transformation coefficients for hydromagnetic waves incident on the ionosphere and to find eigenmodes

of the Alfvén resonator. However, for numerical studies, we typically include the effects of dipole tilt, and often make use of more complicated models which account for latitudinal and local time variation.

When making use of a constant conductance model, we must be concerned with the ratio of conductances, Σ_P/Σ_H as well as the ratio of the conductances to the Alfvén conductance, say Σ_P/Σ_A. The first ratio indicates whether Pedersen or Hall effects will be more important, while the second indicates the importance of the ionospheric effects in general. Based on observations, the conductance ratio is fairly well constrained to $0.5 \leq \Sigma_P/\Sigma_H \leq 2$, but the ratio Σ_P/Σ_A can range greatly, with $0.01 \leq \Sigma_P/\Sigma_A \leq 100$ depending on the assumed conditions.

D.2.2 Empirical Conductance Model

The solar azimuth angle, χ, is defined by

$$\cos\chi = \sin\lambda\sin\delta - \cos\lambda\cos\delta\cos\phi_{LT} \tag{D.5}$$

Where λ is the (geographic) latitude, $\phi_{LT} = 15°LT$ is the local time angle, and $\delta = -23.45°\cos(90°QRT)$ with QRT being the number of quarter-years that have passed since the December solstice.

Given the solar zenith angle, the ionospheric conductance due to solar illumination can be determined from the empirical model fittings

$$\Sigma_P = 1.81 + 8.88\cos\chi \qquad \Sigma_H = 21.58 - 0.21\chi \tag{D.6}$$

This model was developed using three years of EISCAT radar measurements and is due to Senior[84]. Hurtaud[35] recently used this model as a basis of a time-dependent study of seasonal effects on ionospheric currents and plasma convection, who noted that its results generally agreed with observations, although it lacked the ability to account for solar activity. This shortcoming is easily overlooked, however, since we are not concerned with solar climatology in the present research.

D.2.3 Inclusion of Dipole Tilt Effects

It has been previously noted that the geomagnetic field does not intersect the ionosphere at a right angle. Instead, the incidence angle is given by

$$\cos\alpha = \frac{2\cos\theta}{\sqrt{1+3\cos^2\theta}} \tag{D.7}$$

A particularly interesting aspect of field lines with dipole tilt is that Alfvén wave magnetic fields are not only partially screened, allowing them to directly produce signatures on the ground. For ionospheres with uniform Pedersen conductance, it can be shown[24] that the ground magnetic field generated by ionospheric Pedersen currents exactly cancels the magnetic field associated with the wave currents. All ground field signatures in this case are due to the ionospheric Hall currents. This can be seen directly from the ionospheric jump conditions with the compressional magnetic field set to zero, since the resultant Laplace equation will is satisfied by a vanishing magnetic potential.[1]

For a field line with tilt angle α, the modified conductance tensor is[82]

[1]This is not the only admissible solution, though. Much like waves in the IAR, there will exist certain discrete frequencies for which the ground and ionosphere are nodes. The frequency of these eigenmodes is at the upper end of the ULF wave spectrum ($\approx$ 10 Hz), and they are referred to as Schumann resonances. The are not of interest in the frequency range we are considering.

$$\Sigma = \begin{pmatrix} \dfrac{\Sigma_0 \Sigma_P}{\Sigma_{zz}} & -\dfrac{\Sigma_0 \Sigma_H \cos\alpha}{\Sigma_{zz}} \\ \dfrac{\Sigma_0 \Sigma_H \cos\alpha}{\Sigma_{zz}} & \Sigma_P + \dfrac{\Sigma_H \sin^2\alpha}{\Sigma_{zz}} \end{pmatrix} \tag{D.8}$$

Here $\Sigma_{zz} = \Sigma_0 \cos^2\alpha + \Sigma_P \sin^2\alpha$ is the effective parallel conductance. Notice that at the equator the Hall terms vanish while the Pedersen terms become the parallel and Cowling conductances, respectively. At mid-latitudes, $\Sigma_{zz} \approx \Sigma_0 \cos^2\alpha \gg \Sigma_P \sin^2\alpha$ and we can use a simplified conductance tensor

$$\Sigma = \begin{pmatrix} \dfrac{\Sigma_P}{\cos^2\alpha} & -\dfrac{\Sigma_H}{\cos\alpha} \\ \dfrac{\Sigma_H}{\cos\alpha} & \Sigma_P \end{pmatrix} \tag{D.9}$$

This is the form of the tensor used in our model, used to locally apply the ionospheric boundary condition. The tensor varies as a function of colatitude along the magnetic meridians, causing the distortion of wave fronts with different scales in proportion to their latitudinal extent.[2]

[2] A wave with very small latitudinal scale will seen an essentially constant conductivity and thus be minimally distorted. A wave with large latitudinal scale will see much more non-uniformity and thus will be subject to greater distortion.